THREE-DIMENSIONAL SUPER-RESOLUTION IMAGING: FROM CELLULAR SURFACE TO INTERIOR

by

Reza Tafteh

B.Sc., Amirkabir University of Technology (Tehran Polytechnic), 2008

M.A.Sc., The University of British Columbia, 2011

A THESIS SUBMITTED IN PARTIAL FULFILLMENT OF

THE REQUIREMENTS FOR THE DEGREE OF

DOCTOR OF PHILOSOPHY

in

THE FACULTY OF GRADUATE AND POSTDOCTORAL STUDIES

(Chemistry)

THE UNIVERSITY OF BRITISH COLUMBIA

(Vancouver)

March 2017

Abstract

Single-molecule localization microscopy has greatly improved our understanding of biology by providing super-resolution images of biological processes and structures. However, it is still very challenging to apply this technique to thick tissues. A 3D imaging system based on single-molecule localization microscopy is presented to allow high-accuracy drift-free (< 0.7 nm lateral; 2.5 nm axial) imaging many microns deep into a cell.

When imaging deep within a cell, distortions of the point-spread function result in an inaccurate and very compressed Z distribution. For the system to accurately represent the position of each molecule, a series of depth-dependent calibrations are required. The system and its allied methodology were developed to image the type-2 Ryanodine receptor (RYR2) in the cardiac myocyte at a depth of several microns. It enabled us to resolve the structure of the individual (30 nm square) receptors giving a result similar to that obtained with electron tomography.

We also present an optical setup using an electrically tunable lens to actively stabilize a single-molecule localization microscope in three dimensions (RMS ~ 0.7 nm lateral; ~ 2.7 nm axial). The effectiveness of the ETL was demonstrated by imaging endosomal transferrin receptors near the apical surface of B-lymphocytes at a depth of 8 μm. This stabilization system enables a more accurate topological cluster analysis.

We have used these super-resolution imaging approaches to examine overlap between the RYR2 and the L-type Calcium channel (Cav1.2) on the cellular surface and within the rat ventricular myocyte. We accurately imaged receptors down to a depth of 6 μm below the surface, and for the first time, using light microscopy, we were able to image individual receptors. The distribution of RyR2 and $Ca_v1.2$ parallel each other and vary greatly between the surface, just below the surface, and deep in the interior.

We have also used two-color super-resolution microscopy to quantify receptor organization on the plasma membrane of follicular (FO) and marginal zone (MZ) B cells. We have found that B cell receptors (BCR) on the surface of MZ B cells were more dispersed and exhibited less clustering than those on FO B cells.

Preface

The author of this work identified and developed the research objectives and the associated approaches under the supervision of Dr. Keng C. Chou and Dr. Edwin D. W. Moore. The author designed the optical setups and performed the corresponding instrumentations (both hardware- and software-wise). The author carried out the imaging experiments, post-processed the data and constructed the super-resolution images. The author wrote the initial draft of this thesis and refined it based on the feedbacks from the aforementioned supervisors.

Preparation of cardiomyocytes for single-molecule localization microscopy experiments was carried out by Dr. David Scriven. The physiological hypotheses were developed by Drs. Edwin. Moore and David Scriven, who further analyzed the data from physiological point of view.

The preparation of B cells for single-molecule localization microscopy experiments was carried out by Dr. Libin Abraham. The corresponding biological hypotheses were developed by Drs. Michael Gold and Libin Abraham, who further analyzed the data from biological point of view.

The following is a list of publications based on this work.

<u>Research Articles</u>

- R. Tafteh, D. R. L. Scriven, E. D. W. Moore, and K. C. Chou, "**Single molecule localization deep within thick cells; a novel super-resolution microscope**," J. Biophoton **9**, 155-160 (2016).
- R. Tafteh, L. Abraham, D. Seo, H. Y. Lu, M. R. Gold, K. C. Chou, "**Real-time 3D stabilization of a super-resolution imaging system using an electrically tunable lens**," Optics Express **20**, 22959-22970 (2016).

Patent

- R. Tafteh, K. C. Chou, "**Multifocal Method and Apparatus for Stabilization of Optical Systems**," US Patent #62/151,569, Washington, DC, USA (Filed on April 23, 2015).

Conference Papers, Posters and Presentations

- R. Tafteh, D. R. L. Scriven, E. D. W. Moore, and K. C. Chou, "Super-resolution imaging of thick cells: methods for real-time 3D stabilization and accurate depth-localization," in (OSA, 2015), JT3A.38.
- L. Abraham, R. Tafteh, H. Y. Lu, J. Scurll, K. W. Sung, K. C. Chou, D. Coombs, and M. R. Gold, "Receptor organization and mobility as the basis for the priming of Marginal Zone B cells," in B Cells at the Intersection of Innate and Adaptive Immunity, (Stockholm, Sweden, 2016).
- D. R. L. Scriven, R. Tafteh, K. C. Chou, and E. D. W. Moore, "**Super-Resolution Analysis of the Distribution of RyR, Cav1.2 and NCX within the Mammalian Couplon**," Biophys. J. 108, 266a-267a (2015).
- D. R. Scriven, R. Tafteh, K. C. Chou, and E. D. Moore, "**Super-Resolution Localization and Distribution of Proteins within the Mammalian Couplon**," Biophys. J. 104, 105a (2013).

Table of Contents

List of Tables

List of Figures

Acknowledgements

I would like to thank my research supervisor, Dr. Keng Chou, for his mentorship and guidance. Keng's enthusiasm and intuition in scientific research have always inspired me. Thank you for being both supportive and critical and thank you for caring deeply about your students' developments, both personally and academically.

I would also like to thank Dr. Edwin Moore for his mentorship and guidance. I would also like to thank Drs. David Scriven, Libin Abraham, Micheal Gold and Daniel Coomb for the fruitful collaborations and discussions. I would like to thank Henry Lu, Tim Jou and Denny Soe for their help. I am very grateful to Dr. Saeid Kamal for his technical support.

Finally, I would like to thank my family for their love and sacrifice; no words can express my gratitude to you.

Dedication

TO MY DEAR PARENTS, FATEMEH & ALI.

Chapter 1: From Microscopy to Nanoscopy

Designing lenses with sophisticated geometry rendering the lowest possible aberration was considered for years to be a way to unlimitedly enhance the resolution of microscopy systems. It was in the late 19th century when Ernst Abbe [2] and Lord Rayleigh [3] introduced their formulated resolution limit criteria, known as the diffraction limit theory. In analysis based on wave optics and the diffraction of light, they showed that two objects are spatially resolvable if they are separated by $\Delta x \geq \lambda/2$ NA; where λ is the wavelength of illumination or excitation light and NA is the numerical aperture of the objective lens. Numerical aperture is defined as $\mathrm{NA} = n \sin\alpha$, in which n is the refractive index of the imaging medium, and α is the maximum half-angle of the cone of light captured by the objective lens. The resolution of an imaging system can be improved mainly by: capturing light rays at the maximum possible angle, imaging in mediums with higher refractive indices, and using lower wavelength illumination sources. In addition, high-resolution images can be achieved using various optical and computational methods developed in the past few decades, including confocal microscopy, deconvolution microscopy, saturation microscopy, 4-Pi microscopy, and multi-photon microscopy [4, 5].

There is, however, a hidden assumption in the derivation of Abbe's diffraction limit, which makes the theory only valid if there is no prior knowledge about the object being imaged. For instance, the diffraction limit theory can be overcome when it comes to the localization of isolated single molecules. Here, the prior knowledge that a single molecule is isolated allows one to estimate its molecular position with sub-diffraction precision and achieve an order of magnitude better spatial resolution compared to diffraction-limited fluorescence microscopy. This concept has been known for a long time [6] and has been widely applied in single particle tracking (SPT) experiments [7, 8]. However, the emergence of new photoswitchable fluorophores and labelling

methods has made it possible to accumulate an ample number of localizations from millions of fluorophores in order to construct super-resolution images.

Single-molecule localization microscopy (SMLM) methods, such as photo-activated localization microscopy (PALM) [9], stochastic optical reconstruction microscopy (STORM), [10] and universal point accumulation for imaging in nanoscale topography (uPAINT) [11], use this prior knowledge to resolve the structures of biological systems with nanometer-scale spatial resolutions. SMLM is based on consecutive photoswitching of fluorophores (or fluorescent proteins) between the fluorescent state and the dark state such that only a subset of fluorophores is randomly activated at a given time. This approach allows one to spatially and temporally separate the point-spread functions (PSFs) of activated fluorophores and to estimate their lateral and axial positions using appropriate localization algorithms, even in sub-diffraction regions where hundreds of fluorophores are densely packed.

Chapter 2: Three-Dimensional Super-Resolution Microscopy

Fluorescence microscopy is one of the most widely used techniques for three-dimensional imaging of biological processes at the cellular and sub-cellular level. The availability of efficient fluorescent probes and specific labeling methods are two principle factors that have facilitated the success of fluorescence microscopy among various other microscopy techniques [12]. The diffraction of light, however, poses a limitation on the resolution of fluorescence microscopy, which leaves many subcellular structures too small to be resolved. For visible light in far field microscopy, spatial resolution is about half the wavelength of light (i.e. 200-300 nm in the lateral direction and 500-700 nm in the axial direction) [13]. Therefore, conventional optical microscopy does not possess sufficient resolving power for cellular structures and multi-protein complexes with sizes on the order of a few tens of nanometers.

The relatively low spatial resolution of optical microscopes comes from the fact that the diffraction barrier of light prevents the exact convergence of rays from an object to a single point at the image plane. Therefore, a sharp point on the object plane translates into a finite-sized spot in the image plane. The three-dimensional intensity distribution of that finite-sized spot is called the point spread function (PSF), which determines the resolution of the microscope. In principle, if two objects are closer than the full width half-maximum (FWHM) of the PSF, their images will overlap substantially, making them difficult to resolve [14]. The FWHM of the PSF in the lateral direction can be approximated by Abbe's diffraction limit theory [15]. However, the commonly used objective lenses yield a nonsymmetrical distribution of PSF, which makes the axial width of PSF about two times larger than its lateral width. This leads to a significant decrease in the axial resolution of optical microscopes (Figure 2.1a).

2.1 The Optical Resolution Limit

Resolution of an imaging system is classically defined as the smallest distance between two nearby objects such that the imaging system can still distinguish them as distinct entities (Figure 2.1b). The resolution in optical microscopy is limited by the diffraction of light. The lower bound of resolution in optical microscopy can be estimated based on the diffraction from a point source (i.e. small aperture). The approach presented here is based on the work by Mondel and Diaspro [16].

The image of a point, $I(x, y)$, is the Fraunhofer diffraction pattern of the limiting aperture (exit pupil). Thus, starting from the Fraunhofer approximation, one can write the diffraction pattern at a point (x, y) as

$$I(x, y) = I_0 \left(\frac{|K(x/\lambda d, y/\lambda d)|}{\lambda d} \right)^2, \qquad \textbf{Eq. 2.1}$$

where I_0 is the amplitude and $K(x/\lambda d, y/\lambda d)$ is the Fourier transform of the aperture function $k(x, y)$ evaluated at spatial frequencies $v_x = x/\lambda d$ and $v_y = y/\lambda d$ (Figure 2.1c). Assuming a circular aperture, the aperture function and its corresponding Fourier transform are given by

$$k(x, y) = \begin{cases} 1 & r \leq D/2 \\ 0 & r > D/2 \end{cases}, \qquad r = \sqrt{x^2 + y^2},$$

$$K(v_x, v_y) = \int_{x=0}^{\infty} \int_{y=0}^{\infty} k(x, y) \exp\left(-i2\pi(xv_x + yv_y)\right) \mathrm{dxdy}, \qquad \textbf{Eq. 2.2}$$

where D is the aperture diameter. By transforming Eq. 2.2 into polar coordinates in both the spatial and the Fourier domains ($x = rcos\theta, y = rsin\theta, v_x = \rho cos\phi,\ v_y = \rho sin\phi;\ d\varepsilon = 2\pi\rho dr$), the Fourier transform can be expressed as

$$K(\rho,\phi) = \frac{1}{(2\pi\rho)^2}\int_{\varepsilon=0}^{\pi D\rho r}\int_{\theta=0}^{2\pi} k(x,y)\exp\left(-i2\pi(xv_x + yv_y\right)\mathrm{dxdy}$$
$$= \frac{D}{2\rho}J_1(\pi D\rho). \qquad \textbf{Eq. 2.3}$$

where J_n is the n-th order Bessel function. Considering a plane wave focused using a convex lens (focal length, f), the diffraction pattern under the Fraunhofer approximation is given by

$$I(x,y) = \left(\frac{\pi D^2 I_0}{(\lambda f)^2}\right)\left|\frac{J_1(\pi Dr/\lambda f)}{\pi Dr/\lambda f}\right|^2. \qquad \textbf{Eq. 2.4}$$

This diffraction pattern is called an Airy pattern, which consists of a bright central lobe surrounded by many circular rings Figure 2.1d; the intensity of the circular rings decreases with the distance from the central lobe. Two nearby airy patterns are distinguishable from each other if the central lobe of the first pattern falls on the first side lobe of the second airy pattern. If two airy patterns are closers than this, they are indistinguishable. Thus, the first minimum of the airy pattern ($I(x,y) = 0$; $J_1\left(\frac{\pi Dr}{\lambda f}\right) = 0$) defines the resolution limit of an imaging system. Since the first zero of the Bessel function occurs at 3.8317, the resolution limit of an imaging system in a medium of refractive index n (i.e. $\lambda \to \lambda/n$) can be approximated as

$$\left.\frac{\pi Dr}{\lambda f}\right|_{r=R} = 3.8317,$$
$$R = 1.22\frac{\lambda f}{nD} = 0.61\frac{\lambda}{nsin\alpha} = 0.61\frac{\lambda}{NA}, \qquad \textbf{Eq. 2.5}$$

where α is the half cone angle of the aperture (i.e. $sin\alpha = D/(2f)$) and NA is the numerical aperture of the lens. Hence, the theoretical resolution limit of a microscope only depends on the wavelength of the light and the numerical aperture of the objective lens. The higher the numerical aperture is, the better the resolution will be. Eq. 2.5 is, however, valid only for the special case of

a point source emitting monochromatic light detected by a perfect detection system. In real experiments, however, several factors increase the lower bound of the resolution, including aberration, light scattering, and asymmetry in the emission profile of the light source.

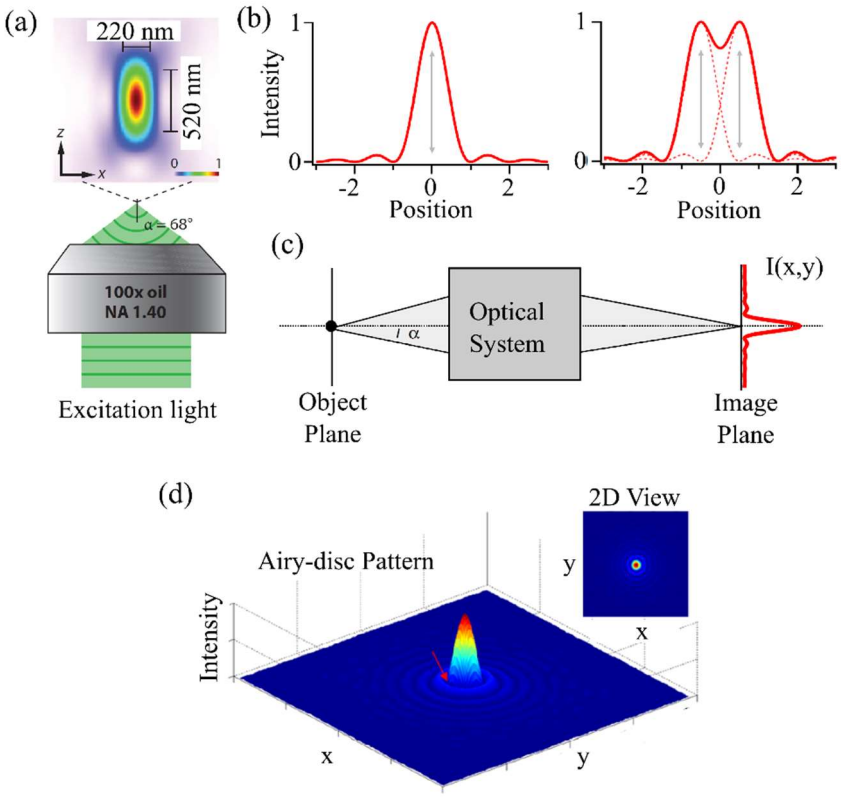

Figure 2.1 – The optical resolution limit. (a) Lateral and axial resolution in diffraction-limited optical microscopy. A numerically computed PSF in *x-z* plane of an oil-immersion objective lens showing the FWHM of 220 nm and 550 nm in lateral and axial directions, respectively. The wavelength of the excitation light used for computation: 550 nm [14]. **(b)** An isolated point spread function (on the left) and two point sources separated by d_{Abbe}. **(c)** Schematic of the imaging process, showing the point-spread function *I(x)* in the image plane. The maximum angle of rays collected, $\boldsymbol{\alpha}$, determines the numerical aperture (*NA*) [5]. **(d)** Classical Airy-disc pattern generated by a circular aperture [16].

2.2 Super-Resolution Microscopy Techniques

In order to overcome the optical resolution limit, a number of super-resolution fluorescence microscopy techniques have been developed in recent years, including single-molecule localization microscopy (SMLM) and stimulated emission depletion (STED) microscopy. SMLM is based on *engineering the prior*, i.e. precise molecular localization based on the prior knowledge that the single molecules are isolated. Some examples of SMLM are stochastic optical reconstruction microscopy (STORM) [10], direct STORM (dSTORM) [17, 18], photoactivated localization microscopy (PALM) [9] and universal point accumulation for imaging in nanoscale topography (uPAINT) [11]. Although these methods are slightly different from each other, they all exploit the photoswitchable nature of certain fluorophores to temporally and spatially separate the fluorophores' PSFs. The single fluorophores are then localized by evaluating their PSFs imaged on the detector [12].

Stimulated emission depletion (STED) microscopy [19, 20] is another super-resolution microscopy technique, which is based on *engineering the PSF*. It employs a non-linear saturation process for controlled de-excitation of fluorophores and sharpening the PSF. Simply speaking, it uses a second laser (STED laser) coupled with an excitation laser to suppress the fluorescence emission from the fluorophores located at the periphery of the excitation pattern [14]. Here, we briefly describe the concepts and techniques behind SMLM and STED microscopy.

2.2.1 Super-Resolution from Prior Engineering: Single-Molecule Localization Microscopy

SMLM is based on stochastic photoswitching of isolated fluorophores. This is achieved in two steps: first, the majority of fluorophores are transferred to a reversible 'OFF state' and then the individual fluorophores are stochastically activated (i.e. 'ON state') upon excitation by a laser with an appropriate wavelength and intensity (Figure 2.2a). To obtain an informative super-resolution

image, an image stack of thousands of images is typically required. Hence, this process of cyclic activation and readout of the emission of individual fluorophores is repeated continuously to accumulate millions of localizations. The super-resolution image is then reconstructed based on these localizations (Figure 2.2b-c).

The single-molecule fluorescence emission is collected using an objective lens with a high numerical aperture and then recorded on a sensitive detector, which is typically an electron multiplying charge-coupled device (EMCCD). Activated fluorophores are then localized by fitting a PSF model to the measured photon distribution (Figure 2.2d-e). Ideally, a SMLM experiment should be conducted such that only one single fluorophore emits within a diffraction limit at any time. This is achieved by maintaining a sufficiently low activation probability, where two adjacent activated fluorophores in the 'ON state' are further apart than the diffraction limit. Common to all SMLM methods is the need for photoswitchable fluorophores with a fluorescent 'ON state', a non-fluorescent 'OFF state' and a transition between these two states (Figure 2.2f-g). The strengths and limitations of various SMLM methods have been comprehensively discussed [21, 22].

The labeling density can become a limiting factor for effective spatial resolution in SMLM. The effect of labeling density on the effective resolution can be quantified by Nyquist-Shannon criterion [23], which states that the mean distance between neighboring localized fluorophores must be at least twice as fine as the desired resolution. Therefore, structural features smaller than two times the fluorophore-to-fluorophore distance cannot be clearly resolved [24]. The number of emitted photons per photo-switching event, the duty cycle of the fluorophores, the formation of the stable 'OFF state', and the tunable switching rate between 'ON' and 'OFF states' (i.e. $r = \tau_{OFF} / \tau_{ON}$) are among the key factors that directly influence the quality of the super-resolution image [25, 26]. The photoswitching rate of fluorophores and the lifetime of the 'OFF state' in

dSTORM can be optimized to an extent by adjusting the activation laser intensity and the excitation laser intensity, respectively. The concentration of the reducing agents such as β-mercaptoethylamine (MEA) and the pH value of the solvent also influence the duty cycle and photoswitching rate of fluorophores [17, 27, 28]. A summary of switching properties of the most commonly used fluorophores in SMLM is given in Table 2.1.

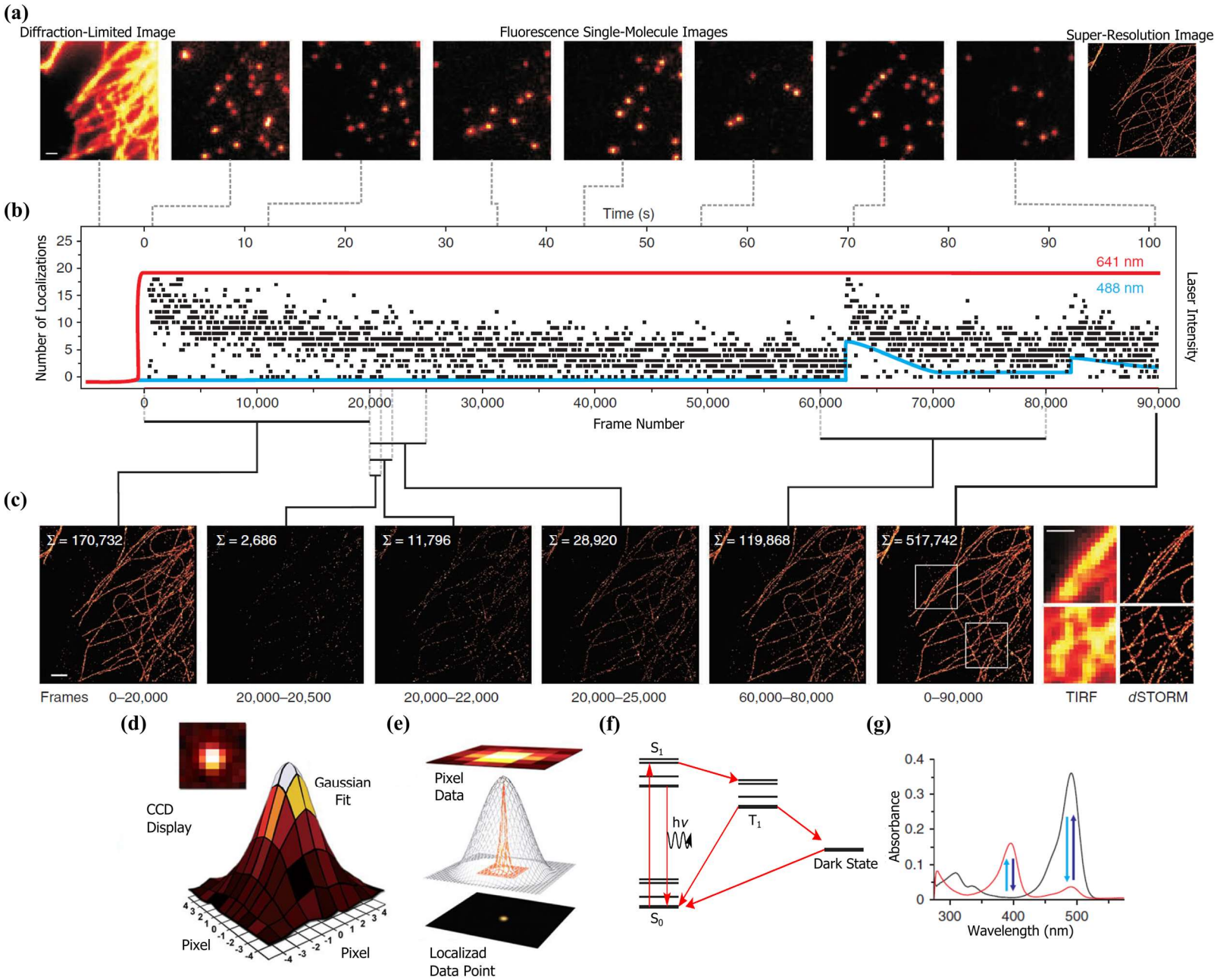
(a)
Diffraction-Limited Image
Fluorescence Single-Molecule Images
Super-Resolution Image
(b)
Time (s)
Number of Localizations
641 nm
488 nm
Laser Intensity
Frame Number
(c)
Σ = 170,732
Σ = 2,686
Σ = 11,796
Σ = 28,920
Σ = 119,868
Σ = 517,742
Frames 0–20,000
20,000–20,500
20,000–22,000
20,000–25,000
60,000–80,000
0–90,000
TIRF
dSTORM
(d)
CCD Display
Gaussian Fit
Pixel
Pixel
(e)
Pixel Data
Localizad Data Point
(f)
S1
hν
T1
Dark State
S0
(g)
Absorbance
Wavelength (nm)

Figure 2.2 – Principles of single-molecule localization microscopy. An example of SMLM acquisition procedure. A diffraction-limited image of the structure (Alexa Fluor 647–labeled β-tubulin in a COS-7 cell) is obtained at low excitation intensity. A higher irradiation intensity is then applied to transfer the majority of fluorophores into a non-fluorescent 'OFF state' until a sufficiently low spot density is reached. Finally, a super-resolved image is reconstructed from all localizations. **(b)** Number of localizations per frame. The direct excitation of the 'OFF state' at 488 nm (blue line) acts to increase the number of fluorophores in the 'ON state'. **(c)** The super-resolution image reconstruction [29]. **(d)** An example of actual intensity data from a single emitter captured by an EMCCD and characterized using a Gaussian fit. **(e)** Captured pixel data and the subsequent localization with a sub-diffraction precision [30]. **(f)** Photo-physics of organic fluorophores. A modified Jablonski diagram including intersystem crossing to the first triplet state and transition to a generic dark state [31]. **(g)** Absorption spectra of Alexa Fluor 488 in PBS (pH 9.3) in the presence of 100 mM MEA. After irradiation at 488 nm (light blue), the absorption at 488 nm decreases and radical anion absorption occurs maximally around 400 nm. The fluorescent state is recovered spontaneously or by direct excitation of the radical anion at ~400 nm (dark blue) [29]. Σ denotes the cumulative number of localizations used to reconstruct the dSTORM image. Scale bar: 1 μm.

Table 2.1 - Summary of switching properties of the most commonly used fluorophores in SMLM [1].

					Detected photons per switching event		Equilibrium on-off duty cycle (400–600 s)		Survival fraction after illumination for 400 s		Number of switching cycles (mean)	
Dye	Excitation maximum (nm)[a]	Emission maximum (nm)[a]	Extinction (M^{-1} cm^{-1})[b]	Quantum yield[c]	MEA	βME	MEA	βME	MEA	βME	MEA	βME
Blue-absorbing												
Atto 488	501	523	90,000	0.8	1,341	1,110	0.00065	0.0022	0.98	0.99	11	49
Alexa Fluor 488	495	519	71,000	0.92	1,193	427	0.00055	0.0017	0.94	1	16	139
Atto 520	516	538	110,000	0.9	1,231	868	0.0015	0.00061	0.92	0.86	9	17
Fluorescein	494	518	70,000	0.79	1,493	776	0.00032	0.00034	0.51	0.83	4	15
FITC	494	518	70,000	0.8	639	1,086	0.00041	0.00031	0.75	0.9	17	16
Cy2	489	506	150,000	0.12	6,241	4,583	0.00012	0.00045	0.12	0.19	0.4	0.7
Yellow-absorbing												
Cy3B	559	570	130,000	0.67	1,365	2,057	0.0003	0.0004	1	0.89	8	5
Alexa Fluor 568	578	603	91,300	0.69	2,826	1,686	0.00058	0.0027	0.58	0.99	7	52
TAMRA	546	575	90,430	0.2	4,884	2,025	0.0017	0.0049	0.85	0.99	10	59
Cy3	550	570	150,000	0.15	11,022	8,158	0.0001	0.0003	0.17	0.55	0.5	1.6
Cy3.5	581	596	150,000	0.15	4,968	8,028	0.0017	0.0005	0.89	0.61	5.7	3.3
Atto 565	563	592	120,000	0.9	19,714	13,294	0.00058	0.00037	0.17	0.26	4	5
Red-absorbing												
Alexa Fluor 647	650	665	239,000	0.33	3,823	5,202	0.0005	0.0012	0.83	0.73	14	26
Cy5	649	670	250,000	0.28	4,254	5,873	0.0004	0.0007	0.75	0.83	10	17
Atto 647	645	669	120,000	0.2	1,526	944	0.0021	0.0016	0.46	0.84	10	24
Atto 647N	644	669	150,000	0.65	3,254	4,433	0.0012	0.0035	0.24	0.65	9	39
Dyomics 654	654	675	220,000	–	3,653	3,014	0.0011	0.0018	0.79	0.64	20	19
Atto 655	663	684	125,000	0.3	1,105	657	0.0006	0.0011	0.65	0.78	17	22
Atto 680	680	700	125,000	0.3	1,656	987	0.0019	0.0024	0.65	0.91	8	27
Cy5.5	675	694	250,000	0.28	5,831	6,337	0.0069	0.0073	0.87	0.85	16	25
NIR-absorbing												
DyLight 750	752	778	220,000	–	712	749	0.0006	0.0002	0.55	0.58	5	6
Cy7	747	776	200,000	0.28	852	997	0.0003	0.0004	0.48	0.49	5	2.6
Alexa Fluor 750	749	775	240,000	0.12	437	703	0.00006	0.0001	0.36	0.68	1.5	6
Atto 740	740	764	120,000	0.1	779	463	0.00047	0.0014	0.31	0.96	3	14
Alexa Fluor 790	785	810	260,000	–	591	740	0.00049	0.0014	0.54	0.62	5	2.7
IRDye 800 CW	778	794	240,000	–	2,753	2,540	0.0018	0.038	0.6	1	3	127

Excitation wavelength, dichroic mirrors and emission filters used for characterization and imaging for each spectral range were 488 nm, T495LP (Chroma) and ET535/50m (Chroma) for blue-absorbing dyes; 561 nm, Di01-R561 (Semrock) and FF01-617/73-25 (Semrock) for yellow-absorbing dyes; 647 nm, Z660DCXRU (Chroma) and ET700/75m (Chroma) for red-absorbing dyes; 752 nm, Q770DCXR (Chroma) and HQ800/60m (Chroma) for NIR-absorbing dyes, respectively. Dye-switching properties are reported in the presence of GLOX and 10 mM MEA as well as GLOX and 140 mM βME.
[a]Excitation and emission peak wavelengths from dye spectra. [b]Extinction coefficients from the dye manufacturers. [c]Quantum yields from either the dye manufacturer when known or from the McNamara 2007 fluorophore data tables. –, quantum yield values not available from dye manufacturer or McNamara data tables.

2.2.2 Super-Resolution by PSF Engineering: Stimulated Emission Depletion (STED) Microscopy

The concept of STED microscopy was first proposed in 1994 [20] and a few years later the theoretical concept was demonstrated experimentally [32]. STED microscopy is based on the depletion of the molecular fluorescence state through stimulated emission. In brief terms, it uses a second laser (i.e. STED laser) to suppress the fluorescence emission from the fluorophores located in the periphery of the excitation pattern (Figure 2.3a). When a fluorophore in its excited state encounters a photon that matches the energy difference between the excited and ground state, it can be brought back to the ground state through stimulated emission before spontaneous fluorescence emission can occur (Figure 2.3b). Therefore, the excited state fluorophores capable of fluorescence emission are effectively depleted (Figure 2.3c-d).

STED microscopy sharpens the excitation PSF using a spatially patterned laser that has zero intensity at the center and non-zero intensity at the periphery. This pattern is typically generated by introducing a phase mask into the depletion laser path to modulate the spatial phase distribution of the depletion beam (Figure 2.3e). The key to achieving high resolution here is the non-linear dependence of the depleted population on the laser intensity when the saturation intensity is approached [33].

In principle, the majority of the spontaneous fluorescence emission can be suppressed if the local intensity of the STED laser is higher than a certain value. By increasing the STED laser intensity, the region experiencing the saturation depletion expands without affecting the fluorescence emission from the focal point as the STED laser intensity is close to zero at the focal point. As a result, the fluorescence emission can be detected from only a small area around the focal point, leading to a significant decrease in the FWHM of the PSF. The super-resolution images

can be therefore obtained by scanning this reduced PSF in 2D and 3D [14, 34]. Consequently, the resolution (d) in STED microscopy is limited by the intensity of the STED laser rather than the diffraction of light and is given by [33]

$$d = \frac{\lambda}{NA\sqrt{1 + \frac{I}{I_{sat}}}} \qquad \textbf{Eq. 2.6}$$

where I is the power of the depletion laser and I_{sat} is a fluorophore-dependent parameter corresponding to the laser power required to deplete 50% of the fluorescence (Figure 2.3d). Dyes with high photostability and large stimulated emission cross sections in the visible to near infrared range, such as Atto 532 and Atto 647N, are preferred for STED microscopy. The theory of STED microscopy has been comprehensively discussed [5, 33]. STED microscopy with a resolution of about 20-50 nm has been achieved and has determined the location of fluorescent antibody labeled proteins in fixed tissues [35]. It has observed the movement of neurotransmitter vesicles inside associated neurons [36] and it has imaged dendritic spines of the brain [37]. STED provides the best performance in non-scattering environments or near the surface of scattering tissues. In the case of fluorophore excitation via two-photon processes, however, STED microscopy is less sensitive to absorption and scattering, which makes it a suitable tool for

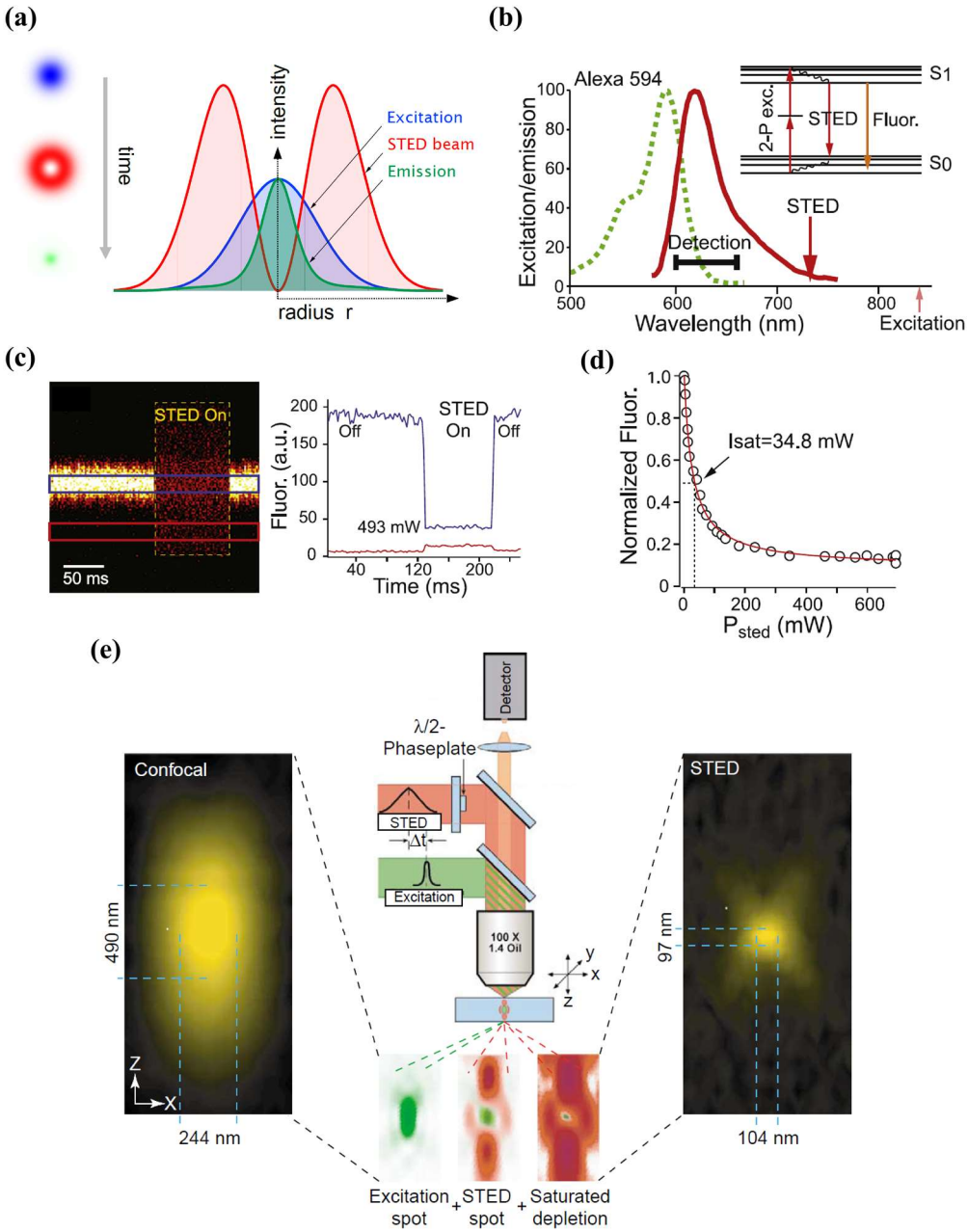

Figure 2.3 - Principles of STED microscopy. (a) An intensity profile illustrating the broad excitation pulse (blue), the doughnut-shaped STED depletion beam (red), the narrow emission pulse (green), and temporal sequence of beams [5]. **(b)** One-photon excitation and fluorescence emission spectra of Alexa 594, indicating the depletion wavelength of 736 nm in the far red region of the emission spectrum. Inset: A simplified energy diagram of two-photon excitation and one-photon depletion. **(c)** Fluorescence measured in line scans over the region indicated by the rectangle during normal excitation and with additional illumination with 760 nm light (boxed region) (left) and quantification of fluorescence intensity in the regions of interest (ROI) indicated by the colored boxes (right). **(d)** Depletion of Alexa 594 fluorescence under constant two-photon excitation with 840 nm light as a function of the power (P_{sted}) of applied 736 nm depletion light [34]. **(e)** Schematic of the optical path for modulation and combination of the excitation (green) and depletion (light red) laser light. Note the difference in full width at half maximums (FWHM) of the PSFs [33].

researchers in neuroscience, where the nature of their studies require imaging in deep tissue or in a a highly-scattering environment [34].

2.3 The Fundamental Limit of Resolution in Single Molecule Localization Microscopy

The resolution in SMLM is closely related to both the localization precision and the localization accuracy. Determining the precision and the accuracy with which a single molecule can be localized is integral in quantitative analyses of SMLM data. This is imperative because it determines not only the theoretical limit of resolution achievable in SMLM, but it also provides an answer to an important practical question: what types of studies can essentially be carried out using SMLM?

Using the point-spread function (PSF) of an isolated single molecule, one can estimate its positional coordinates with relative certainty. If the position of an isolated single molecule (with a true coordinate of x) is measured n times (x_i; $i = 1; n$), the localization accuracy describes the deviation of the mean of the measurements ($\bar{x}$) from the true position whereas the localization precision denotes the spread of these measurements around the mean value (Figure 2.4a). The localization precision of a single molecule in the *x* direction is commonly expressed in terms of a standard deviation, which is given by $\sigma_x = \sqrt{\frac{1}{n-1}\sum_{i=1}^{n} (x_i - \bar{x})^2}$.

Several approaches have been proposed to determine the theoretical limit of localization precision in SMLM, including the ones proposed by Kubitscheck *et al.* [38], Thompson *et al.* [39], Cheezum *et al.* [40], Ober *et al.* [41] and Huang *et al.* [42]. Despite the differences among these approaches, nearly all of them are based on the following principles:

a) a model for the photon emission process of a single molecule

b) a noise model for the detection device (e.g. a comprehensive model for dark noise, read noise, and excess noise in the case of an electron multiplying charge coupled device (EMCCD))

c) an image formation function (i.e. a mathematical model for the point spread function (PSF) of single fluorophore)

d) an estimation algorithm for the localization of a single molecule.

The analytical approach proposed by Ober *et al.* [41] is presented here. It provides a simple expression for the fundamental limit of localization precision for single molecules and demonstrates how this limit is influenced by the photon emission rate (k), the wavelength of photon emission (λ), the photon-detection efficiency of the optical system (η), the numerical aperture of the objective lens (n_a), and the acquisition time (t).

Consider a simple two-dimensional imaging system with a unit magnification ($M = 1$) and incoherent and monochromatic photon emission. A single molecule located at the focal plane of the objective lens forms an image on a planar detector with a point spread function $q(x, y)$. $\theta = (u, v)$ denotes the molecular coordinates in the object plane. Rays are collected at the maximum angle α using an objective lens with a numerical aperture of n_a. The single molecule is considered a point source emitting photons in a stochastic process modeled by Poisson distribution. It is assumed that the detected photons on the image plane are independent and identically distributed random variables with a density function $f_\theta = (1/M^2)\, q(\mathrm{r}/\mathrm{M} - \theta)$, where $r \in R^2$ and q can be an Airy function or a Gaussian point-spread function.

The limit of localization precision for u coordinate of the single molecule can be calculated using the Cremer-Rao lower bound (CRLB) [43], which states that a lower bound for the variance ($var(\theta)$) of any unbiased estimator is the inverse of the Fisher information matrix ($I^{-1}(\theta)$),

$$var(\theta) \geq I^{-1}(\theta). \qquad \textbf{Eq. 2.7}$$

The inverse of the Fisher information matrix can therefore be interpreted as a lower limit for the variance of the estimation procedure in single molecule localization. Here, we calculate $\sqrt{I^{-1}(\theta)}$, since the precision limit (i.e. standard deviation of the estimator) is of interest, not the variance. The Fisher information matrix is expressed as

$$I(\theta) = \eta\, \mathrm{E}[N(t)] \int_{R^2} \frac{1}{q(x,y)} \left[\frac{\partial q(x,y)}{\partial x}, \frac{\partial q(x,y)}{\partial y}\right]^T \left[\frac{\partial q(x,y)}{\partial x}, \frac{\partial q(x,y)}{\partial y}\right] dxdy, \qquad \textbf{Eq. 2.8}$$

where $\mathrm{E}[N(t)]$ is the expected number of photons detected during acquisition time (i.e. $\mathrm{E}[N(t)] = \eta\mathrm{At}$). In the case of a Gaussian point-spread function, $q(x,y)$ is given by $q(x,y) = (1/(2\pi\sigma_g))\ \exp(-(x^2+y^2)/(2{\sigma_g}^2))$, where σ_g is the standard deviation of the Gaussian function ($FWHM = 2\sqrt{2ln2}\sigma_g$) and is estimated by Abbe's diffraction limit as $\sigma_g = \lambda/(2n_a)$. As a result of the symmetry of Gaussian profiles (i.e. $q(-x,y) = q(x,-y)$), the off-diagonal entries of the Fisher information matrix vanish and the generalized precision limit for u coordinate of the single molecule (σ_u) is given by

$$I(\mathrm{u}) = \sigma_u = \mathrm{E}[N(t)] \int_{R^2} \frac{1}{q(x,y)} \left[\frac{\partial q(x,y)}{\partial x}\right]^2 dxdy$$

$$= \frac{\eta\mathrm{At}}{{\sigma_g}^4}\left(\left(\frac{1}{\sqrt{2\pi}\sigma_g}\right)\int_{\mathrm{R}} x^2 e^{\frac{-x^2}{2{\sigma_g}^2}} dx\right)\left(\left(\frac{1}{\sqrt{2\pi}\sigma_g}\right)\int_{\mathrm{R}} e^{\frac{-y}{2{\sigma_g}^2}} dy\right) = \frac{\eta\mathrm{At}}{{\sigma_g}^2}\ . \qquad \textbf{Eq. 2.9}$$

which essentially demonstrate that the lower bound for the localization precision of single molecule localization for a Gaussian PSF is $\sigma_u \geq \sigma_g/\sqrt{\eta\mathrm{At}} = \sigma_g/\sqrt{\mathrm{E}[N(t)]}$, or simply

$$\sigma_u \geq \sigma_g/\sqrt{\mathrm{N}}. \qquad \textbf{Eq. 2.10}$$

This result implies that the localization precision can be improved by a factor of two if one increases the number of photons detected by four times, or halves the emission wavelength, or doubles the numerical aperture of the objective lens. In practice, however, there are several experimental and computational factors, which make the theoretical limit of precision very difficult to achieve, or virtually impossible. They not only increase the CRLB but also rigorously degrade the imaging accuracy. These factors include the detector pixellation and noise, sample drift, label displacement, asymmetry in the emission pattern of the fluorophore, and computational errors in the single-molecule localization algorithms. Brief descriptions of some of these factors are in the following sections.

2.3.1 Camera Pixelation and Noise

A theoretical image of an isotropic light emitter with a sub-diffraction size on an ideal detector, which is noise-free and has no pixelation, would be a disk surrounded by diffraction rings centered on the coordinates of the emitter. The imaging detectors, however, come with pixels and can record the coordinates of a detected photon only up to the size of a pixel. This limits the localization precision achievable on a detector because the real position of the detected photon on the detector is unknown (i.e. the sub-pixel information is missing) [41, 44].

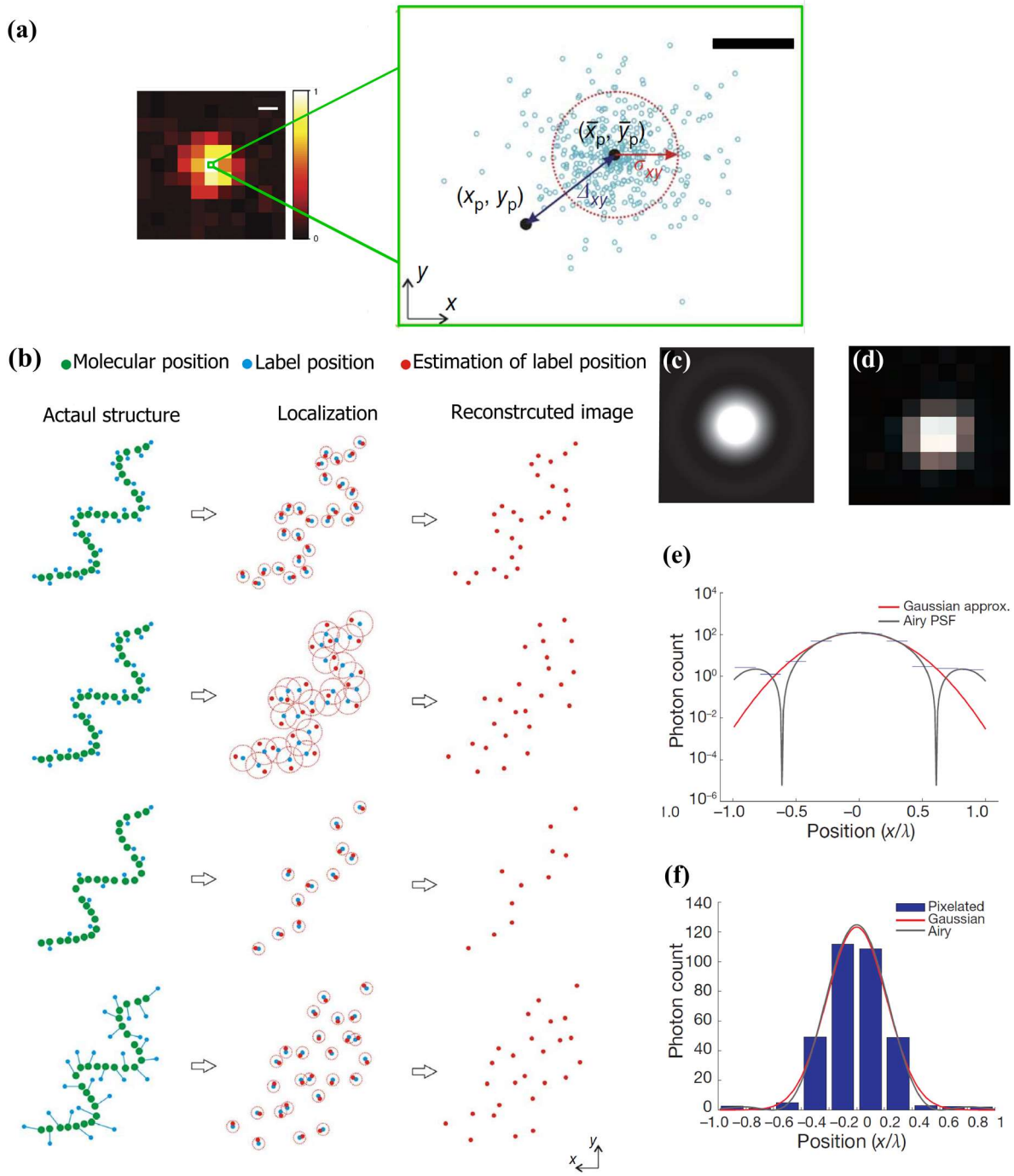

Figure 2.4 – Localization precision and accuracy in SMLM. (a) The real particle position (x_p, y_p) can be estimated from the image of the fluorophore's PSF with a lateral localization precision σ_{xy} and a lateral localization accuracy Δ_{xy}. The blue circles denote experimentally determined position estimates from different images of the same emitter and (x_p, y_p) is the average of these individual values. **(b)** Influence of localization precision, label density, and label displacement on the resolution of a localization microscopy image. The localization microscopy image faithfully represents the actual structure only when the localization precision and label density are sufficiently high and the label displacement is sufficiently small [45]. **(c)** The PSF of a fluorophore simulated using the Richards-Wolf model. The image is two wavelengths across. **(d)** The image in **(a)** pixelated with one-fifth–wavelength pixels, and with shot noise (assuming 1,000 total photons in the image). **(e)** Cross section of the pixelated image and approximate Airy and Gaussian models for comparison. The widths of the model PSFs are based on standard theoretical models [37]. The heights are proportional to the photon count in the image. **(f)** Same as **(d)** but shown on a logarithmic scale to emphasize the discrepancy in the tails [46].

There is, however, a trade-off between the pixel size on the detector and the localization precision. A very large pixel size on the detector can result in an undersampling of the PSF of the single molecule, which degrades the localization precision. On the other hand, smaller pixels detect fewer photons, which decreases the signal to noise ratio. Thus, the total magnification of an imaging system should be adjusted such that the pixel size provides sufficient sampling of the PSFs of the single molecules. According to the Nyquist–Shannon sampling theorem, the best performance is achieved when the full width at half maximum (FWHM) of the PSF spans about three pixels on the camera [42, 45]. This translates into a pixel size of 100-150 nm/px, depending on the specifications of the imaging system [4, 47].

In addition to the shot noise, which is due to the finite number of photons emitted from the fluorophores and the Poisson distribution of the emission pattern, there is other noise associated with cameras, including the dark noise, the readout noise, the excess noise, and the pattern noise. These sources of noise further reduce the localization precision in SMLM. The thermally induced dark current introduces a Poisson distributed background in charge-coupled devices (CCD) and complementary metal-oxide semiconductor (CMOS) detectors, especially at long exposure times. The dark noise is temperature-dependent and is decreased significantly by cooling down these cameras to < -30 ºC. Current electron multiplying CCDs (EMCCDs) can be easily cooled down to ~ -80 ºC using a coolant, effectively eliminating dark noise and its effects on the localization precision. The readout noise, which is due to an imperfect digitization of electron counts, is an issue with CCD and CMOS cameras when extremely low numbers of photons are detected. The on-chip electron multiplication process (i.e. EM gain) in EMCCD cameras removes the readout noise efficiently even at very high readout rates (e.g. < 1 e^- at 17 MHz). However, the stochastic nature of electron multiplication processes result in excess noise. Any inconsistency in the

behavior of pixels and amplifiers in a camera leads to pattern noise, which results in an asymmetric photon emission pattern of the emitter on the camera [42, 44, 46].

Generally, the image quality of a camera can be described by the signal-to-noise ratio (SNR). For an input number of photons, N, the SNR is estimated as [48, 49]

$$SNR = \frac{N * QE}{\sqrt{QE * (N + b) * F_n^2 + (N_r/M)}}, \qquad \textbf{Eq. 2.11}$$

where QE is the quantum efficiency of the camera, b is the background noise (i.e. the background fluorescence and the residual excitation photons), N_r is the readout noise, and M is the EM gain factor. EM gain occurs in a voltage-dependent, step-wise manner and has a statistical distribution and associated variance, which is accounted for by the noise factor, F_n ($F_n = \sqrt{2}$ for EMCCD; $F_n = 1$ for CCD and CMOS). According to Eq. 2.11, the SNR for a perfect camera is limited only by the shot noise (i.e. $SNR = \sqrt{N}$). Any additional noise leads to a lower SNR. The SNR of CCD cameras approach that of an ideal camera when high numbers of photons are detected (Figure 2.5a). Due to the noise factor in EMCCDs, the maximum SNR that can be achieved using an EMCCD is ~ 0.67 that of a perfect camera (Figure 2.5b). The EMCCD camera is, however, an appropriate choice for imaging experiments, which deal with a very low number of photons at high acquisition rates. CCD cameras are the ideal choice for imaging when low acquisition rates with high numbers of detected photons are the conditions present (Figure 2.5b). More comprehensive reviews of camera noise and their effects on localization precision can be found in the references [42, 45, 47]. Considering the camera pixelation and noise, a more realistic model for the limit of localization precision in SMLM has been proposed by Moertensen *et al.* [44], which is expressed as

$$\sigma_x = F_n^2 \left[\frac{16(w^2 + a^2/12)}{9N} + \frac{8\pi b^2 (w^2 + a^2/12)^2}{a^2 N^2} \right], \qquad \textbf{Eq. 2.12}$$

where w is the width of the PSF, a is the pixel size and b is the standard deviation of the background noise.

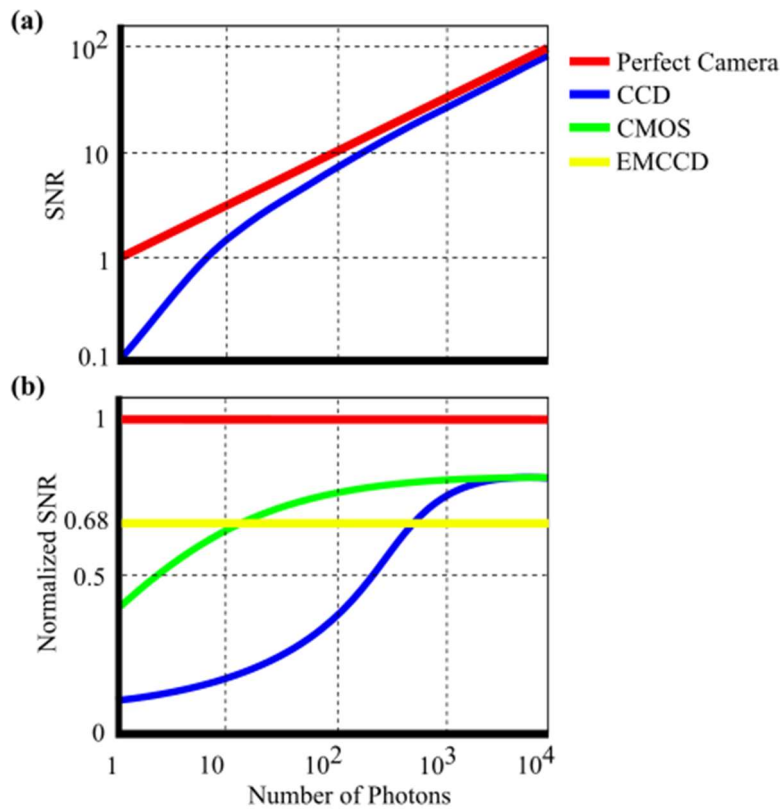

Figure 2.5 - Signal to noise ratio of different cameras. (a) SNR of a perfect camera vs. SNR of a CCD. **(b)** Normalized SNR in different cameras.

2.3.2 Imaging System Instability

Sample drift on the order of tens of nanometers is inevitable. Drift has a random nature and is caused by temperature fluctuations, mechanical relaxation, and mechanical vibrational. This results in an asymmetry in the emission pattern of the single molecule and flattens the PSF pattern on the detector [44, 46, 50, 51].

Considering the length of time required for image acquisition in a typical SMLM experiment (i.e. 10-30 min), the overall effects of imaging system instability on the localization accuracy could be tremendous. It takes away from the main objective of super-resolution microscopy to image the structure of interest at very high spatial resolutions down to a few nanometers. Drift can be minimized by relating all localizations to the position of a fiducial marker embedded in the sample as a reference point [51, 52]. Cross correlation analysis of the bright-field images [53] or the tracking of single molecules [54] are the other approaches to correct for the drift in SMLM.

2.3.3 Label Density and Probe Size

Insufficient labeling density (i.e. the fraction of target molecules labeled) in SMLM leads to artifacts in the super-resolution image such that the structure of interest is not reconstructed meaningfully or continuous structures may be represented as discontinuous structures (Figure 2.4b). The effect of labeling density on the localization precision can be quantified by Nyquist-Shannon criterion [23], which state that the mean distance between neighboring localized fluorophores must be at least twice as fine as the desired resolution. Thus, structural features smaller than two times the fluorophore-to-fluorophore distance cannot be clearly resolved [24]. The smallest resolvable feature size, $\Delta_{Nyquist}$, is given by

$$\Delta_{Nyquist} = 2C^{-1/D} \qquad \textbf{Eq. 2.13}$$

where C is the labeling density and D is the dimension of the structure of the interest. According to Eq. 2.13, a labeling density of 10^4 μm^2 is required to achieve a two-dimensional super-resolution image with a resolution of 20 nm. However, due to the geometry of biological samples, a lower concentration of labeling fluorophore is experimentally sufficient to achieve reliable localizations [12, 14].

Any chemical moiety used to attach the label to the target molecule can affect the localization accuracy (Figure 2.4b). For instance, the combination of primary and secondary antibodies used in labeling microtubules increase the diameter of the structure from 25 nm to 60 nm [55, 56]. Using smaller probes, such as Fab fragments (~6 nm in size) and fluorescent proteins (~4 nm in size), one can significantly improve the localization accuracy in SMLM [4, 45, 46]. The ultimate goal in SMLM is to directly label the structure of interest using organic fluorophores, which are ~1 nm in size [14].

2.3.4 Single-Molecule Localization Algorithms

Various methods have been proposed for analyzing single molecule localization data [57-60] but nearly all of them follow the same basic workflow. The raw data (typically 10-40K images) are loaded into the program. Images are filtered and features are enhanced. The approximate positions of fluorophores are then estimated according to the local maximum pixel intensity of the PSF pattern. Decoding the 3D positions of molecules with subpixel accuracy is the next step. The method used here depends on the imaging technique. For example, in astigmatism-based imaging, the lateral positions are determined by fitting a Gaussian function to the intensity profile and the axial position can be calculated using the ratio of the widths of the PSF in the x to that in the y direction. Then, a table of data containing the information on x, y, z, error in x, error in y, error in z, frame number, and number of photons for each blink is generated. This table is then processed

and filtered according to user-defined filter settings. Finally, the remaining localization data is used to render a 3D super-resolution image.

Single-molecule localization can be treated as a statistical problem, where a fitting model is developed to correlate the pixel intensity, $I(x, y)$, to the fluorophore's coordinates, emission rate, background noise, and imperfections in the optical systems (such as aberration) [44-46]. Varying the model's parameters, one can then find the values that render the best fit to the measured PSF of the fluorophore. The fit is typically evaluated either by the least-square (LS) criterion [41, 61] or the maximum likelihood criterion [41, 61]. The fitting model can be generally expressed as

$$I(x, y) = I_0 H\left(x - x_{0,}\, y - y_0\right) + b, \qquad \textbf{Eq. 2.14}$$

where I_0 is the amplitude (i.e. the peak value of the intensity profile) and $H(x, y)$ is the PSF model, which describes the shape of the blur formed on the detector when a point source is imaged. (x_0, y_0) are the fluorophore's coordinates, and b is the average background noise per pixel.

As a result of the errors in the approximation of the PSF of an imaging system as well as the shot noise in the detected photons on the detector, single-molecule localization algorithms can deteriorate and influence the localization precision and accuracy. In order to achieve a high-accuracy PSF model, such as Richards-Wolf [62] or Gibson-Lanni [63] models, the numerical aperture of the objective lens, the refractive index mismatch between the objective lens and the imaging medium, the aberration induced by the sample and optical elements, and the dipole moment should be considered. Due to their simpler mathematical formulations, however, the Airy and the Gaussian functions are typically used in modeling the PSFs of the imaging systems. Although these models are good approximations that hold in many situations, they are not necessarily valid if the PSF of the single molecules are asymmetric due to aberration, random scattering, or the dipole effect [46, 64].

In addition, because of the shot noise, the emitted photons are not smoothly distributed over the detector area (i.e. they arrive at random positions). This is similar to adding noise to an ideal image of a fluorophore, which leads to the deviation of the fluorophore's image on the camera from the ideal PSF model (Figure 2.4e-f). Thus, every single image of a fluorophore on the camera possesses a slightly different center, which results in additional error in the localization of the single molecule. This error can be measured by the standard deviation of the estimates, as discussed by Deschout *et al.* [45].

Chapter 3: Single Molecule Localization Deep Within Thick Cells

Three-dimensional (3D) super-resolution imaging based on astigmatic single-molecule localizations has been gaining popularity, but high accuracy deep imaging still faces many challenges. In single-molecule localization microscopy (SMLM), an acquisition time of several minutes is often needed to accumulate a sufficient number of fluorophore positions and construct an informative image. The lateral accuracy of the fluorophore localization in a single image can be better than 10 nm, but sample drift due to thermal gradients or mechanical motion can be easily in the hundreds of nanometers. Therefore, stability often becomes the most important factor determining the performance of a SMLM system. To correct the drift, several approaches have been proposed, including online correction using fiducial markers [51, 65] as well as offline processing algorithms using a bright-field image [53, 66] or consecutive blink tracking [50, 54]. While large drifts cannot be properly corrected using offline processing algorithms, real-time drift correction using fiducial markers has produced the best super-resolution images because the position of a bright fiduciary marker can be determined within an error of a few nm [65]. Fiducial markers, typically fluorescent beads affixed to the coverslip, are used as reference points to measure and correct the drift. However, when the focal plane moves beyond ~ 0.5 μm (the typical depth of field of an objective lens with a high numerical aperture) into the cell, the fiducial markers on the coverslip are out of focus making a drift-free image difficult to obtain.

Another challenge for deep imaging using 3D SMLM is refractive index mismatch which produces a depth-dependent point spread function (PSF). Oil immersion objective lenses are often used for single-molecule based super-resolution microscopy because of their higher numerical apertures (NA) which collect more photons and leads to a higher accuracy for fluorophore localization. However, because of the refractive index mismatch between the oil (n = 1.51) and the

cells (n = 1.35-1.40), both the PSF and the astigmatism used to determine a fluorophore's depth become depth-dependent. This refractive index mismatch leads to a false depth localization when imaging a few micrometers deeper than the coverslip. The issue can be partially corrected using theoretical calculations [67, 68], but they are non-trivial and do not account for imperfections in the optical components.

In this chapter, we demonstrate a SMLM system with two independent, variable, focal planes for deep 3D super-resolution imaging enabling real-time nanometer-scale drift correction using fiducial markers on the coverslip. We also present a method to obtain an empirical (rather than theoretical) correction for refractive index mismatches, and the depth-dependent astigmatism that results. This method compensates for imperfections in all of the optical components that cannot be accounted for otherwise. Additionally, we show that when the sample has regions where the fluorophores have a very high local density, the resulting high local blinking rates can generate artefacts that cannot be removed using existing techniques. The methodology presented here leads to a far more accurate positioning of the blinks and to an image that more faithfully represents the labeled structure. While the images presented in this paper were obtained using direct stochastic optical reconstruction microscopy (dSTORM), the methodologies described here are applicable to other SMLM techniques, such as STORM, PALM, FPALM, GSDIM, etc.

3.1 Materials and Methods

3.1.1 Optical Setup

All experiments were performed on a home-built inverted microscope (Figure 3.1a) equipped with an apochromatic TIRF oil-immersion objective lens (60×; NA 1.49; Nikon Instruments, Melville, NY). A 405 nm laser (Thorlabs, Newton, NJ) and a 639 nm lasers (Genesis MX639, Coherent, Santa Clara, CA) were used for activation and excitation of the Alexa 647 fluorophore (Life

Technologies, Burlington, ON), respectively. Excitation of the fiducial markers (diameter 100 nm; F8800, Life Technologies) was provided by a 532 nm laser (Excelsior One, Spectra-Physics, Santa Clara, CA). Laser beams were collimated, combined, circularly polarized and focused onto the back aperture of the objective lens (DM1: FF458-Di02, DM2: FF560-FDi01, Semrock, NY; QWP: AQWP05M-600, L: AC254-150-A, Thorlabs). A translational stage was used to shift the incident beam for oblique incident excitation. A quad-band polychroic mirror (DM3: Di01-R205/488/532/636, Semrock) was used to reflect the laser beams and transmit the fluorescence signal. A long-pass dichroic mirror (DM4; FF640-FDi01, Semrock) was used to separate the fluorescence emission of Alexa 647 from that of the fiducial markers. In the Alexa 647 detection pathway, the emitted light passed through a cylindrical lens assembly (CL1; effective focal length (EFL) = 10 m), then through a band-pass filter (BPF1; FF01-676/37, Semrock) followed by a 200 mm tube lens (TL1; ACA254-200-B, Thorlabs) and imaged to a back-illuminated CCD camera (CCD1; iXon Ultra 897 BV, Andor, South Windsor, CT). A 2.5× compound lens (not displayed in Figure 3.1a) was placed between DM4 and CL1 to obtain an overall magnification of 150 times.

The detection path of the fiducial markers contained a relay imaging lens (RL1; AC254-100-A, Thorlabs). When the imaging depth was changed, the position of RL1 was adjusted to keep the fiducial markers in focus on CCD2. A 250 mm achromatic doublet lens (TL2; AC254-250-A, Thorlabs) was used to form an image of the fiducial markers at the back focal plane of RL1. The emitted light then passed through a cylindrical lens assembly (CL2; EFL = 2 m), a band-pass filter (BPF2; FF01-562/40, Semrock) and a 200 mm achromatic doublet lens (RL2; ACA254-200-B, Thorlabs) before being imaged by CCD2 (Newton 970 UBV, Andor). Astigmatism was introduced into both optical paths (CL1 and CL2) using a pair of concave and convex cylindrical

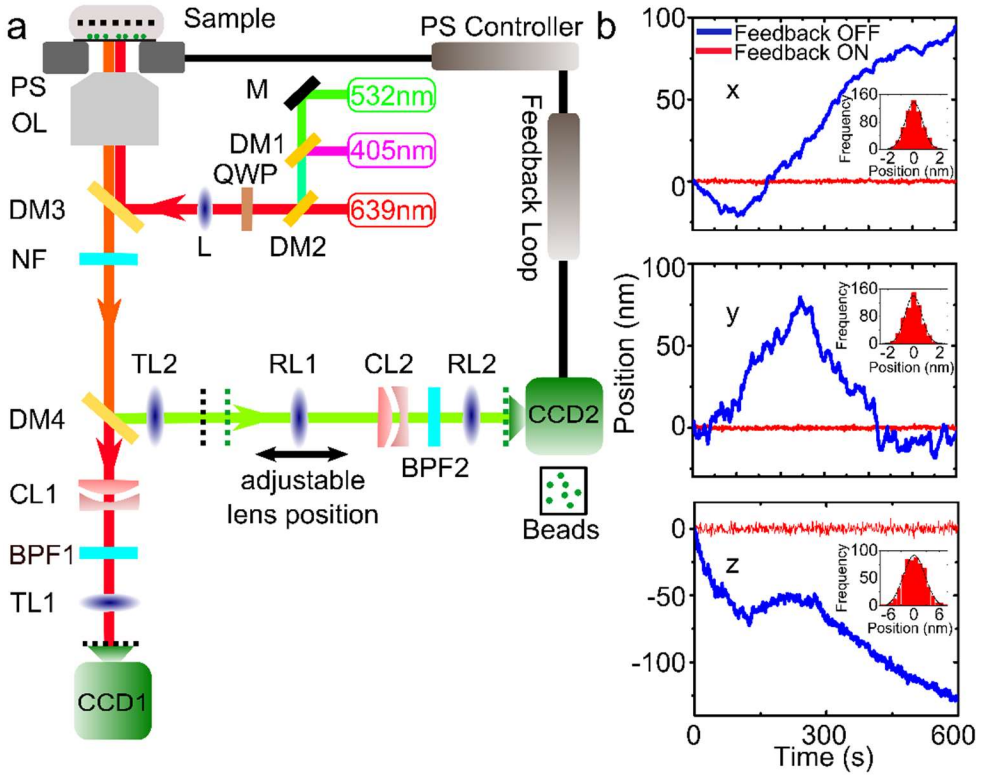

Figure 3.1 - Schematic layout of the optical setup. (a) A 639 nm laser was used for exciting fluorophores, and a 405 nm laser for reactivation. A 532 nm laser was used for exciting the fiducial markers. Lasers were combined using dichroic mirrors (DM1 and DM2), circularly polarized by a quarter-wave plate (QWP), focused and directed into the back aperture of the objective lens (OL). Fluorescence collected by the objective lens was separated by a dichroic mirror (DM3) and filtered using a notch filter (NF). The fluorescence signals from the cell and the fiducial markers were split using a dichroic mirror (DM4). In the bead tracking path, the fluorescence passed a tube lens (TL2) to form an image of the fiducial markers, and a relay lens assembly (RL1 and RL2) transferred the image of the fiducial markers into a camera (CCD2). A cylindrical lens assembly (CL2) introduces astigmatism enabling the 3D positions of the beads to be determined. These positions were used in a closed feedback loop for 3D stabilization of the microscope stage. A cylindrical lens assembly (CL1) and a tube lens (TL1) were used to form astigmatically aberrated images of the fluorophores onto CCD1. The black and green dashed lines indicate the focal planes of the cell (focused on CCD1) and the fiducial markers (focused on CCD2), respectively. The position of RL1 is adjusted to refocus the fiducial markers on CCD2 when the imaging depth of the sample changes on CCD1. The fluorescent signal passes through band-pass filters (BPF1 and BPF2) before entering each camera. (b) Performance of the real-time 3D stabilization system showing the lateral (x and y) and axial (z) positions of the fluorescent beads over 10 minutes with the feedback loop on (red curves) and off (blue curves). Insets show histograms of the bead's position in each direction. Standard deviations were 0.7 nm in x, 0.7 nm in y and 2.6 nm in z. Five fiducial markers on CCD2 were used for tracking. PS: piezo stage, M: mirror, L: spherical lens.

lenses (f = ±40 cm), in contrast to the single-cylindrical-lens design used by Huang *et al.* [69]. This approach allowed us to optimize the astigmatic effect for deep imaging.

3.1.2 Image Acquisition and Post Processing

The sample was first illuminated with relatively low intensities of the 639 nm and 532 nm lasers (< 2 W/cm^2 at sample). The imaging depth was recorded before acquiring the data. The position of RL1 was adjusted to obtain a clear image of the fiducial markers before turning on the feedback control. The intensity of the 639 nm laser was then increased to ~5 kW/cm^2, switching the dye molecules to their dark states. Images were then acquired at 50 frames per second with a minimum of 40,000 frames being required to construct the final image. The intensity of the 405 nm laser was ramped up (from 0 to 1 W/cm^2) during acquisition to reactivate dye molecules and compensate for a decreasing number of blinks due to photobleaching. The post-acquisition processing of images to determine the positions of single-molecules was performed using a software written in MATLAB (Figure 3.2).

To actively stabilize the microscope stage in 3D during the image acquisition, up to five different fiducial markers were used for tracking. Images of beads were subsequently fitted using an error function to determine their axial and lateral positions as follows [70]

$$I_k(x,y) = I_0\left(\mathrm{erf}\left(\frac{x-x_0+0.5}{\sqrt{2}\sigma_x}\right) - \mathrm{erf}\left(\frac{x-x_0-0.5}{\sqrt{2}\sigma_x}\right)\right) \times \left(\mathrm{erf}\left(\frac{y-y_0+0.5}{\sqrt{2}\sigma_y}\right) - \mathrm{erf}\left(\frac{y-y_0-0.5}{\sqrt{2}\sigma_y}\right)\right) + b_0, \quad \textbf{Eq. 3.1}$$

where $\mu_k(x,y)$ is the expected number of photons for a given pixel k, I_0 is the total number of photons and x_0 and y_0 are the emitter positions in lateral directions. σ_x and σ_y are the standard deviations of the error function in x and y, respectively, and b_0 is the background noise. By taking the error-propagation-weighted average of the fiducial markers' drifts, an appropriate

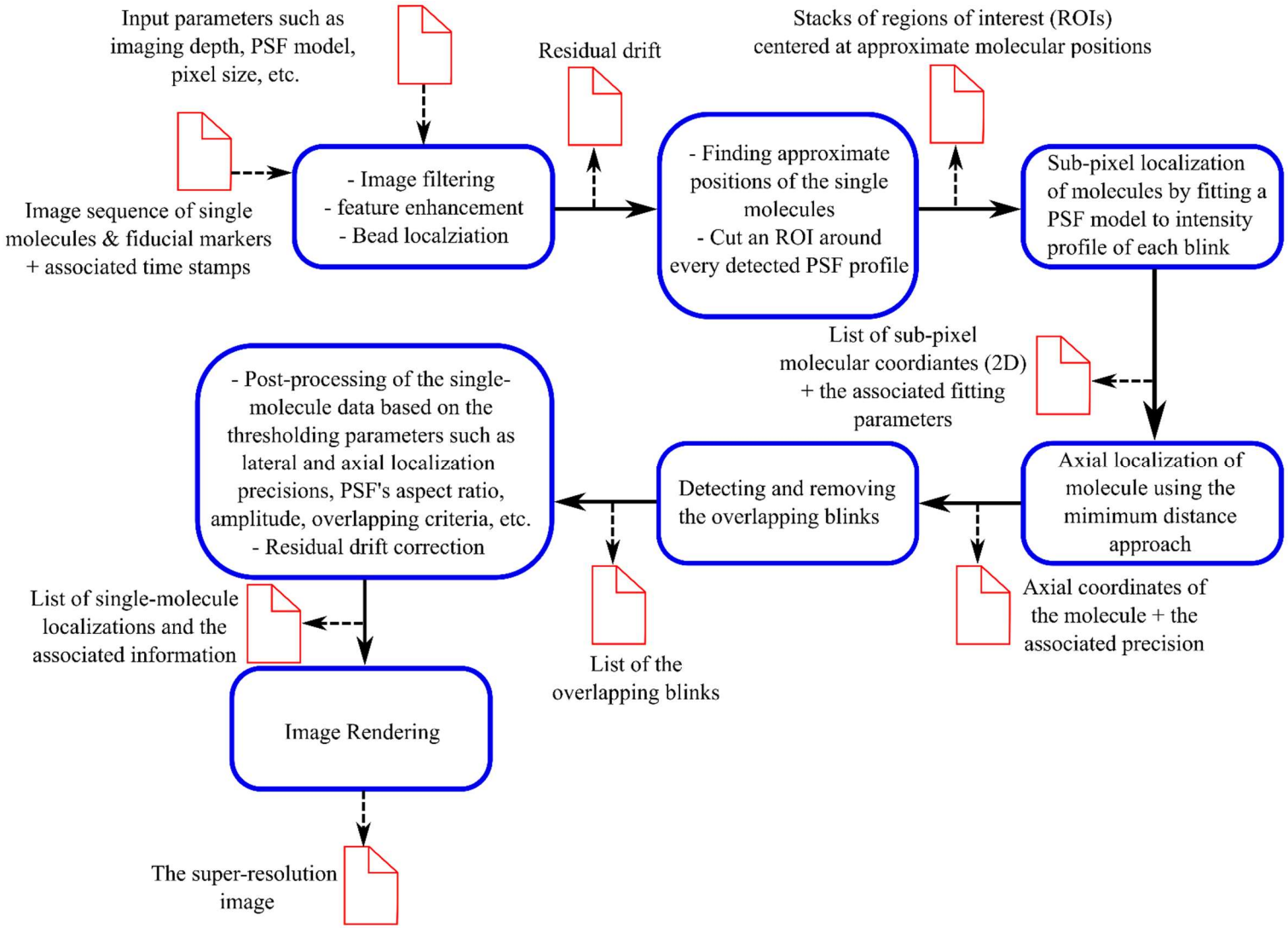

Figure 3.2 - Image processing pipeline for single molecule localization microscopy.

voltage was then sent to the piezo stage (Max311D, Thorlabs) using a 16-bit digital-to-analog converter (PCI6323, National Instruments, Austin, TX) and a piezo-stage controller (MDT693B, Thorlabs). The fiducial markers were exposed for ~200 ms, with an additional ~10 ms required for fitting the image and settling the piezo stage. Drift correction was therefore conducted at a rate of ~5 Hz. Measurements of 3D stability

The performance of the active stabilization system was measured by tracking the positional stability of 100 nm fluorescent beads on CCD1 for 10 minutes. A mixture of 100 nm TetraSpeck beads (T7279; Life Technologies) at a concentration of 1 in 200, and 100 nm Orange FluoSpheres (F8800; excitation 540nm, emission 560 nm, Life Technologies) at a concentration of 1 in 100000 were settled overnight onto a poly-L-lysine-coated coverslip. The coverslip was rinsed the following morning to remove beads that had not firmly attached, and then mounted in phosphate buffered saline. The 100 nm Orange FluoSpheres were tracked on CCD2 to provide drift correction feedback while the TetraSpeck beads were simultaneously imaged on CCD1.

3.1.3 Depth-Dependent Calibration

Calibration slides were prepared using 40 nm dark red FluoSpheres (F8789, Life Technologies) that were suspended in a mixture of 0.5% low melting point agarose and 30% sucrose dissolved in double distilled water. This mixture has a refractive index of ~1.38, which is close to that of cardiomyocytes [71]. The mixture was poured into a 1 mm deep chamber, sealed with a high precision coverslip (#1.5H, 22x22 mm, BioScience Tools, San Diego, CA) then rotated so as to maintain an even distribution of the beads until the gel had solidified.

A positional map of the beads in the gel was obtained by first scanning the gel along the Z axis to locate the depth of each bead (step size = 20 nm). Figure 3.3a shows an image of beads embedded in gel at an actual depth of 4 μm. The apparent depth of each bead is defined as the

depth where the bead appears as a homogeneous Gaussian (W_x/W_y = 1). Hell et al. [72] demonstrated that the actual position of the bead is linearly related to its apparent position (Z_{actual} = K*$Z_{apparent}$) up to a depth of ~50 microns, where K is the correction factor used to account for the refractive index mismatch between the objective's immersion oil (n_1) and the cell (n_2). Huang et al. [69] showed that K = 0.72 when n_1 = 1.515 and n_2 = 1.34, which increased to 0.89 when n_2 = 1.45. The refractive index of cardiomyocytes is ~1.38, and a linear interpolation gave the value of K = 0.78 used in our experiments. This value is close to the 0.79 previously used for whole-cell 3D SMLM [69].

Figure 3.3b shows the values of z vs the widths (Wx and Wy). To accumulate a sufficient number of data points, the sample was scanned laterally at fixed depths (for example, 4 □m in the case of Figure 3.3b). Figure 3.3c shows the calibration curve in the Wx-Wy plane. Once the 3D map of the beads was obtained, the depth-dependence of the calibration curve for any depth could be determined, as shown in Figure 3.3d. These curves can be then used for axial localizations of the blinks in the images. A modified version of the defocusing function was used to fit Wx and Wy as a function of Z as follows

$$W_{x,y}(z) = W_0\sqrt{1+\left(\frac{z-d}{f}\right)^2 + A\left(\frac{z-d}{f}\right)^3 + B\left(\frac{z-d}{f}\right)^4} + Cz \qquad \textbf{Eq. 3.2}$$

where $W_{x,y}(z)$ and W_0 are the FWHM at a given z and the FWHM at the focus, respectively, d is the offset of x and y focal planes from the average focal plane and f is the focal depth. A and B are coefficients to correct for any non-ideal behavior of the optics in the detection path and C is a coefficient to correct for any distortion induced by the refractive index mismatch when a calibration curve deeper than the coverslip is obtained.

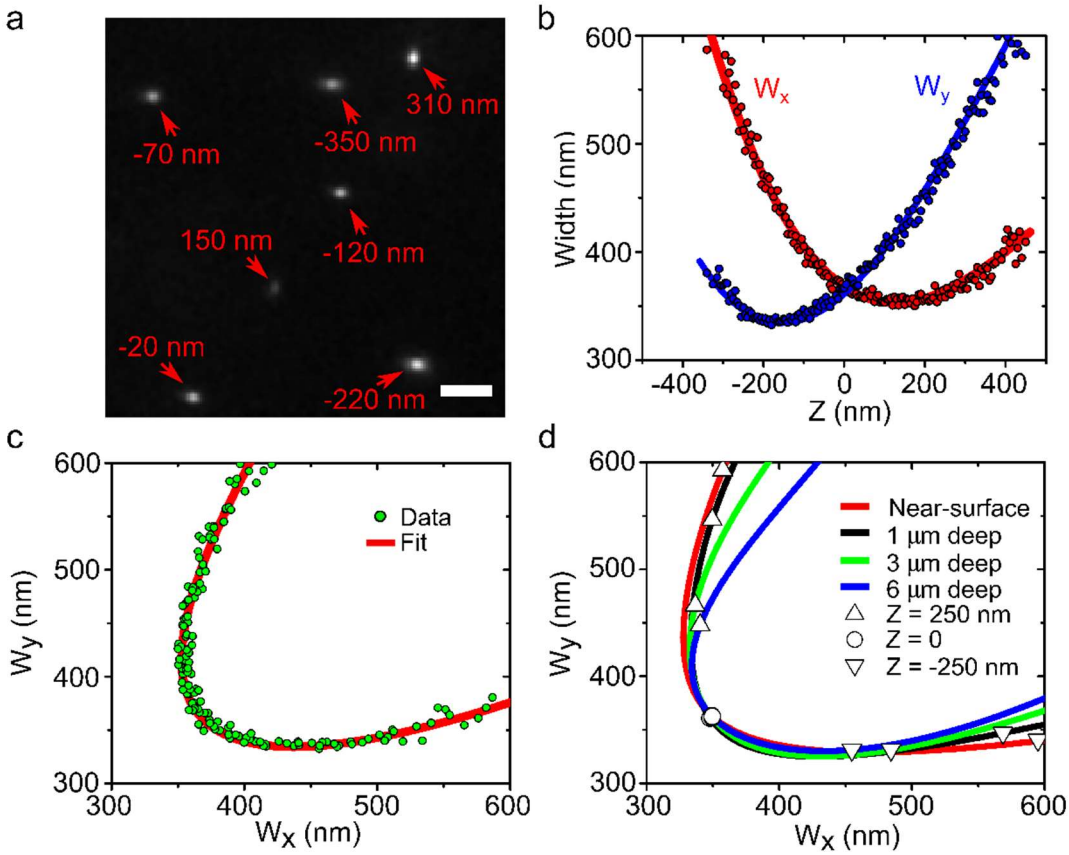

Figure 3.3 - Depth-dependent calibration curve. (a) An image of beads embedded in the gel at a depth of 4 µm. Z positions are shown relative to the focal plane. (b) The corresponding calibration curve for axial localizations at the depth of 4 µm, obtained by many lateral scans to accumulate sufficient number of beads at the same 4 µm depth. Each data point represents the average FWHM values obtained from 10 beads. (c) The same calibration curve as (b) but in the W_x-W_y plot. (d) Calibration curves at various depths. Upright triangles, circles and upside down triangles represent the depths of beads relative to the focal plane at z = -250 nm, z = 0 and z = 250 nm, respectively. Scale bar in (a): 2 µm.

3.1.4 Cell labeling and Preparation

The isolation of the cardiomyocytes and the labeling of the ryanodine receptor have been described in detail elsewhere [73]. Imaging was performed in a standard GLOX-thiol solution (a nitrogenated TN buffer [50 mM Tris, 10 mM NaCl, pH 8.0], 0.5 mg/ml glucose oxidase, 40 µg/ml catalase, 10 % (w/v) glucose and 10mM MEA). The coverslip with the attached cardiomyocytes was mounted onto a chamber with a volume of 700 µl which was filled with the imaging solution and sealed.

3.1.4.1 Ryanodine Receptors

These experiments used ventricular myocytes from adult rats. Animal handling was done in accordance with the guidelines of the Canadian Council on Animal Care and approved by the animal research committee of the University of British Columbia (UBC). All chemicals were purchased from Sigma-Aldrich (Oakville, ON) unless otherwise stated. We used male Wistar rats, 200 – 300 grams, (Charles River Laboratories, Wilmington, MA) that were given an intraperitoneal injection of 2 ml of 1000 units of heparin (Hepalean; Organon, Mississauga, ON) followed 30 minutes later with an intraperitoneal injection of 2 ml of sodium pentobarbital (240 mg/ml; MTC Pharmaceuticals, Cambridge, ON). The experiments proceeded only after hard pressure on the footpad failed to produce a withdrawal reflex.

The isolation technique is based on the method of Rodrigues and Severson [74]: The hearts were excised, hung on a Langendorff apparatus and perfused for 5 min. at 37°C with a nominally Ca^{2+}-free physiological saline solution, PSS, (in mmol/l): 138 NaCl, 5 KCl, 0.3 KH_2PO_4, 0.3 Na_2HPO_4, 10 HEPES, 15 D-glucose, 1 creatine, 1 carnitine, pH 7.4) that had been equilibrated with 95% O2/5% CO_2. Cell dissociation was initiated by switching to a perfusate of PSS containing 0.5 mg/ml Type II Collagenase (Worthington Biochemical, Lakewood, NJ) and 1 mg/ml bovine serum albumin. When the heart began to soften, the ventricles were cut free and

sliced into small chunks, which were gently shaken to dislodge cells. These were filtered through a 200 μm nylon mesh (Nitex) into fresh PSS. There were typically greater than 90% quiescent, rod-shaped, cells. Cells were immediately fixed in a solution containing 2% paraformaldehyde for 10 minutes at room temperature.

3.1.4.2 Labeling

Fixed cells were immediately quenched in 100 mM glycine for 10 min, washed in PBS (2 x 10 min), permeabilized with 0.1% Triton for 10 min after which they were washed in PBS (3 x 10 min). Prior to the application of the primary antibody, the cells were incubated for 30 minutes at room temperature (RT) with Image-IT FX Signal Enhancer (I36933; Life Technologies) to neutralize surface charge, washed briefly in PBS and then incubated for 1 hour at RT in BlockAid blocking solution (B10710; Life Technologies). The primary antibodies (anti-ryanodine receptor type 2, MA3-916; Cedarlane, Burlington, ON) was diluted in BlockAid before being applied to the cells (overnight at 4˚C). Cells were then washed in PBS (5 x 10 min) and incubated at RT for 90 minutes with goat anti-mouse Alexa 647 (A21236; Life Technologies) and washed in PBS (5 x 10 min) followed by post-fixation in 4% paraformaldehyde for 10 min and a final series of PBS washes (4 x 5 min).

3.2 Results and Discussion

3.2.1 Nanometer Real-Time 3D Stability

To eliminate drift for deep imaging, the system decouples the focal planes of the sample and the fiducial markers so that the imaging and tracking of the fiducial markers are independent of the depth at which the cell is imaged. As shown in Figure 3.1a, the sample is imaged on CCD1, while the fiducial markers are relayed to a separate camera (CCD2). When the sample imaging depth is changed, the position of the relay imaging lens (RL1) is adjusted to keep the fiducial markers in

focus on CCD2. A pair of concave and convex cylindrical lenses (CL1) allowed us to optimize the depth-dependent astigmatic effect for both surface and deep imaging.

The astigmatism introduced into the optical path of the fiducial markers (CL2, Figure 3.1a) allowed for their precise 3D localization, which was used to stabilize the sample position via a feedback loop. Figure 3.1b compares the positions of the fiducial markers imaged using CCD1 with and without feedback. Without feedback, the sample drifts were typically in the range of a few hundred nm over a period of 10 min. With the real-time 3D drift correction, the sample drift was limited to 0.7 nm (rms) in x and y and 2.5 nm (rms) in z (Figure 3.1b). As with single-molecule localization measurements [51], the stabilization accuracy may be limited by non-uniformity in the photo-response of a CCD camera, asymmetry in fluorescence emission of the beads as well as computational errors. Accuracy in z was worse than either x or y because the z position was derived from the ratio of width (W_x) to the height (W_y) of an elliptical PSF.

3.2.2 Axial Localization of Fluorophores in Deep Imaging

A common practice in obtaining a z-position calibration curve is to measure the PSF of a fluorescent bead (or fluorophores) on the cover slip while its z position is scanned (red curve in Figure 3.4a) [75-77]. However, this 'surface' calibration curve is incorrect for deeper imaging since the depth dependence of the PSF's ellipticity means that a given W_x/W_y ratio corresponds to different z localizations at different focal depths. Without proper correction the z positions can be off by hundreds of nanometers. Because the PSF is z-dependent, a correct z-axis localization curve cannot be obtained by scanning along the z-axis.

To obviate this problem, we present an approach to obtain the z dependence of the PSF using a combination of both lateral and axial scans. To minimize the refractive index mismatch, calibration slides were prepared using 40 nm dark red FluoSpheres (F8789, Life Technologies,

Burlington, ON) that were suspended in a mixture of 0.5% low melting point agarose and 30% sucrose dissolved in double distilled water. This mixture has a refractive index of ~1.38, which is close to that of cardiomyocytes [71]. As an example, Figure 3.4b shows an image of beads embedded in gel at a depth of 6 μm along with their positions relative to the focal plane. The actual depths of these beads, defined as the depth where the bead appears as a homogeneous Gaussian (the ratio of the width in x and y $W_x/W_y = 1$), were determined by the position of the piezo stage when stepping through z. The depth dependence of the PSF's ellipticity was obtained based on lateral scans, instead of axial scans, to accumulate PSFs of fluorescent beads at different depths. These positions were then multiplied by a correction factor of 0.78 to account for the refractive index mismatch between the embedding medium (gel) and the objective's immersion oil [72]. Once the 3D map of the beads was obtained, the depth-dependence of the calibration curve for any depth could be determined, as shown in Figure 3.4a. The insets in Figure 3.4a clearly demonstrate the astigmatic effect becomes less pronounced with depth, making it impossible to accurately position a blink when deep imaging is performed using the surface calibration curve. An advantage of this approach is that the effect of the refractive index mismatch is included in these calibration curves. In addition, the empirical measurement also includes the imperfection of the objective lens and other elements of the optical pathway [69]. These curves can then be used for axial localizations of the blinks in super-resolution images. Depending on the imaging depth, the correct calibration curve is used to find the axial position of each blink [69].

Figure 3.4c shows the histogram of blinks imaged at 6 μm deep in a W_y vs. W_x plot; there is a large discrepancy between the observed widths and the "surface" calibration curve (red line). On the other hand, the calibration curve at 6 μm depth (green line, Fig. 2c) obtained using the above methodology matches the distribution of the blink shapes in the W_y-W_x plot. Figure 3.4d and 2e

show reconstructed SMLM images of type 2 ryanodine receptors (RYR2) in a rat ventricular cardiomyocyte at a depth of 6 μm using the calibration curves obtained at the surface of the cover slip (Figure 3.4d) and at 6 μm deep (Figure 3.4e). The effect of using the incorrect calibration curve can clearly be seen in Figure 3.4d and its corresponding z distribution of blinks (Figure 3.4f). The range of z values is compressed to about half of their real values compared to those obtained when the correct calibration curve is used (Figure 3.4e and 2g).

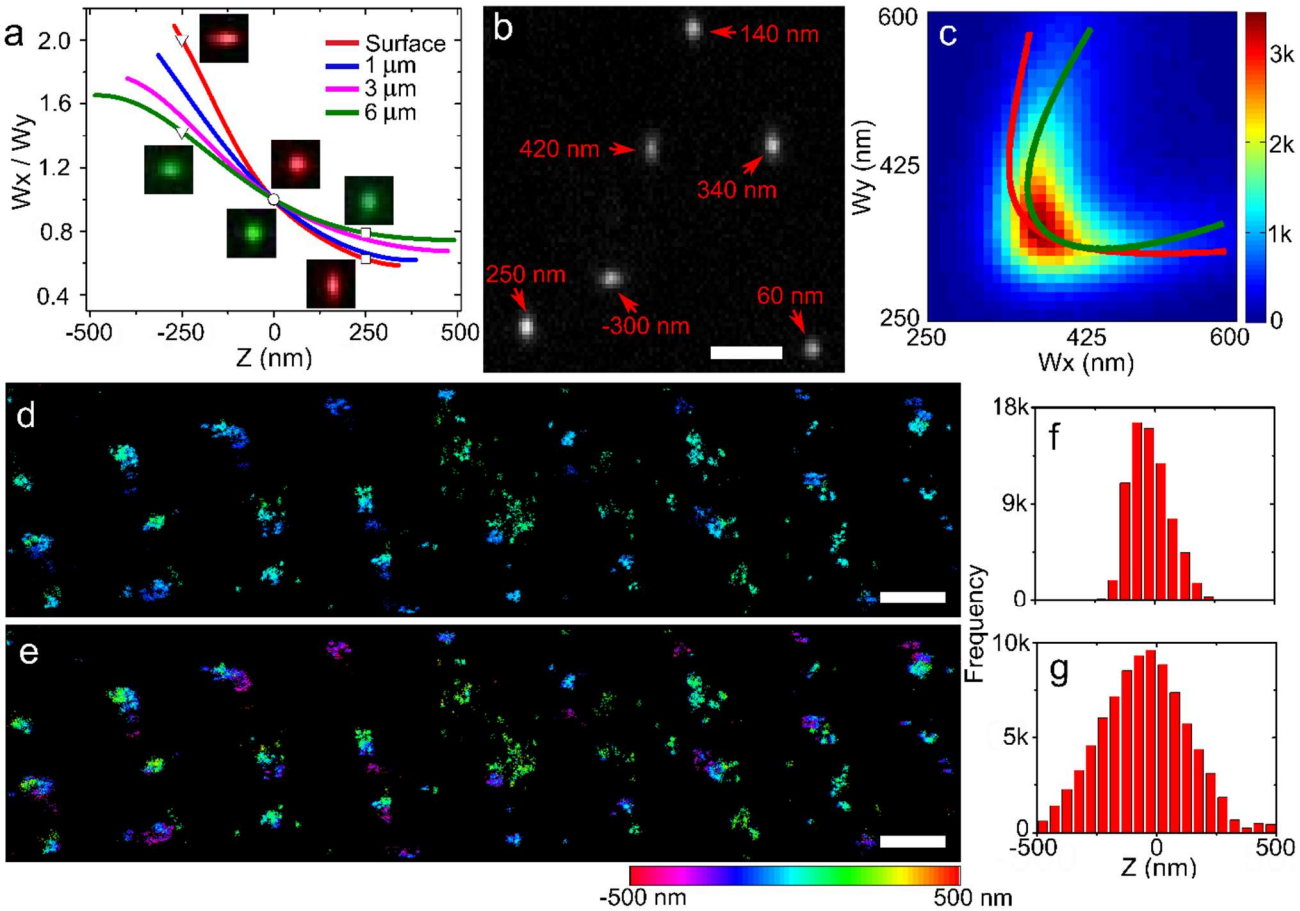

Figure 3.4 - Deep imaging and the depth-dependent calibration. (a) Aspect ratio of the PSF (*Wx/Wy*) as a function of z at various imaging depths. *Wx* and *Wy* represent widths of PSF in x and y directions, respectively. (b) An image of beads embedded in the gel at a depth of 6 µm. Their z positions, shown relative to the focal plane, were determined by a z-scan. (c) 2D histograms of the widths of PSFs of individual fluorophores in the *Wy*-*Wx* plot; red and green curves correspond to the calibration curve acquired at the surface and at 6 µm deep, respectively. (d-e) Super-resolution images of RyR2, color-coded according to depth, in the interior of a rat cardiomyocyte (imaging depth = 6 µm) using the calibration curves obtained at the surface (d) and at 6 µm (e). (f-g) The distributions of the z localizations of (d) and (e), respectively. Scale bar in (a): 2 µm, and scale bar in (d-e): 1 µm.

3.2.3 Time-Domain Filter for Blinks from Densely Packed Fluorophores

When astigmatism-based 3D localization is used to image structures with densely packed fluorophores, high local blinking rates may produce artefacts [78-82] even though the total blinks per frame appears to be low enough to produce what appears to be a well-defined image. Such local hot-spots occur when labeling RYR2. RYR2, a large 2.2 MDa protein, is a homotetrameric calcium channel located in discrete regions of the sarcoplasmic reticulum of the cardiac myocytes, a cell with a thickness of 10 μm or more. One primary antibody can bind to each of the RYR2 subunits (four/tetramer), and each secondary antibody (Alexa 647) contains about 6 fluorophores (A21236, Invitrogen; 6 moles dye/mole), so an individual tetramer can have many tens of fluorophores bound to an area about 30 nm square [83] and a RYR2 cluster could have hundreds of fluorophores located in an area comparable to the size of the PSF. In this small and densely packed structure, the probability of two adjacent fluorophores blinking at the same time becomes significant.

To overcome this issue, others have used spatial domain information to fit multiple Gaussians to overlapping blinks, but this is limited to 2D localization data [79, 80]. A more recent paper extends these methods to astigmatic (3D) data [78] and attempts to fit multiple 3D Gaussians to a blink when a single Gaussian fails. Our studies show that this latter method does not detect many overlapped blinks, that spatial domain information alone is insufficient, and that a time domain filter is essential to achieve an artefact free super-resolution image.

Figure 3.5a-c show three consecutive images of blinks from Alexa647-tagged RYR2s in a ventricular cardiomyocyte. While Figure 3.5a and 3.4c show well-fitted single blinks, Figure 3.5b

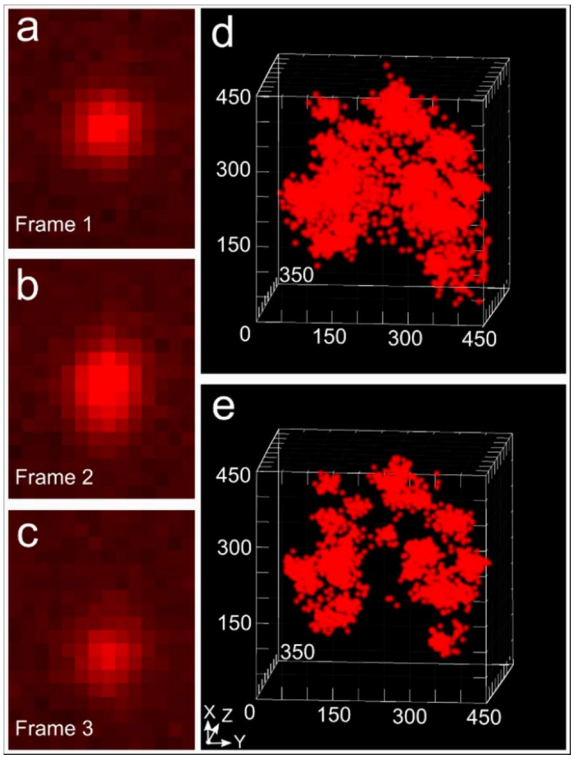

Figure 3.5 - Time-domain filter for blinks from densely packed fluorophores. (a-c) Three consecutive image frames showing blinks with an ambiguous interpretation. Frame b could be a blink originating in a different plane or the overlap of the blinks in a and c. (d-e) 3D view of RyR2 clusters before (d) and after (e) applying the time-domain filter removing the ambiguous blinks. Exposure time for each frame: 20 ms. Pixel size in (a-c): 100 nm and images are normalized to their maximum pixel value. Plots in (d-e) are binary; each red dot represents a blink of a fluorophore. x, y and z scales are in nm.

show that the blink lifetimes may have overlapped. In astigmatism-based 3D localizations, Figure 3.5b can be well-fitted with either a single molecule located 250 nm above the focal plane or an overlapped image of two molecules near the focal plane (Figure 3.5a and 3.4c), two solutions which cannot be distinguished from each other using only a spatial filter or goodness of fit criteria. To exclude these artefacts we developed an algorithm that monitored the coordinates of each blink over time. As noted above, overlapping blinks would be characterized by a sudden shift in the x, y or z coordinates in consecutive frames. Every blink within the size of the PSF that showed a variation in its position that exceeded three standard deviations of the localization error ($\sigma_x \sim 8$ nm, $\sigma_y \sim 8$ nm, $\sigma_z \sim 12$ nm) was excluded; in effect, a time domain filter. Figure 3.5d shows a RYR2 cluster in an area of 450 nm × 450 nm using only the spatial-fitting quality filter; the image shows that the cluster has little internal structure, although the area around the cluster is almost completely clear of blinks indicating that this lack of structure is not due to the non-specific binding of fluorophores. Figure 3.5e shows the same cluster after the application of the time-domain filter; it has revealed the positions of several individual RyR2 tetramers (~30 nm square) whose distribution appears consistent with recent electron tomographic analyses [84].

3.3 Conclusion

We have resolved issues associated with deep imaging of thick cells using 3D SMLM. Nanometer-scale system stability for deep imaging was achieved using two independent and variable focal planes. Localization errors due to the refractive index mismatch were removed by empirical measurements, which also provided corrections for the imperfection of the optics. Additionally, we showed that the spatial filter commonly used in reconstructing a super-resolution image may not eliminate artefacts that arise from structures with densely packed fluorophores. A time-domain filter was described that significantly reduced these artefacts.

Chapter 4: Real-Time 3D Stabilization of a Super-Resolution Imaging System Using an Electrically Tunable Lens

Single-molecule localization microscopy (SMLM) methods, such as photo-activated localization microscopy (PALM) [9], stochastic optical reconstruction microscopy (STORM) [10] and universal point accumulation for imaging in nanoscale topography (uPAINT) [11], use this prior knowledge to resolve the structures of biological systems with nanometer-scale spatial resolutions. SMLM is based on consecutive photoswitching of fluorophores (or fluorescent proteins) between the fluorescent state and the dark state such that only a subset of fluorophores is randomly activated at any time. This approach allows one to spatially and temporally separate the point-spread functions (PSFs) of activated fluorophores and estimate their lateral and axial positions using appropriate localization algorithms, even in a sub-diffraction region where hundreds of fluorophores are densely packed. The theoretical limit of resolution (i.e. localization precision) has been analytically determined, using Cramér-Rao bound (CRLB) and Fisher information matrix, to be dependent on the number of detected photons and the camera's pixel size and noise [41].

In practice, however, the achievable resolution in SMLM is closely related to both the localization precision and localization accuracy. The accuracy of single molecule localization is affected by emitter properties (isotropic or dipole emission), label displacement, biased localization algorithm and sample drift. SMLM is susceptible to sample drift caused by mechanical relaxation and temperature fluctuation because typically 10-20 min is needed to acquire tens of thousands of frames for reconstructing an informative super-resolution image. Thus, to achieve the expected resolution the sample drift has to be significantly smaller than the single molecule localization precision.

Several methods have been proposed to correct sample drift, including stabilization methods using fiducial markers as reference points [51, 52, 65], image correlation analysis of bright field images [53, 66] and post-processing of single-molecule localization data (i.e. blink tracking) [50, 54]. Due to the superior photon budgets of fluorescent particles, the microscope stabilization methods based on fiducial markers have shown the best performance. For instance, Lee *et al.* [52] achieved a nanometer-scale stability of an optical microscope in three dimensions by tracking a fluorescent bead attached to the coverslip. Pertsinidis *et al.* [51] have reported a sub-nanometer stability by actively tracking single molecules, instead of a fiducial marker, and correcting the drift through a feedback mechanism loop. They have successfully measured Cy3/Alexa 647 distance trace from a single DNA molecule with an accuracy of 0.77 nm. Despite this, practical issues exist when these sub-nanometer stabilization methods are applied to the deep imaging of thick biological samples. A sophisticated sample preparation procedure is required in Lee *et al.*'s method to add a fiducial marker to the same focal plane as the structure of interest. Pertsinidis *et al.*'s relies on localization of single molecules, which have short lifetimes and are more susceptible to photobleaching compared to fluorescent beads. Evidently, their approach is more suitable for short-term imaging experiments. Recently, it was shown that nanometer 3D stabilization for long-term deep imaging is possible with a bifocal design using a movable lens [85]. However, the depth of field was limited to several micrometers in that approach.

In this chapter, we present an optical design using an electrically tunable lens (ETL) to actively stabilize a single-molecule localization microscope down to a few nanometers in three dimensions. Generally, shifting the imaging focal plane in the microscopy systems is achieved by translating a lens in the optical path or by moving the sample itself. An alternative way for focus shifting is to use a liquid lens (focal length = f_{ETL}), which is tunable by applying an electrical current. Currently

available ETLs function based on various methods, including the shape changing approach [86] , dielectric effects [87], liquid crystals [88] or electrowetting principles [89]. The ETL can extend the depth of field of the objective lens to allow for the decoupling of focal planes of the two cameras; one camera possesses a focal plane placed at the region of interest inside a cell, while the other camera has its focal plane placed at the coverslip to image the fiducial markers. This approach enables high-accuracy drift-free super-resolution imaging of biological structures many micrometers deep within thick cells. Because this design has no moving parts in the optical path, better stability and user-friendliness can be obtained. This stabilization system is inexpensive, compact and easy to implement into both custom-built and commercial SMLM systems.

4.1 Materials and Methods

4.1.1 Optical Setup

A home-built SMLM system with an electrically tunable lens is shown in Figure 4.1. The optical system is an inverted microscope equipped with an apochromatic TIRF oil-immersion objective lens (60X; NA 1.49; Nikon Instruments, Melville, NY). A 639 nm laser (Genesis MX639, Coherent, Santa Clara, CA) was used for excitation of the Alexa 647 fluorophores (Life Technologies, Burlington, ON) and 100 nm Infrared FluoSpheres (F8799, Life Technologies). Activation of the Alexa 647 fluorophores (i.e. increasing the transition rate of fluorophores between dark and bright states) was provided by a 405 nm laser (LRD 0405, Laserglow Technologies, Toronto, Canada). Laser beams were collimated, combined, circularly polarized and focused onto the back aperture of the objective lens (L1 and L3; AC127-030-A, L2 and L4; AC127-075-A, DM1; FF560-FDi01, QWP; AQWP05M-600, L5; AC254-150-A, Thorlabs, Newton, NJ). Mirror M3 and M4 were moved by a translation stage (PT1, Thorlabs) to control incident beam angle and to switch between epi-illumination and oblique incident illumination

modes. A quad-band polychroic mirror (DM2; Di01-R205/488/532/636, Semrock, Rochester, NY) was used to reflect the laser beams and transmit the fluorescence signal. A 3D piezo stage (Max311D, Thorlabs) equipped with a 16-bit digital-to-analog converter (PCI6323, National Instruments, Austin, TX) and a piezo-stage controller (MDT693B, Thorlabs) was used to locate the region of interest and stabilize the microscope during data acquisition. A quad-notch filter (NF; 405/488/532/636, Semrock) was placed in the detection path to further block the excitation/activation lasers. A short-pass dichroic mirror (DM3; FF720-FDi01, Semrock) was used to separate the fluorescence emission of Alexa 647 from that of the fiducial markers.

The detection path of the Alexa 647 contained a weak cylindrical lens assembly (CL1; effective focal length (EFL) = 10 m) composed of a plano-convex and a plano-concave round cylindrical lens with anti-reflection coating and focal lengths of ±400 mm (LJ1363RM-B and LK1487RM-A, Thorlabs). CL1 introduced astigmatism into the imaging path, creating slightly different focal planes in the x and y directions. This resulted in elliptical PSFs for the fluorophores (i.e. the ellipticity and orientation of PSF varies along the optical axis). This allowed for the decoding of the axial positions of fluorophores within a few hundred nanometers above and below the focal plane of the objective lens [69]. Concave and convex cylindrical lenses were separated by a distance, d. After the cylindrical lens assembly, the emission light passed through a band-pass filter (BPF1; FF01-676/37, Semrock) followed by a 200 mm tube lens (TL1; ACA254-200-B, Thorlabs) and imaged to a back-illuminated electron multiplying charge-coupled device (EMCCD; iXon Ultra DU-897U, Andor, South Windsor, CT). A 2.5X zoom lens (ZL) was placed between DM3 and CL1 to obtain an overall magnification of 150 times.

In the detection path of the fiducial markers, the emission light passed through a 250 mm achromatic doublet lens (TL2; AC254-250-A, Thorlabs) followed by a relay imaging lens (RL1;

AC254-100-A, Thorlabs). An electrically tunable lens (EL-10-30-Ci-VIS-LD, Optotune) was placed after the relay system such that it is conjugate to the back focal plane of the objective lens. The emitted light then passed through a cylindrical lens assembly (CL2; EFL = 2 m), which has a design analogous to that of CL1; The focal lengths of the concave and convex components in CL2 are ±200 mm (LJ1653RM-B, LK1069RM-A, Thorlabs). The emission light then passed through a band-pass filter (BPF2; FF01-747/33, Semrock) and a 200 mm achromatic doublet lens (RL2; ACA254-200-B, Thorlabs) before being imaged by the CCD (Newton 970 UBV, Andor).

4.1.2 Sample Preparation for 3D Stabilization Test

To measure the performance of the active stabilization system, a mixture of 100 nm TetraSpeck beads (T7279; Life Technologies) at a concentration of 1 in 200, and 100 nm Infrared FluoSpheres (excitation 540nm; emission 560 nm) at a concentration of 1 in 200000 were affixed onto a poly-L-lysine-coated coverslip. The coverslip was then rinsed to remove beads that had not firmly attached and mounted in phosphate buffered saline. The 100 nm Infrared FluoSpheres were tracked on the CCD to provide drift correction feedback. TetraSpeck beads were simultaneously imaged on the EMCCD to measure the stability of the image on the camera.

4.1.3 Cell labeling and Preparation for STORM

Splenic B cells from 8-week old C57BL/6 mice were used. Animal handling was done in accordance with the guidelines of the Canadian Council on Animal Care and approved by the animal research committee of the University of British Columbia (UBC, Vancouver, Canada). Splenic B cells were isolated, as previously described in [90], using a B cell isolation kit (#19854, Stemcell Technologies) to deplete non-B cells. To increase TfR expression levels [91, 92], B cells were cultured in RPMI-1640 supplemented with 10% fetal calf serum, 2mM glutamine, 1mM pyruvate, 50 μM 2-mercaptoethanol, 50 U/mL penicillin and 50μg/mL streptomycin (complete

medium) and stimulated with 5 μg/ml E. coli 0111:B4 LPS (#L2630, Sigma-Aldrich catalogue) for 12 hr, as previously described in [90].

B cells were plated on coverslips (18 mm; #1.5H, Marienfeld,) functionalized with non-stimulatory M5/114 anti-MHCII monoclonal antibody (#12-5321, eBioscience) for 10 min at 4^0C, and subsequently fixed with ice cold 4% paraformaldehyde, 0.2% glutaraldehyde in PBS for 90 min. Fixed cells were washed in PBS (3×), permeabilized with 0.1% Triton for 5 min after which they were washed in PBS again (3×). The sample was blocked in blocking buffer (10% normal goat serum in PBS) for 1 hr at 4°C and subsequently stained with primary antibody (transferrin receptor; #13-6800, Invitrogen) overnight at 4°C. Cells were then washed in PBS (3×), incubated at room temperature for 30 min with goat anti-mouse Alexa Fluor 647 (A21244, Life Technologies) and then washed with PBS (5×) followed by a secondary fixation in 4% paraformaldehyde for 10 min and a final series of PBS washes (5×). Fluorescent fiducial markers (F8800, Life Technologies) were incubated with the sample overnight at $4\ ^{\circ}$C for the purpose of sample stabilization during image acquisition.

Imaging was performed in a standard GLOX-thiol solution (TN buffer [50 mM Tris, 10 mM NaCl, pH 8.0], 0.5 mg/ml glucose oxidase, 40 μg/ml catalase, 10% (w/v) glucose and 140 mM beta-mercaptoethanol). The coverslip along with the sample were mounted onto depression slides and sealed with the two-component silicone-glue Twinsil (Picodent, Wipperfürth,Germany, #13001000).

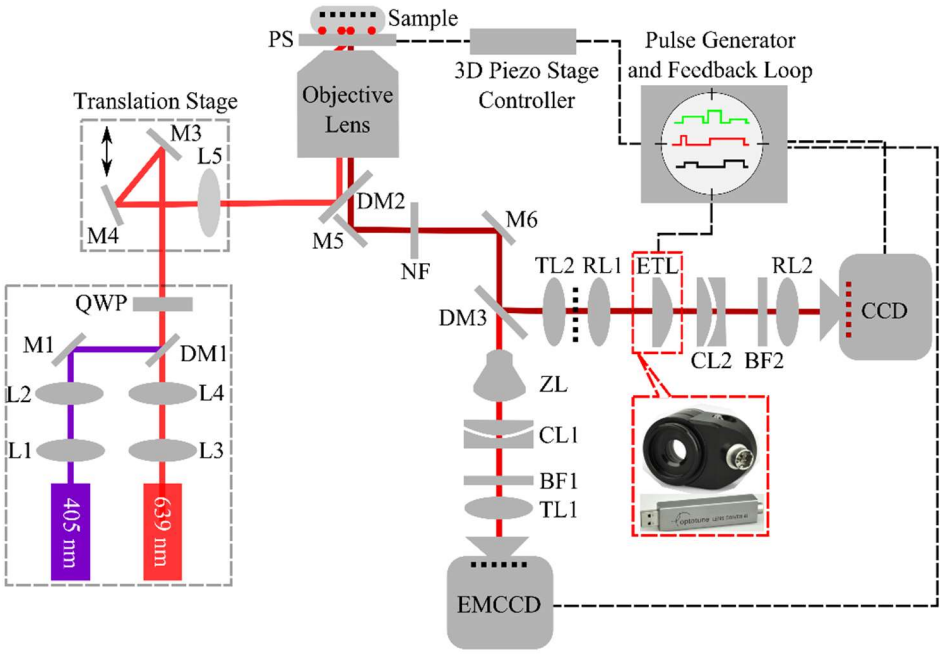

Figure 4.1 - Schematic layout of the imaging system. A 639 nm laser was used for excitation of fluorophores and fiducial markers and a 405 nm laser was used for reactivation. The diameters of the laser beams were adjusted using relay lenses (L1-L4). Lasers were combined using a dichroic mirror (DM1), circularly polarized by a quarter-wave plate (QWP), focused by a plano-convex lens (L5) and directed into the back aperture of the objective lens. Mirrors (M3 and M4) along with L5 were positioned on a translation stage to control incidence angle of the excitation light. A 3D piezo stage (PZ) equipped with a controller and a feedback mechanism loop was used. Fluorescence collected by the objective lens was separated by a dichroic mirror (DM2) and filtered using a notch filter (NF). The fluorescence signals from the cell and the fiducial markers were split using a dichroic mirror (DM3). In the bead tracking path, the fluorescence passed a relay system which consists of a tube lens (TL2) and a relay lens (RL1). An electrically tunable lens driven by an electrical lens driver (see the inset marked by the red box) was used to extend the depth of field of the objective lens and refocus the image of the fiducial marker on the CCD even when imaging many micrometers deep within a sample. A cylindrical lens assembly (CL2; composed of a plano-convex and a plano-concave round cylindrical lens) introduces astigmatism into the detection path enabling the 3D positions of the beads to be determined. These positions were used in a closed feedback loop for 3D stabilization of the microscope stage. A cylindrical lens assembly (CL1) and a tube lens (TL1) were used to form astigmatically aberrated images of the fluorophores onto the EMCCD. A 2.5X zoom lens (ZL) was used to obtain an appropriate magnification of 150X on the EMCCD. The black and red dashed lines indicate the focal planes of the structure of interest (focused on the EMCCD) and the fiducial markers (focused on the CCD) in the detection path, respectively. The fluorescent signal passes through band-pass filters (BPF1 and BPF2) before entering each camera.

4.2 Results and Discussion

4.2.1 The Dynamic Behavior of the Electrically Tunable Lens

The ETL used in this stabilization system functions based on the shape changing principle. It has low dispersion in the visible range (wavefront error < 0.25λ) and a focal length, f_{ETL}, spanning from 200 mm to 100 mm (10 mm aperture size; C-mounted). It consists of a polymer membrane surrounded with a low dispersion fluid on one side and air on the other side (Figure 4.2a). The curvature of the polymer membrane increases (i.e. f_{ETL} decreases) as the current applied to the ETL is increased; conversely, f_{ETL} decreases by lowering the current. The whole system is housed between two anti-reflection coated BK7 cover glasses [86, 93].

A programmable lens driver equipped with a temperature sensor and a drift compensation mechanism was used to control the ETL. When the imaging depth was changed, an appropriate current was applied to the ETL to tune f_{ETL} and keep the fiducial markers in focus on the CCD. In order to characterize the dynamic behavior of the ETL, 100 nm TetraSpeck beads attached to the coverslip were used. Starting with the beads in focus on the CCD (i.e. when the ellipticity of the beads' PSFs = 1), an appropriate voltage was applied to the piezo stage to move the sample in the z direction. The current was then increased gradually to bring the fluorescent beads back into focus on the CCD. Knowing the actual shift of the sample in z as well as the applied current, the relationship between the control current and the actual focal shift was obtained (Figure 4.2b). Displacement of the axial focal plane (δz) was measured to be ~11 μm when the control current was increased from 0 to 250 mA. Note that the ETL must be mounted horizontally to avoid the effect of gravity on its refractive power. Vertical mounting also induces a significant comatic aberration into the detection path. The ETL should be aligned precisely to ensure that the magnification of the detection path is independent of the f_{ETL}. Precise alignment was achieved

through an iterative process using a grid distortion test target (R1L3S3P, Thorlabs). f_{ETL} was changed to its maximum and minimum values and the grid images were recorded. The ETL was aligned such that the shift between the two images was insignificant. The response time of the ETL was measured to be less than 50 ms.

A cylindrical lens compound (CL2; focal length: f_{CL2}) was used to introduce an adjustable astigmatism into the imaging path of the fiducial markers. CL2 is composed of a plano-convex and a plano-concave round cylindrical lens with focal lengths (f_{cl}) of ±200 mm, separated from each other by a distance d (Figure 4.2c). The setup is simpler and more cost effective compared to previously proposed methods based on a deformable mirror array [94, 95]. In contrast to the single-cylindrical-lens design used by Huang *et al.* [69], our design allows for optimization of the depth-dependent astigmatic effect by varying the distance between the two cylindrical lenses. This approach allowed one to optimize the astigmatism for the PSF of the fluorescent beads for deep imaging. Therefore, one can achieve an axial localization precision down to a few nanometers when tracking beads to stabilize the microscope at any imaging depth that the depth of field allows. For instance, Figure 4.2d-e shows an optimized astigmatism effect used to track fluorescent beads when imaging at a depth of 8 μm (d = 10 mm). To achieve a good sensitivity, d was adjusted such that moving the beads along the z direction from +200 nm to -200 nm changes their aspect ratio on the CCD from 1.5 to 0.75.

In this design, the imaging focal shift in the z-axis δz is inversely proportional to the effective focal length of the ETL, $f_{ETL,eff}$, and is given by [96]

$$\delta z = -\frac{n f_{RL2}}{M^2 f_{ETL,eff}}, \qquad \textbf{Eq. 4.1}$$

where n is the refractive index of the immersion medium, f_{RL2} is the focal length of RL2 and M is the magnification on the CCD. $f_{ETL,eff}$ can be expressed as ${f_{ETL,eff}}^{-1} = {f_{ETL}}^{-1} + {f_{CL2}}^{-1} - d{f_{ETL}}^{-1}{f_{CL2}}^{-1} \approx {f_{ETL}}^{-1} + {f_{CL2}}^{-1}$. CL2 can be considered as an anamorphic Fourier transform system [97, 98] with a ray matrix in the x direction ($S_{CL2,x}$) given by

$$S_{CL2,x} = \begin{pmatrix} 1 & 0 \\ {f_{cl}}^{-1} & 1 \end{pmatrix} \begin{pmatrix} 1 & d \\ 0 & 1 \end{pmatrix} \begin{pmatrix} 1 & 0 \\ -{f_{cl}}^{-1} & 1 \end{pmatrix} = \begin{pmatrix} 1 - d{f_{cl}}^{-1} & 1 \\ -d{f_{cl}}^{-2} & 1 + d{f_{cl}}^{-1} \end{pmatrix}, \qquad \textbf{Eq. 4.2}$$

which gives $f_{CL2} = -d{f_{cl}}^{-2}$. The ray matrix for an individual cylindrical lens depends on a rotation matrix described by $R(\alpha) = \begin{pmatrix} \cos(\alpha) & \sin(\alpha) \\ -\sin(\alpha) & \cos(\alpha) \end{pmatrix}$, where α is the angle between the direction of the lens curvature and x-axis (in case of CL2, $\alpha = 0$ so $R(\alpha) = \mathrm{I}$).

For the current optical system, the imaging focal shift (δz) was calculated as 12.6 µm, which is very close to the experimental measurement (< 10% difference). The actual focal shift of ~11 µm (Figure 4.2b) was sufficient for imaging the transferrin receptors within B cells; the largest B cell which was observed had a thickness of ~10 µm. In addition, imaging at a depth larger than that greatly suffers from the sample-induced aberration and light scattering, which degrades the quality of the PSFs of single molecules. Note that δz can be easily extended by four times if one decreases M by two times (i.e. $M = 75$).

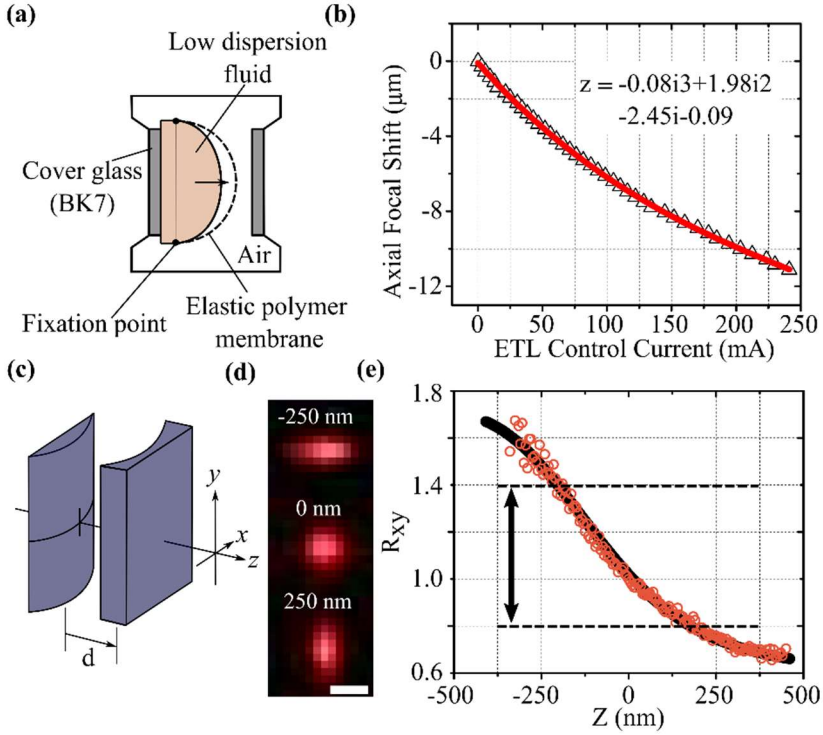

Figure 4.2 - Characteristics of the major optical elements used in the stabilization system. (a) Schematic representation of an electrically tunable lens based on shape-changing polymer membrane technology. (b) The axial focal shift vs. current for the ETL used in the stabilization system. (c) Schematic representation of the cylindrical lens compound, which introduces an adaptive astigmatic effect into the detection path of the fiducial markers. (d) *x-y* cross sections of an astigmatically aberrated PSF at different axial positions and (e) Aspect ratio (R_{xy}) of the astigmatic PSF as a function of *z.* The black arrow shows the range of ellipticity which was used for tracking of fiducial markers. This range provides sufficient sensitivity to achieve high accuracy tracking of fiducial markers in the axial direction.

4.2.2 Performance of the Active 3D Stabilization System

In order to examine the performance of the stabilization system, the positional stability of 100 nm TetraSpeck beads was measured on EMCCD for 10 min. Cameras were synchronized to obtain simultaneous exposure and readout. Both cameras were set to acquire images at a rate of ~3 frames per second (exposure time = 300 ms, piezo stage settling time = 20 ms). Five Infrared fiducial markers located close to the center of the frame were tracked on CCD to provide drift correction feedback. TetraSpeck beads were simultaneously imaged on EMCCD. A region of interest (ROI = 10 pixel × 10 pixel) was set around each individual bead and ROIs were subsequently fitted using an error function to determine the lateral position of the beads as follows

$$I_k(x,y) = I_0\left(\mathrm{erf}\left(\frac{x-x_0+0.5}{\sqrt{2}\sigma_x}\right) - \mathrm{erf}\left(\frac{x-x_0-0.5}{\sqrt{2}\sigma_x}\right)\right) \times \left(\mathrm{erf}\left(\frac{y-y_0+0.5}{\sqrt{2}\sigma_y}\right) - \mathrm{erf}\left(\frac{y-y_0-0.5}{\sqrt{2}\sigma_y}\right)\right) + b_0, \quad \textbf{Eq. 4.3}$$

where $I_k(x,y)$ is the expected number of photons for a given pixel k, I_0 is the total number of photons and x_0 and y_0 are the emitter positions in lateral directions. σ_x and σ_y are the standard deviations of the error function in x and y, respectively, and b_0 is the background noise. The aspect ratio, $R_{xy} = \sigma_x / \sigma_y$, was then calculated to determine the axial position of a bead according to the calibration curve shown in Figure 4.2e. Displacement of beads was subsequently determined by comparing their shifted and initial positions. The mean of the displacements was then calculated and an appropriate voltage was applied to the piezo stage through a feedback loop to correct for the drift in all axes.

Figure 4.3a shows the positional stability of the TetraSpeck beads on EMCCD with respect to time. Without the drift-correcting feedback loop enabled, the system drifts ~100 nm in the lateral direction and ~150 nm in the axial direction as measured over 10 min. With the feedback loop,

however, the sample was stabilized in real-time and in three dimensions down to a few nanometers; root-mean-square (rms) of the beads' position was measured to be ~0.7 nm in the x and y directions and ~2.7 nm in the z direction, as shown in Figure 4.3b. The uncertainty in bead localization may arise from the numbers of photons emitted by the fiducial markers, asymmetric emission profile of fluorescent beads, and non-linearity in the photoelectric response of the camera. Note that the uncertainty in z is about four times larger than that in x and y. This is partially due to error propagation, which occurs by estimating the axial position of a bead using the widths of its PSF in x and y directions, i.e. W_x and W_y.

4.2.3 Super-Resolution Imaging of Transferrin Receptors in B Cells

To demonstrate the impact of the real-time 3D stabilization system, transferrin receptors in B cells were imaged at a depth of 8 μm. The transferrin receptor (TfR) is a membrane glycoprotein and mediates cellular uptake of iron from a plasma glycoprotein, transferrin. Iron uptake from transferrin involves the binding of transferrin to the TfR, internalization of transferrin within an endocytic vesicle by receptor-mediated endocytosis and the subsequent release of iron from the protein induced by a decrease in endosomal pH [99]. In cell biology, TfR is a prototype marker for the recycling pathways and to probe both cell surface and endosomal structures in cells [100-102].

The 639 nm laser was used at a relatively low intensity (< 2 W/cm^2 at the sample) for illumination. A region of interest deep within the cell was located and the actual imaging depth was measured using the piezo stage controller. Before turning on the feedback mechanism loop, an appropriate current was applied to the ETL through the lens controller to obtain a clear image of the fiducial markers on the CCD. The current was adjusted such that the beads' ellipticity was in the range of 0.75-1.5. Up to five fiducial markers were typically tracked during image

acquisition at a rate of 3 frames per seconds (fps). Exposure time and gain of the CCD were gradually increased to compensate for the continuously decreasing number of photons emitted by fiducial markers. The intensity of the 639 nm laser was then increased to ~5 kW/cm^2 and the sample was photobleached for ~30 s. 40,000 frames were typically acquired on the EMCCD, at a rate of ~50 fps, to accumulate a sufficient number of single-molecule localizations. To reactivate dye molecules and compensate for a decreasing number of blinks due to photobleaching, the intensity of the 405 nm laser was increased in a stepwise fashion (from 0 to ~1 W/cm^2) during image acquisition. The post-acquisition processing of images to determine the positions of single-molecules was performed using a software written in MATLAB, as previously described in [85].

A drift-free super-resolution image of transferrin receptors in a B cell is shown in Figure 4.4a. This image was constructed by plotting the density map of single-molecule localizations (nearest neighborhood distance (NND) = 100 nm). The corresponding image with drift is shown in (Figure 4.4b). This was obtained by computationally adding the actual drift in all directions that occurred during image acquisition to the drift-free image (Figure 4.4c). Insets of the regions marked by white boxes in Figure 4.4a-b are shown in Figure 4.4d and 4e, respectively. The drift-free super-resolution image (Figure 4.4d) reveals that transferrin receptors are distributed as well-defined clusters, which are punctate with a significantly higher density compared to the corresponding clusters in the drifted image (Figure 4.4e). Specifically, clusters in the drifted image are elongated and blurred. The three-dimensional representations of the green-boxed regions in Figure 4.4d and 4e are shown in Figure 4.4f and 4g, respectively. The clusters in the drift-free super-resolution image (Figure 4.4f) are isotropic and distinct from cluster to cluster. However, the corresponding clusters in the drifted image (Figure 4.4g) are non-isotropic and difficult to discern as they are fused together.

To quantitatively analyze the effects of drift on topology and density of TfR clusters, a cluster analysis method based on Voronoï tessellation was used [103, 104]. Voronoï tessellation is based on the principle of subdividing an image into polygonal regions centered on seeds. Any point within a polygon is closer to its associated seed than it is to any other seed. Figure 4.4h-i show the tessellation maps of the regions marked by red boxes in Figure 4.4d-e; segmented clusters are shown in blue. Segmentation of the localization data points into clusters was performed using a single parameter, i.e. density threshold, which was set to twice the average localization density (similar to the work by Levet *et al.* [103]). Comparing the regions marked by white dashed lines in Figure 4.4h-i, one can see that drift not only affects the separation of the closely spaced transferrin clusters (region A and B) but it also affects the topology of the clusters (compare the clusters in region C of Figure 4.4h with the corresponding clusters in Figure 4.4i).

A more comprehensive analysis of transferrin clusters (Figure 4.4j-k) reveals that drift has significant influences on the distribution of cluster density (i.e. number of localization per cluster per unit area, and cluster size). Overall, the TfR clusters in the drift-free image are smaller than those in the drifted image and show higher cluster density. This is attributed to the sample drift, which extends the area of clusters and leads to a lowered cluster density. The drift-free images show that that TfR exist as heterogeneous nanoclusters in B cells (as shown by bimodal size distribution in Figure 4.4k). This data is consistent with electron microscopy (EM) studies, which show that size of TfR containing vesicles varies from 30 nm to 160 nm [101, 105-107]. The distribution of the cluster circularity (Figure 4.4l) shows that the transferrin clusters in the drift-free super-resolution image are more circular compared to those in the drifted image. Cluster circularity was calculated as the ratio of the major and minor axes of a cluster. The majority of TfR clusters in the drifted image have a circularity of 0.5, compared to 0.75 in the drift-free image.

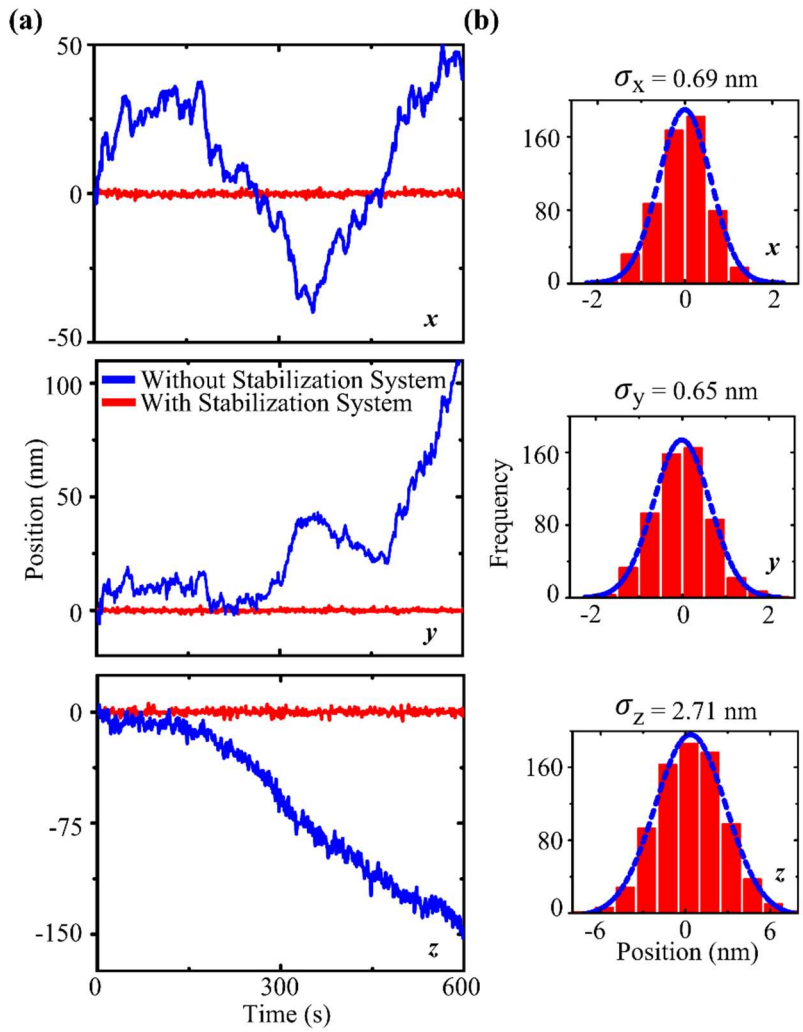

Figure 4.3 - Performance of the active 3D stabilization system using an electrical tunable lens system. (a) The positions of the fluorescent beads in *x*, *y* and z over 10 min with the stabilization system (red curves) and without the stabilization system (blue curves). (b) Histogram of bead tracking accuracy in each direction. Standard deviations were 0.69 nm in *x*, 0.65 nm in *y* and 2.71 nm in *z*. Four fiducial markers on the CCD were used for stabilizing the setup. The data shown here were obtained by analyzing the stability of three TetraSpeck beads on the EMCCD.

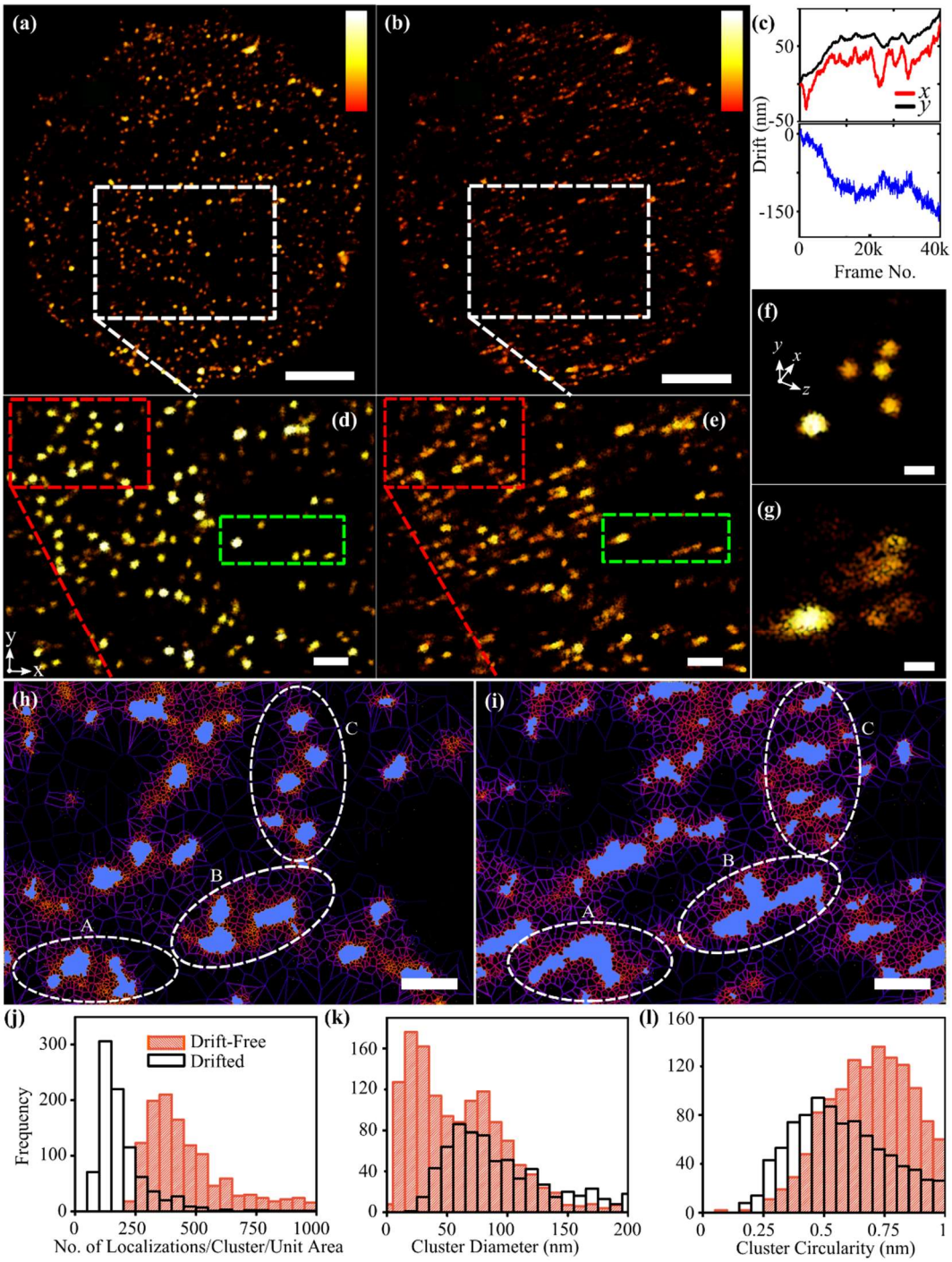

Figure 4.4 - The organization of transferrin receptors in a drift-free super-resolution image vs. a corresponding drifted image. STORM images of transferrin receptors in a B cell obtained (a) with the stabilization system and (b) without the stabilization system. (c) The actual drift occurred during STORM data acquisition. (d-e) Insets of the regions marked by white boxes in (a-b). (f-g) Three-dimensional representations of the regions marked by green rectangles in (d-e). (h-i) Voronoï tessellation maps of the red-boxed regions in (d-e); regions in blue show the transferrin clusters segmented using density thresholding. (i-h) Quantitative analysis of transferrin clusters in the drift-free image and the drifted image. Distribution of the cluster density (j), cluster diameter (k) and cluster circularity (l). Scale bars in (a-b): 2 µm, (d-e): 500 nm and (f-i): 200 nm.

4.3 Conclusion

We presented an optical design for real-time 3D drift correction of a super-resolution microscope using an electrically tunable lens. By extending the depth of field of the objective lens and decoupling the focal planes of the sample and the fiducial markers, it enabled drift-free super-resolution imaging at any depth. The instability of the microscope stage was shown to be reduced to ~0.7 nm in the lateral direction and ~2.7 nm in the axial direction.

The impact of stability on super-resolution images was demonstrated by imaging transferrin receptors in B cells at a depth of 8 μm. The drift-free super-resolution image depicts the transferrin receptors as distinct and heterogeneous clusters with a high circularity index and a bimodal size distribution. Additionally, the average density of fluorophores per unit area in these clusters was two times higher than that in the drifted image.

This stabilization system is simple, inexpensive and compact and can be readily integrated into both commercial and custom-made super-resolution imaging systems. Imaging experiments, which require long-term data acquisition are generally susceptible to setup instability, but this can be greatly ameliorated by the technique presented in this study.

Chapter 5: The Structure of the Couplon in Rat Ventricular Myocytes

The excitation-contraction coupling (ECC) process in ventricular muscle cells (myocytes) is initiated by an influx of Ca^{2+} through voltage-gated Ca^{2+} channels ($Ca_v1.2$) on the sarcolemma. The sarcolemmal membranes of the mammalian ventricular myocytes are characterized by the presence of invaginations called transverse tubules (T-tubule). T-tubules are key determinants of cardiac cell function and are a network of transverse and axial elements (i.e. the transverse-axial tubule system (TATS)). A significant number of proteins involved in the ECC process are concentrated within the T-tubular network, including the L-type voltage-gated Ca^{2+} channels ($Ca_v1.2$) and the Na^+/Ca^{2+} exchangers (NCX), or in the membrane of the adjacent junctional sarcoplasmic reticulum (the type-2 ryanodine receptors (RyR2)) [108].

During the stimulation of myocytes, action potentials travel along the T-tubules, where it activates the L-type voltage-gated Ca^{2+} channel ($Ca_v1.2$), resulting in an influx of Ca^{2+} through $Ca_v1.2$ on the plasmalemma. The L-type calcium channels are in a close association with the type-2 ryanodine receptors (RyR2) in the sarcoplasmic reticulum (SR)and form a functional element called a couplon. A small influx of Ca^{2+} from $Ca_v1.2$ can therefore activate the associated RyR2s, leading to a much larger release of Ca^{2+} into the contractile part of the cell (myoplasm). This mechanism of ECC is called calcium-induced calcium release [109, 110]. On the other hand, the extrusion of Ca^{2+} from myocardial cells is accomplished through the Na^+/Ca^{2+} exchangers (NCX). NCX is essentially a secondary active transporter, which translocates three Na^+ ions in exchange for one Ca^{2+} ion. The ion exchange is reversible and the transportation direction is determined by the local gradients of Na^+ and Ca^{2+} as well as the membrane potential [110].

In principle, the morphological details and distribution of the membrane system are crucial for controlling cardiac Ca^{2+} dynamics. Mapping the three-dimensional topology of this membrane

system can provide valuable information for elucidating the underlying mechanisms of cardiac Ca^{2+} dynamics. Recently, Asghari *et al. [111, 112]* showed that RyR2s are located only in three regions: in couplons on the surface, in transverse tubules, and on most regions of the axial tubules. They also showed that the RyR2s may play a significant role in the ECC since the majority of RyR2s colocalize with the $Ca_v1.2$s. In addition, Thior *et al*. [113] have used electron tomography to map the three-dimensional structure of dyadic clefts and associated membrane organelles in mouse ventricular myocardium. Comparable results with numerous smaller and irregularly shaped clusters of RyR2 have been also shown by super-resolution imaging of rat ventricle myocardium [114]. However, the super-resolution co-localization and distribution of type-2 ryanodine receptor (RyR2), the L-type voltage-gated Ca^{2+} channel ($Ca_v1.2$) and the Na^+/Ca^{2+} exchanger (NCX) has not been characterized. Thus, we have used dSTORM to examine the distribution and colocalization of the type-2 ryanodine receptor (RyR2) and the L-type voltage-gated Ca^{2+} channel (Cav1.2) on the surface and in the interior of rat ventricular myocytes.

5.1 Materials and Methods

5.1.1 Optical Setup

A custom-built STORM system, as previously described in Chapter 3, was modified to allow for two-color SMLM experiments (Figure 5.2). The fluorescent signals from Alexa 647 fluorophores (red) and Cy3B fluorophores (green) were split using a dichroic mirror (DM5; FF560-FDi01, Semrock). In the detection path of Cy3B fluorophores, a tube lens (TL3; ACA254-200-B,

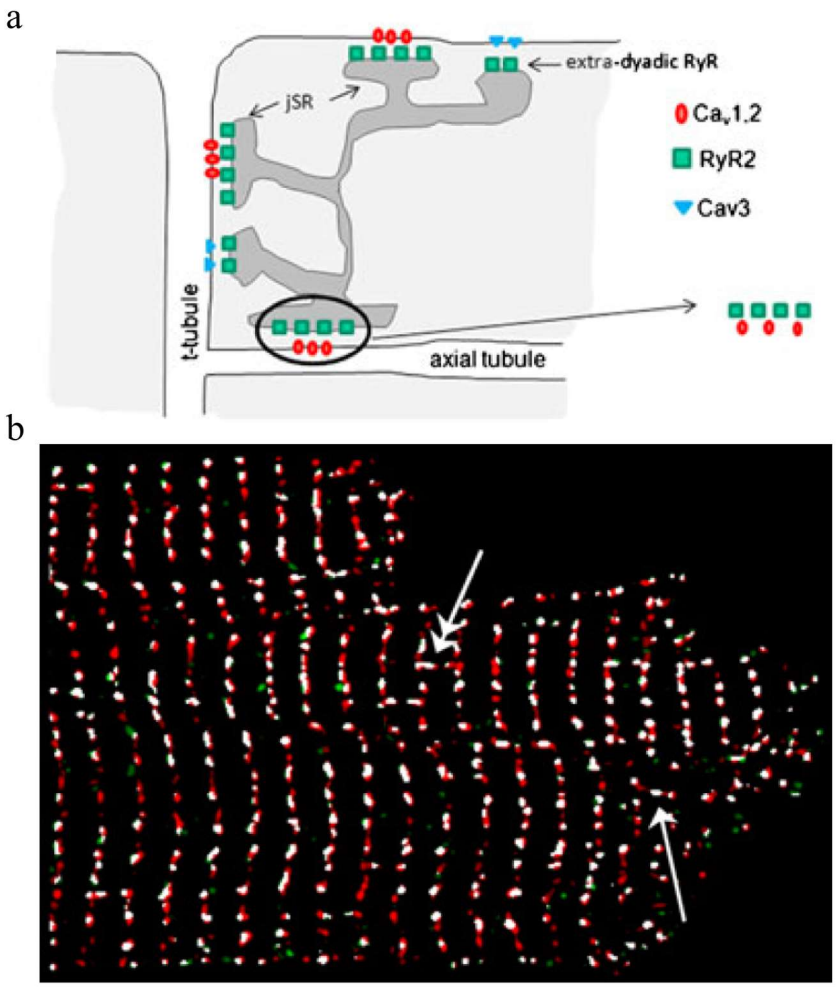

Figure 5.1 – Ultrastructure of a cardimyocyte. (a) Hypothesized structure of an adult ventricular myocyte. Couplons are visible on the cell surface and on both transverse and axial tubules. All couplons contain RyR2, which are opposite to $Ca_v1.2$ in the larger couplons and Ca_v3 in the smaller couplons [111]. (b) A diffraction-limited fluorescence microscopy image of a rat ventricular myocyte labelled for RyR2 (red) and $Ca_v1.2$ (green). The overlap is shown in white. Couplons traversing an entire sarcomere (arrow) and part of a sarcomere (double arrow) are indicated [115]. Scale bar: 2 μm.

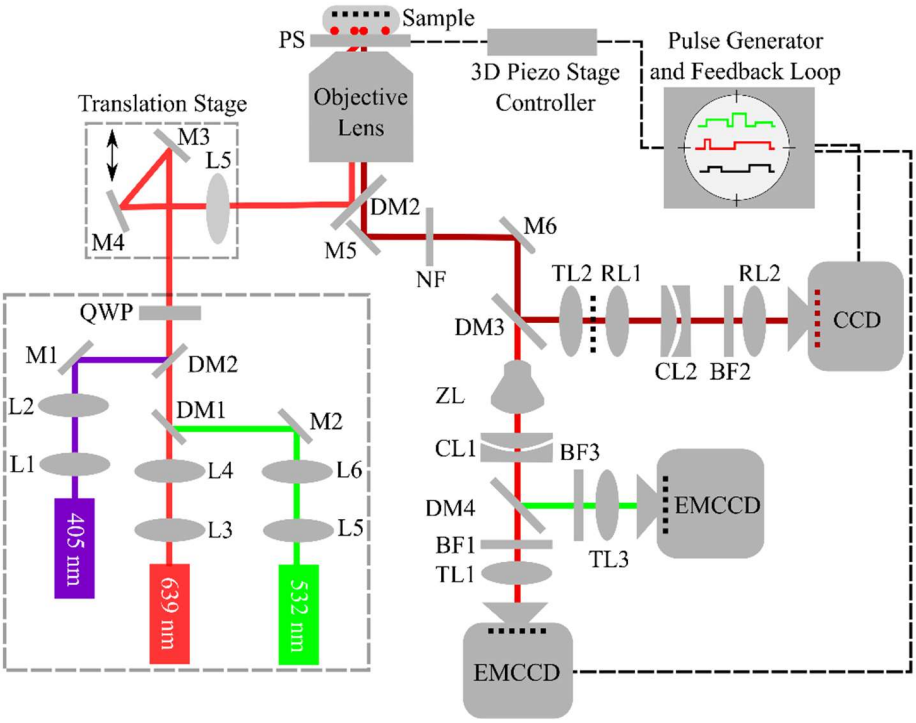

Figure 5.2 - Schematic layout of the two-color single-molecule localization microscope. A 639 nm laser was used for the excitation of Alexa 647 fluorophores and the fiducial markers. Cy3B fluorophores were excited using a 532 nm laser. A 405 nm laser was used for reactivation. The diameters of the laser beams were adjusted using relay lenses (L1-L6). Lasers were combined using the dichroic mirrors (DM1 and DM2), circularly polarized by a quarter-wave plate (QWP), focused by a plano-convex lens (L5) and directed into the back aperture of the objective lens. Mirrors (M3 and M4) along with L5 were positioned on a translation stage to control the incidence angle of the excitation light. A 3D piezo stage (PZ) equipped with a controller and a feedback mechanism loop was used. Fluorescence collected by the objective lens was separated by a dichroic mirror (DM3) and filtered using a notch filter (NF). The fluorescence signals from the cell and the fiducial markers were split using a dichroic mirror (DM4). In the bead tracking path, the fluorescence passed a relay system which consists of a tube lens (TL2) and a relay lens (RL1). A cylindrical lens assembly (CL2; composed of a plano-convex and a plano-concave round cylindrical lens) introduced astigmatism into the detection path enabling the 3D positions of the beads to be determined. These positions were used in a closed feedback loop for 3D stabilization of the microscope stage. A cylindrical lens assembly (CL1) and the tube lenses (TL1 and TL3) were used to form astigmatically aberrated images of the fluorophores onto the EMCCD1 and EMCCD2. The fluorescence signals from Alexa 647 fluorophores (red) and Cy3B fluorophores (green) were split using a dichroic mirror (DM5). A 2.5X zoom lens (ZL) was used to obtain an appropriate magnification of 150X on the EMCCDs. The black and red dashed lines indicate the focal planes of the structure of interest (focused on the EMCCD) and the fiducial markers (focused on the CCD) in the detection path, respectively. The fluorescent signal passes through band-pass filters (BPF1-3) before entering each camera.

Thorlabs) was used to focus the emitted light on EMCCD2 (iXon Ultra 897 BV, Andor). In order to accurately match the focal planes of the two cameras, TL3 was mounted in a zoom housing (SM1NR1; Thorlabs) capable of non-rotating translation of the lens along the optical axis. The signal was filtered using a band-pass filter (BF3; FF01-562/40, Semrock).

5.1.2 Image Registration with Nanometer Resolution in Dual Color SMLM

The proximity of two entities in fluorescence microscopy is typically investigated by the colocalization between two fluorescent probes. The colocalization of two different molecules involves not only the single-channel localization errors, $\sigma_{loc,1}$ and $\sigma_{loc,2}$, but also the registration precision, σ_{reg}, with which the two channels are mapped to each other. This gives a relative distance uncertainty of $\sigma = ({\sigma_{loc,1}}^2 + {\sigma_{loc,2}}^2 + {\sigma_{reg}}^2)^{1/2}$. Geometric transformations, such as translational, rotational and scaling transformations are usually sufficient for diffraction-limited applications to align one channel with another. Super-resolution imaging, however, demands a more rigorous method for image registration to achieve the desired precision and accuracy (i.e. a registration precision of a similar order to that of single channel localization precision is typically required) [51, 116]. In this section, the methodology that we used for image registration in dual-color SMLM is described.

To accumulate a sufficient number of control points across the field of view (FOV = 50 x 50 μm^2), a microscope slide with isolated TetraSpeck fluorescent beads was used (100 nm beads, stained with four different fluorescent dyes; blue (365/430), green (505/515), orange (560/580) and red (660/680)). The sample was illuminated with both green and red lasers and the EMCCD cameras were synchronized. The sample was scanned in a grid pattern using a 3D piezo stage (grid spacing in x and y = 10 μm) and the images were subsequently acquired. The lateral positions of beads were then determined by fitting an error function to the PSF (as previously described in

Chapter 3). The coordinates of the control points in the two channels were matched using a pattern recognition algorithm and a set of control points (i.e. $(x_{i,R}, y_{i,R})$ and $(x_{i,G}, y_{i,G})$) were obtained [117, 118], which were used to find a local weighted mean (LWM) mapping function (Figure 5.3a). This mapping function was then used to register the two channels, i.e. transform the coordinates of the green channel to that of the red channel (Figure 5.3b-d).

The error associated with the mapping function was calculated using the target registration error (TRE) method [119]. TRE is based on sequentially excluding a pair of control points (e.g. pair *i*) and calculating an LWM mapping function ($f_{i,LWM}$) using the remaining control points. By applying this mapping function to the pair that was left out, the Euclidean distance between the registered points was calculated as the registration error (Figure 5.3e). The TRE was then determined as follows

$$TRE = \left(\frac{1}{N}\sum_{i=1}^{N}\left(\left[x_{i,R} - f_{i,LWM}\{x_{i,G}\}\right]^2 + \left[y_{i,R} - f_{i,LWM}\{y_{i,G}\}\right]^2\right)\right). \qquad \textbf{Eq. 5.1}$$

A TRE of ~ 10 nm was obtained for image registration in our setup. A custom-written software in MATLAB was used for image registration and associated calculations. Note that the registration in the *z* direction was done using a single offset value, which was measured experimentally such that the two cameras possessed the same focal planes.

5.1.3 Cell Labeling and Preparation

Enzymatically dissociated cells were permeabilized with 0.1% Triton X-100 for 10 minutesthen plated on poly-L-lysine (P1274; Sigma-Aldrich, Oakville, ON) coated coverslips. Prior to primary antibody labelling, the cells were incubated for 30 min at room temperature (RT) with Image-IT FX Signal Enhancer (I36933; Life Technologies, thermofisher.com) to neutralize surface charge and then washed briefly in PBS and incubated for 1 hr at RT in BlockAid blocking solution

(B10710; Life Technologies). Primary antibodies used in these experiments were one or more of the following: a) monoclonal anti-ryanodine receptor type 2 (RyR2; MA3-916, Cedarlane, Burlington, ON), b) polyclonal anti-L-type Calcium channel ($Ca_v1.2$; AGP-001, Alomone Labs, Jerusalem, Israel), and c) monoclonal anti-Sodium-Calcium exchanger (NCX; R3F1, Swant, Marly, Switzerland) all at a concentration of 1:100 diluted in BlockAid. In dual labelling experiments, the anti-RyR2 and anti-$Ca_v1.2$ were added simultaneously. Cells were incubated at 4^0C overnight with the primary antibodies. The following day, the sample was then washed in PBS (5 x 10 min) and incubated with the secondary antibodies at RT for 90 min. The secondary antibodies included anti-mouse, anti-rabbit, and anti-guinea pig antibodies conjugated to a Cy3B fluorophore (GE Healthcare, Mississauga, ON) per the manufacturer's instructions. The degree of conjugation was measured and found to be 6-7 fluorophores/antibody for each.

Single label experiments examining RyR2 or NCX used goat anti-mouse Alexa 647 (A21236; Life Technologies) as the secondary, while those examining $Ca_v1.2$ used goat anti-guinea pig Alexa 647 (A21450; Life Technologies). Dual labelled experiments examining the mapping of RyR to RyR between the two cameras used goat anti-mouse Cy3B and goat anti-mouse Alexa 647 as their secondaries, while colocalization experiments with RyR2 and Cav1.2 were incubated with goat anti-mouse Cy3B (for RyR2) and goat anti-guinea pig Alexa 647 (for Cav1.2), Life Technologies). After incubation, cells were washed in PBS (5 x 10 min) followed by post-fixation in 4% paraformaldehyde for 10 min and a final series of PBS washes (4 x 5 min).

STORM imaging was performed in an imaging solution (a nitrogenated TN buffer [50 mM Tris, 10 mM NaCl, pH 8.0], 0.5 mg/ml glucose oxidase, 40 µg/ml catalase, 10 % (w/v) glucose and 10mM MEA). The coverslip containing the cells was mounted onto a chamber with a volume of 700 µl, which was filled with the imaging solution and sealed.

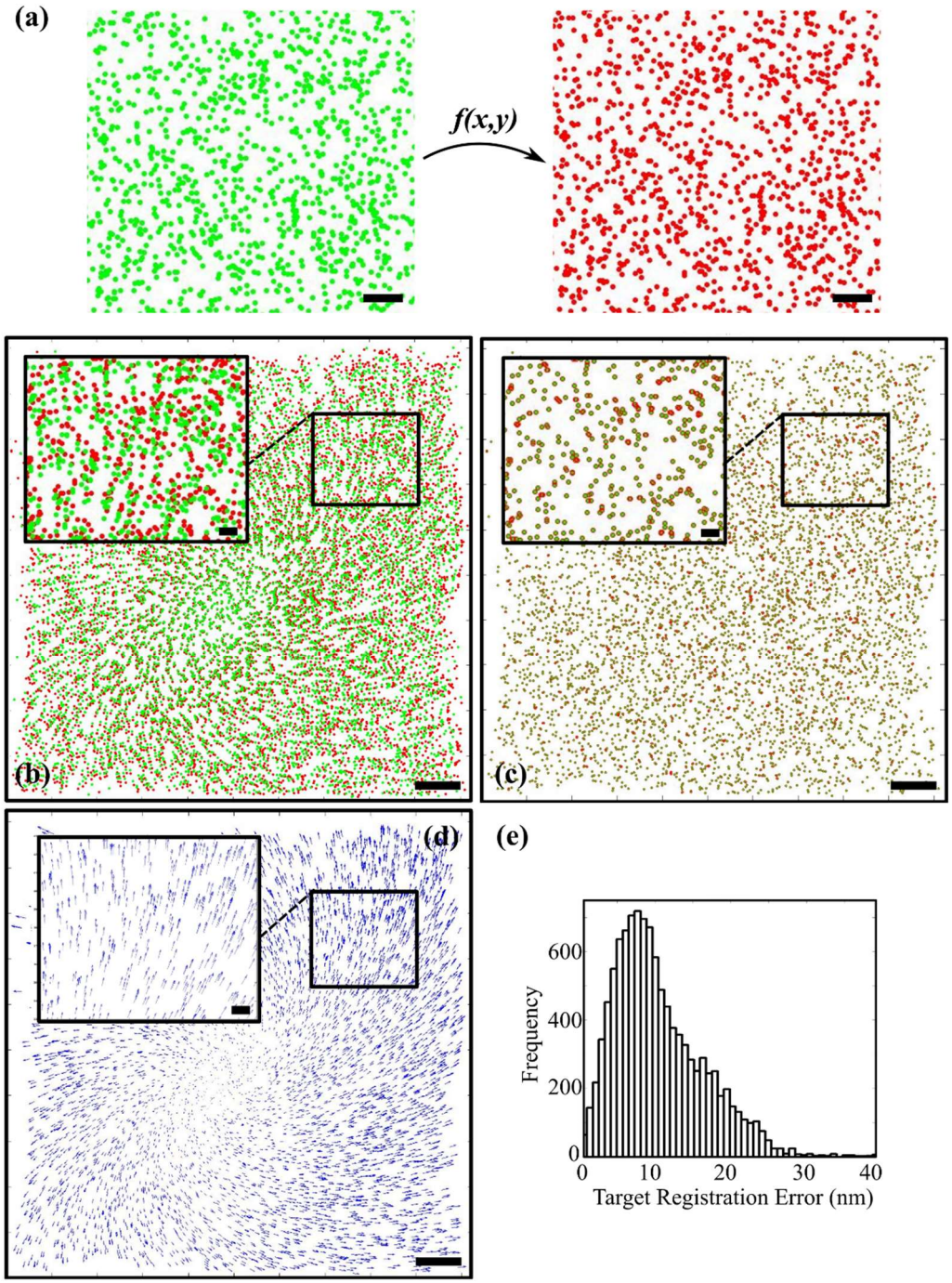

Figure 5.3 – Image registration in dual color SMLM. (a) Fiducial markers distributed in the field of view of the green channel are registered to the corresponding pairs in the red channel using a mapping function, $\boldsymbol{f}(\boldsymbol{x},\boldsymbol{y})$. The fiducial markers in the green and red channels (b) before and (c) after image registration. (e) A vector field presentation of the mapping function. (d) Distribution of the target registration error. Scale bars in: (a) 2 µm; (b) 5 µm and insets: 1 µm.

5.2 Results and Discussion

5.2.1 Distribution of the Type-2 Ryanodine Receptors in the Rat Cardiomyocyte

The organization and distribution of the Type-2 ryanodine receptors (RyR2) in the rat cardiomyocyte were investigated using a super-resolution imaging system. Diffraction-limited images of RyR2 clusters in a region close to the surface of the rat cardiomyocyte (Figure 5.4a) revealed that RyR2 is primarily distributed along successive Z lines. The corresponding super-resolution image, however, clearly resolved the sub-diffraction features of RyR2 distributions in a rat cardiomyocyte (Figure 5.4b). It is apparent that a large number of RyR2 exist and the RyR2s are far more widespread than one would expect based on diffraction-limited images. A series of small RyR2 clusters were found on either side of a T-tubule (see the blue-boxed insets labelled as b1 and b2 in Figure 5.4b). These two groups of clusters have a length of about 600 nm, while the individual clusters averaged about 100 nm in diameter. The maximum width of T-tubules here was determined to be about 100 nm. Note that the diffraction-limited image showed only an amorphous blurred spot in the same region (the red-boxed region in a1).

RyR2s are distributed along both transverse and axial T-tubules with a remarkable variability in both the size and shape of clusters (Figure 5.4c). RyR2 clusters are also distributed along the cross section of a T-tubule (Figure 5.4d). The diameter of the T-tubules and the RyR2 clusters were determined to be about 200 nm and 80-100 nm, respectively. A Z-line spacing of 1.78 μm on average was measured from these super-resolution images. The lateral and axial resolutions were determined to be about 20 nm and 50 nm, respectively. A 2-D projection of localizations within a 250nm thick image stack was used to obtain these super-resolution images (i.e. intensity maps, where the intensity is proportional to the number of blinks in a pixel).

We were able to obtain super-resolution images of RyR2 over a broad region (up to 50x50 µm) from the surface to the interior of a rat ventricular myocyte (up to 6 µm deep within the cell). RyR2 distribution on the cellular surface (Figure 5.5a) is very different from that in the interior (Figure 5.5b). While the Z-lines are obvious at a depth of ~ 6 µm, RyR2 clusters on the surface are distributed such that it is not easy to recognize individual Z-lines in some regions (Figure 5.5c-d). Collecting data from a large volume of the cell allowed us to perform a rigorous analysis without bias from regional variations. This observation led us to ask two major questions: 1) How much RyR2 is there in the ventricular cardiomyocyte (i.e. receptor density)? 2) How big are the clusters of RyR2?

5.2.2 Analysis of Receptor Density

The individual RyR2 is about 30 x 30 x 25 nm in size, so we applied a 40 x 40 x 40 nm^3 grid to the images (to account for variations in orientation, the attached antibodies, as well as errors in localization). The image is sectioned to exclude the nucleus and edges as well as z planes near the top and bottom of the image where the number of blinks is lower than the average of the central planes. Each voxel is examined and if it contains a blink, it is marked as containing a tetramer. Doing this with 15 images allowed for an estimation of RyR2 density, which was found to be 3.03 x $10^5 \pm 0.08$ RyR2 / pl. This number is far larger than that reported by an earlier study in which ^{3}H-Ryanodine was found to bind to about 2,000,000 RyR2 per cardiomyocyte [120]. Assuming that the average ventricular myocyte has a volume of 30 pl, this would give an estimate of ~ 6.6 x 10^4 RyR2 / pl. It may be argued that this large number is due to greater than estimated localization errors; however, even if the box is increased to 45 x 45 x 45 nm^3, the density is still high (i.e. 2.64 x $10^5 \pm 0.07$ RyR2 / pl). Our estimates are perhaps low because not every RyR2 is labeled by a fluorophore and not every fluorophore blinks. Further, many blinks were excluded because they

were too dim or too bright, the fitting was poor, or they had localization errors greater than our set limits.

If there are more receptors than has been previously reported, how would we reconcile this difference? ^{3}H-Ryanodine only binds to activated RyR2 so it is possible that additional receptors that we have found are inactive and detected only by the fluorophore. One may speculate, on the basis of our phosphorylation that these are 'receptors in waiting' which move into tighter clusters when activated.

5.2.3 RyR2 Cluster Analysis

Applying the same 40 x 40 x 40 nm^3 grid to the image, each super-resolution image was converted into a binary image and examined for 18-connectivity (Figure 5.6a). Two voxels were treated as part of the same cluster if they have faces or edges in common, but not their corners. In Figure 5.6a, the red cube is 18-connected to the blue cubes and form part of a cluster, while the green cube is outside the cluster. As a result of the coarseness of the grid, the technique mainly identifies super-clusters, rather than the smaller groupings within the clusters.

An example of the RyR2 cluster analysis is shown in Figure 5.6b-d. A pseudo-colored super-resolution image of RyR2 clusters in a rat ventricular myocyte is shown in Figure 5.6b, where clusters are color-coded according to the size (red: < 600 nm, orange: 600-1000 nm; yellow: 1000-1400 nm; green: 1400-1800 nm and blue: > 1800 nm). Clusters with a very high number of tetramers (up to 1200 tetramers per cluster) were determined in this super-resolution image (Figure 5.6c). The extent of cluster size varied from ~ 150 nm to 1 μm, where clusters with less than 100 localizations were excluded for clarity (Figure 5.6d).

5.2.3.1 Effects of Phosphorylation on RyR2 Cluster Size and Distribution

In order to investigate the effects of phosphorylation on RyR2 distribution, ventricular myocytes were permeabilized with saponin (electron-tomographic data suggests that saponization alone has no effect on the tetramer organization) and then treated with a cocktail containing 10μM/L Okadaic acid 10μM/L c-AMP, 10μM/L IBMX, 0.5 μM/L Calyculin A (CalA) and Thapsigargin for 10 min, after which the cells were fixed with 4% paraformaldehyde, permeabilized again and labeled with Alexa 647, as previously described. The super-resolution images of these cells revealed that RyRs became clustered together, forming a more clumped and discontinuous distribution. This observation is in alignment with electron tomographic analyses of RyR2 distribution, which demonstrated that the tetramer arrangement within the dyadic cleft can be altered by phosphorylation [121].

The mean RyR2 cluster size for the phosphorylated cells is significantly different from that of the untreated rat cardiomyocytes. The difference is even more marked when the smaller clusters are excluded from the analysis. Phosphorylation produced a significant increase in the number of tetramers associated with the clusters. Thus, this data supports the contention that phosphorylation encourages the movement of the RyR into clusters and that the positioning of RyRs are probably dynamic and not fixed.

Table 5.1 - Effects of phosphorylation on RyR2 cluster size and distribution.

RyR Cluster Parameters	Fixed Myocytes (N = 10)	Phosphorylated Cells (N = 3)
Mean size (nm)	12.5 ± 2.4	21.8 ± 3.9
Mean size for clusters > 200 tetramers	485.7 ± 75.4	769.2 ± 111.7
Cluster extent (nm)	323.7 ± 30.5	368.4 ± 27.3

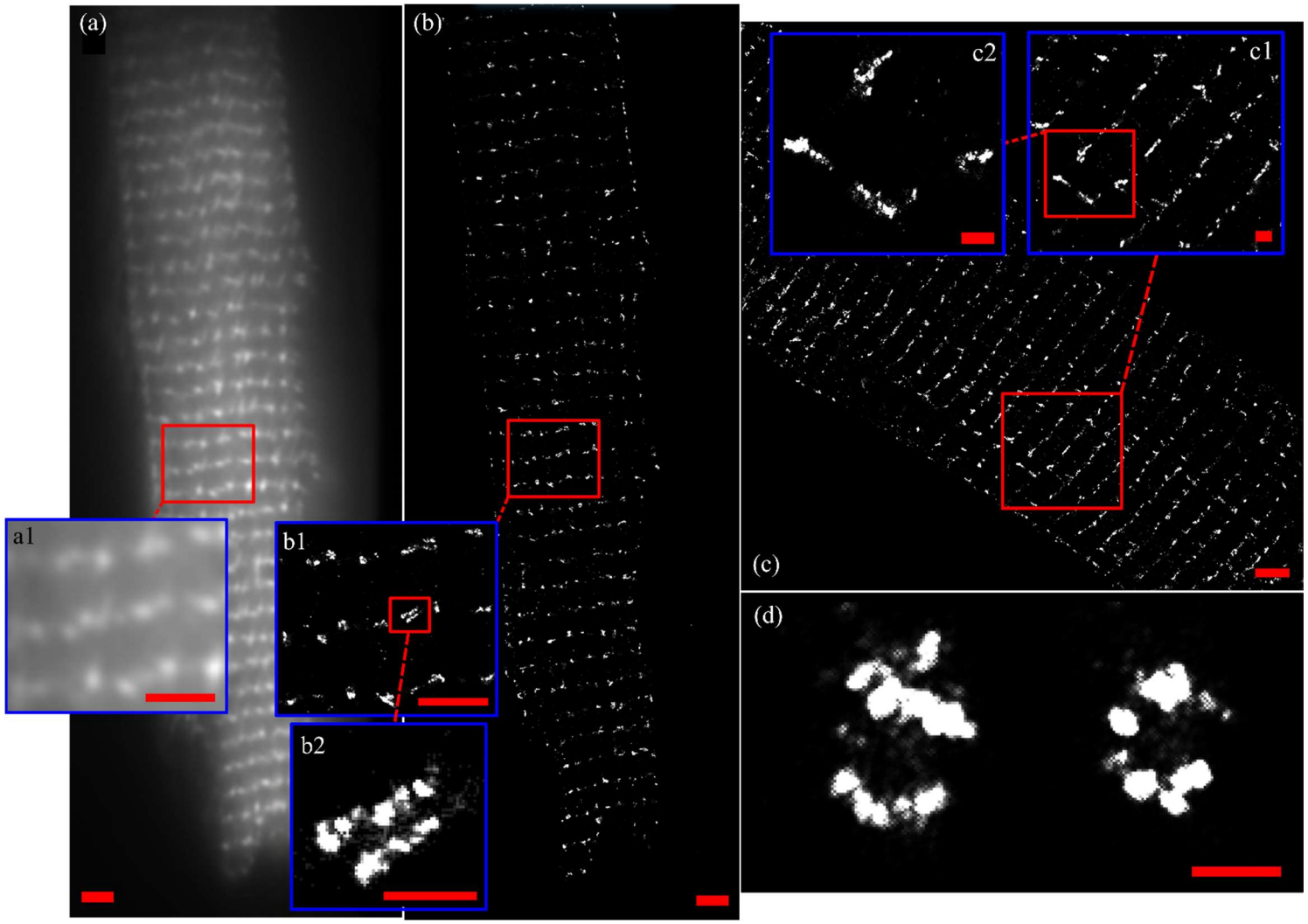

Figure 5.4 - Super-resolution imaging of RyR2 in rat ventricular myocytes. a) A diffraction-limited image of RyR2 in rat ventricular myocytes. (b) A super-resolution image showing RyR2 distribution in a rat ventricular myocyte (c) Distribution of RyR2 along the axial and transverse T-tubules. (d) RyR2 clusters distributed around the cross section of T-tubules. The images in blue boxes are the insets of the corresponding regions marked by red boxes. Scale bars in (a-c): 2 µm, (e): 200nm and all insets: 500 nm.

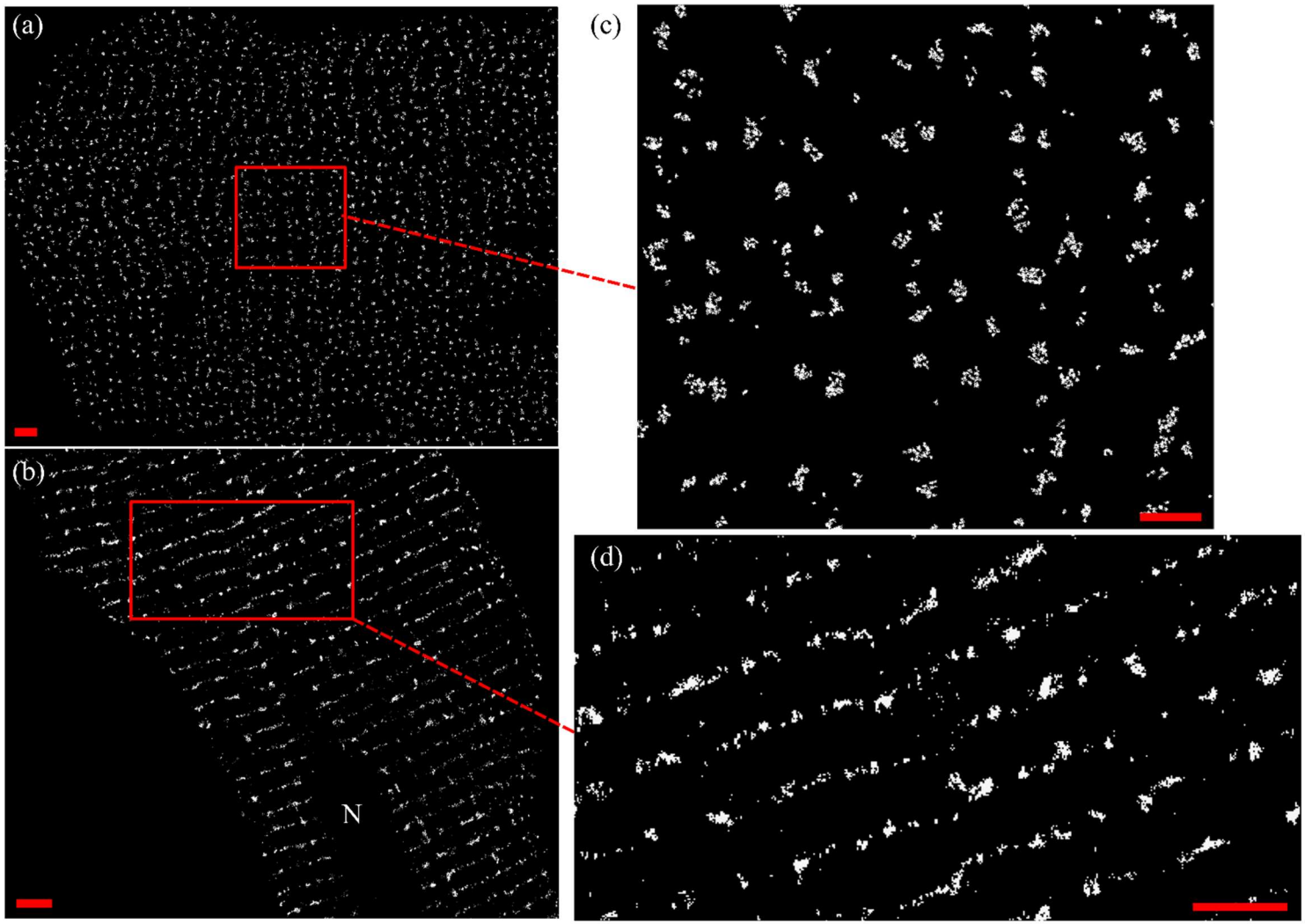

Figure 5.5 - Distribution of RyR2 clusters on the surface and in the interior of rat ventricular myocytes. a) A super-resolution image of RyR2 clusters on the surface and (c) in the interior of rat cardiomyocytes (imaging depth = 3 µm). N denotes the cell nucleus. (c-d) Insets of the regions marked by red boxed in (a-b). Scale bars in (a-b): 6 µm, (c-d): 1 µm.

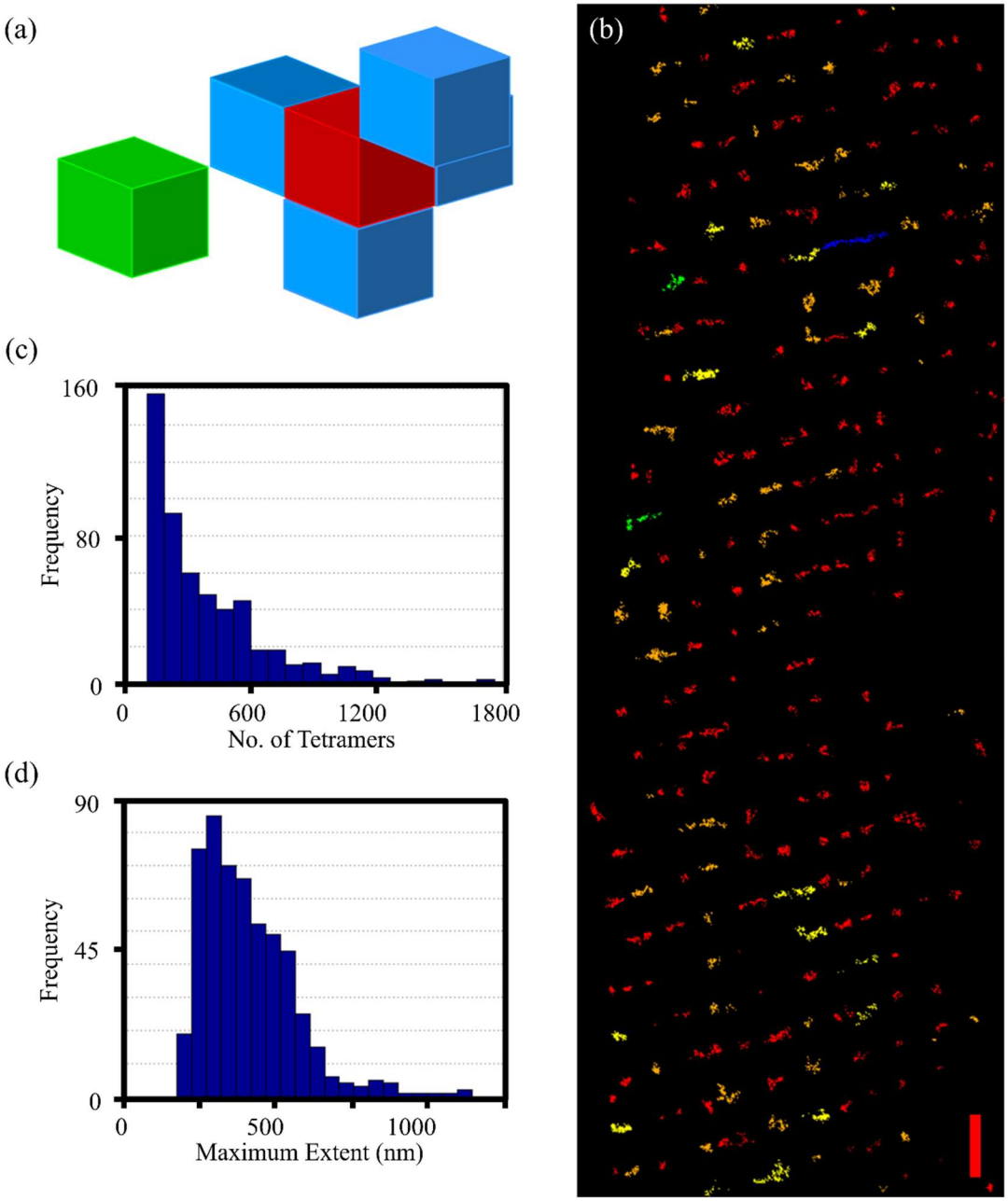

Figure 5.6 - RyR2 cluster analysis in rat ventricular myocytes. (a) Schematic representation of the 18-connectiviy method used for the cluster analysis. The red cube is 18-connected to the blue cubes and forms part of a cluster, while the green cube is outside the cluster. **(b)** A pseudo-colored super-resolution image of RyR2 clusters in a rat ventricular myocyte. Clusters are color-coded according to the size (red: < 600 nm, orange: 600-1000 nm; yellow: 1000-1400 nm; green: 1400-1800 nm and blue: > 1800 nm). **(c)** A histogram of the number of tetramers per cluster. (d) A histogram of the extent of cluster size. Clusters with less than 100 localizations have been excluded for clarity. Scale bar: 2 µm.

5.3 Two-Color Super-Resolution Imaging of RyR2 and $Ca_v1.2$

The colocalization of RyR2 and $Ca_v1.2$ in rat ventricular myocytes was investigated using the dSTORM system. Since the two colors were collected on different imaging paths, one should first validate that the mapping of the images (i.e. image registration) is accurate. We validated two-color mapping by labelling RYR2 with both Cy3B and Alexa 647 and then measuring the overlap between the two images. RyR2-RyR2 dual label super-resolution images (Figure 5.7) displayed an average overlap of 85.4%. Although there is some difference between the red and green images (probably due to differences in antibody binding affinity and blinking probability), this data assured us that the mapping was accurate. Note the overlapping of green and red images in the region around the T-tubule indicated by the red arrow in Figure 5.7.

Two-color super-resolution imaging of RyR2 and $Ca_v1.2$ in rat ventricular myocytes was conducted on the cellular surface, close to the cell surface (depth = 500 nm) and 3 μm deep in the interior of the cell (Figure 5.8-7). Two surface images with single and double rows of RyR2 (presumably on either side of the Z-lines), are shown in Figure 5.8a and b, respectively. Insets of the areas marked by red boxes in Figure 5.8a-b are shown in Figure 5.8c-d, where the colocalization of RyR2 and $Ca_v1.2$ along the Z-lines (marked by red arrows) and around the cross section of a T-tubule (marked by yellow arrows) can be observed.

For the image on the cellular surface, one can estimate the number of RyR2 in a cluster by taking the area of each cluster and dividing it by 900 nm^2 (i.e. the area of one receptor when viewed from above). As there is no information about the size or the packing of $Ca_v1.2$, an equivalent calculation for $Ca_v1.2$ is not possible. Table 5.2 shows the results of the cluster analysis of RyR2 and $Ca_v1.2$ on the cell surface.

The distribution of RyR2 changes just beneath the surface, forming small isolated clusters, although a few show the elongated shape typical of the cell interior (Figure 5.9). Since this is a transitional region, there are two types of clusters in this image. The circular clusters are quite isolated with an edge-to-edge nearest neighbor distance (NND) of 1.25 μm, while the longitudinal clusters (on the left) have a mean edge-to-edge NND of 374 nm. The degree of overlap seems to be less at a depth of 3 μm (Figure 5.10). Note the frequent axial tubules observed at these depths (see insets on the top), along with the transverse tubules (see inset on the right).

In brief, the results of the two-color super-resolution imaging of RyR2 and $Ca_v1.2$ in rat ventricular myocytes can be summarized as follows:

- The majority (> 95%) of RyR2 clusters had some overlap with $Ca_v1.2$, indicating that large extra-dyadic clusters are a rarity.
- The $Ca_v1.2$ clusters are generally smaller than those of RyR2, consistent with previously reported results by Scriven *et al.* [115].
- The distribution of RyR2 and $Ca_v1.2$ parallel each other and vary greatly between the surface, just below it, and deep in the interior. This is consistent with the view that the surface and interior of the myocyte have different molecular architectures.
- There is large cluster-to-cluster variation in overlap as well as in cluster size of both RyR2 and $Ca_v1.2$ implying that there is no 'typical' couplon.

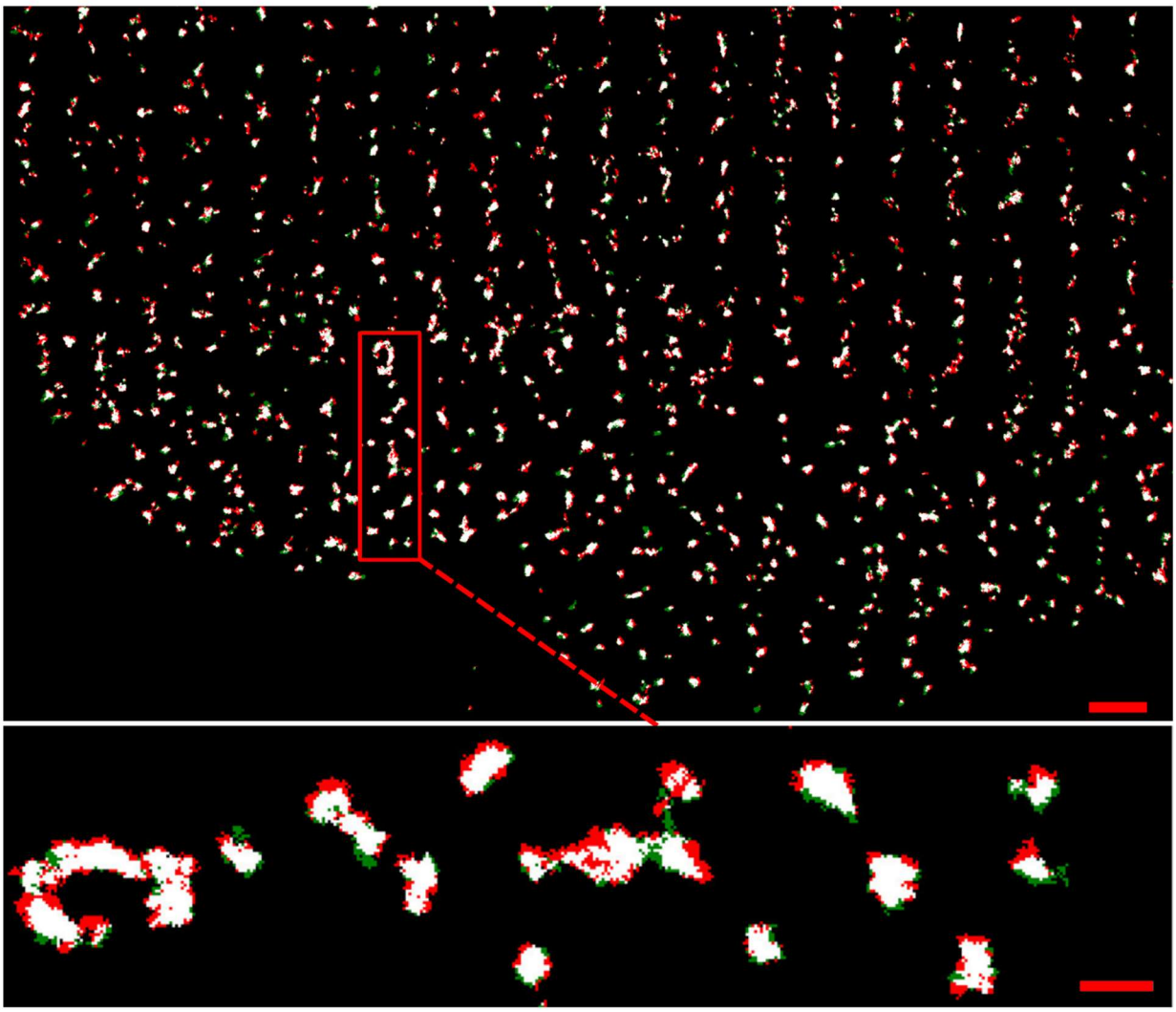

Figure 5.7 - Two-color super-resolution imaging of RyR2 in rat ventricular myocytes. RyR2-RyR2 dual label super-resolution image (top) and inset of the red-boxed region (bottom); Cy3B label in green, Alexa 647 label in red and the overlapping voxels in white. Raw image contained 4.5 million blinks in the green channel and 5.5 million in the red. Projection of a 200 nm thick slice, pixel size 20 nm, scale bars in (a) 2 µm and (b) 500 nm.

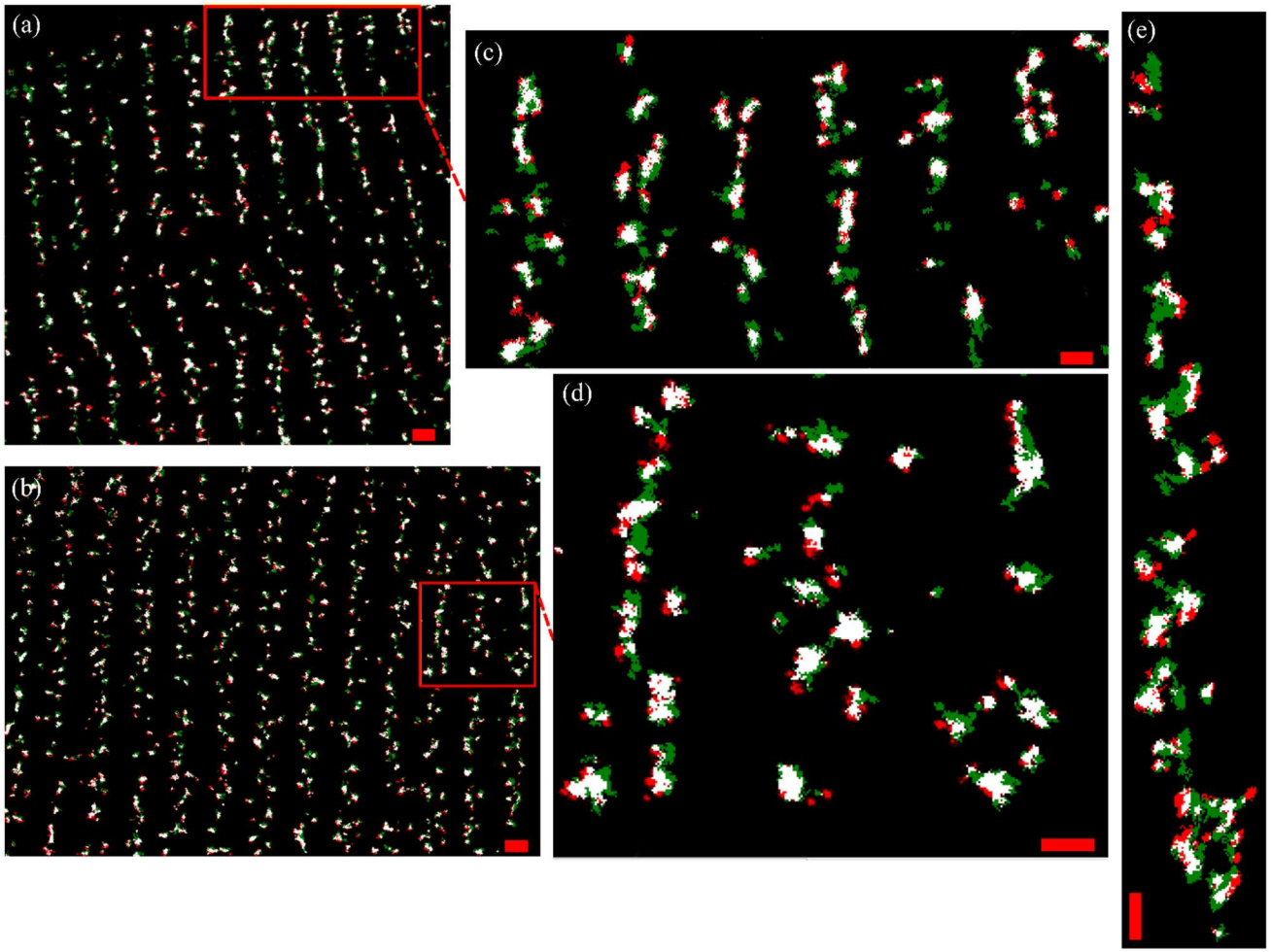

Figure 5.8 - Distributions of RyR2 and $Ca_v1.2$ on the surface of a rat ventricular myocyte. Two cell surface images with single rows of RyR2 (a) and double rows, presumably on either side of the Z-lines (b). (c-d) Insets of the red-boxed regions in (a-b). (e) A Z-line from a different cell. RyR2 in green, $Ca_v1.2$ in red and the overlapping voxels in white. Pixel size 20 nm. Slice: 200 nm thick. Scale bars in (a-b): 1 µm and (c-e): 500 nm.

Table 5.2 - Cluster analysis of RyR2 and $Ca_v1.2$ on the surface of a rat ventricular myocyte. Image (a) and (b) refer to the images in Figure 5.8.

Image	RyR2 Clusters/µm²	RyR2 Cluster Size (nm²)		# RyR2/ cluster				$Ca_v1.2$ Clusters/µm²	Mean $Ca_v1.2$ Cluster Size (nm²)	$Ca_v1.2$/RyR2 Area Ratio
		Mean	Median	Mean	Median	Min	Max			
(a)	1.47	40138	30825	44	34	1	285	1.21	31486	0.76
(b)	3.54	30418	22275	34	25	1	230	2.89	22164	0.73

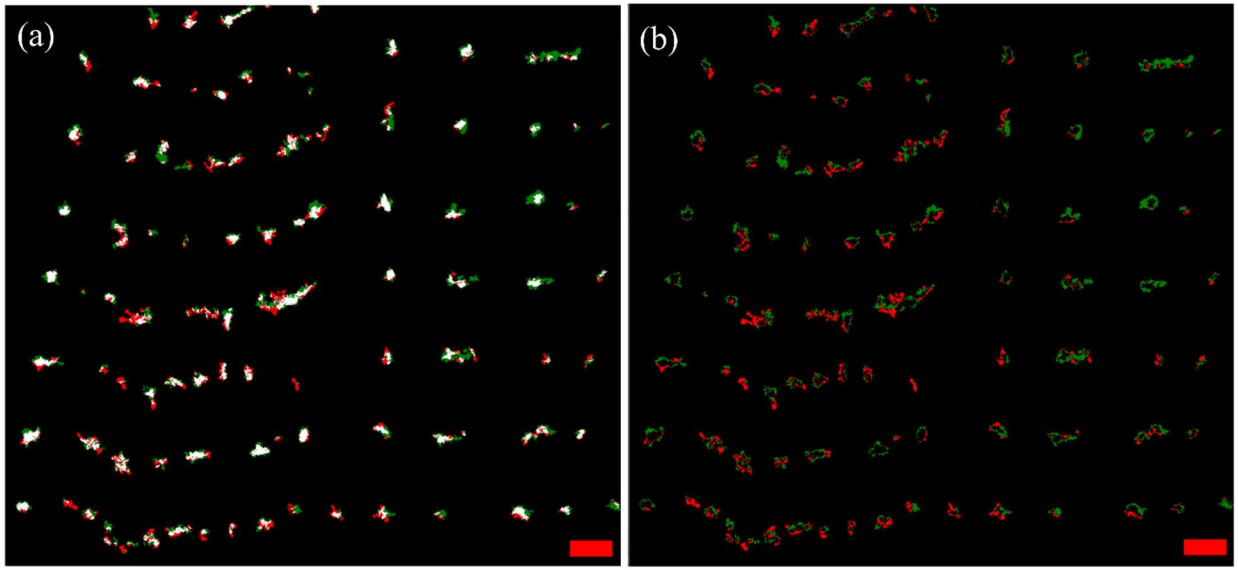

Figure 5.9 - Distributions of RyR2 and $Ca_v1.2$ in a region close to the surface of a rat ventricular myocyte. The image at the bottom is identical to the one on the top except the overlapped areas are omitted. RyR2 in green, $Ca_v1.2$ in red and the overlapping voxels in white. Imaging depth: 500 nm. Pixel size 20 nm. Slice: 200 nm thick. Scale bar: 1 µm.

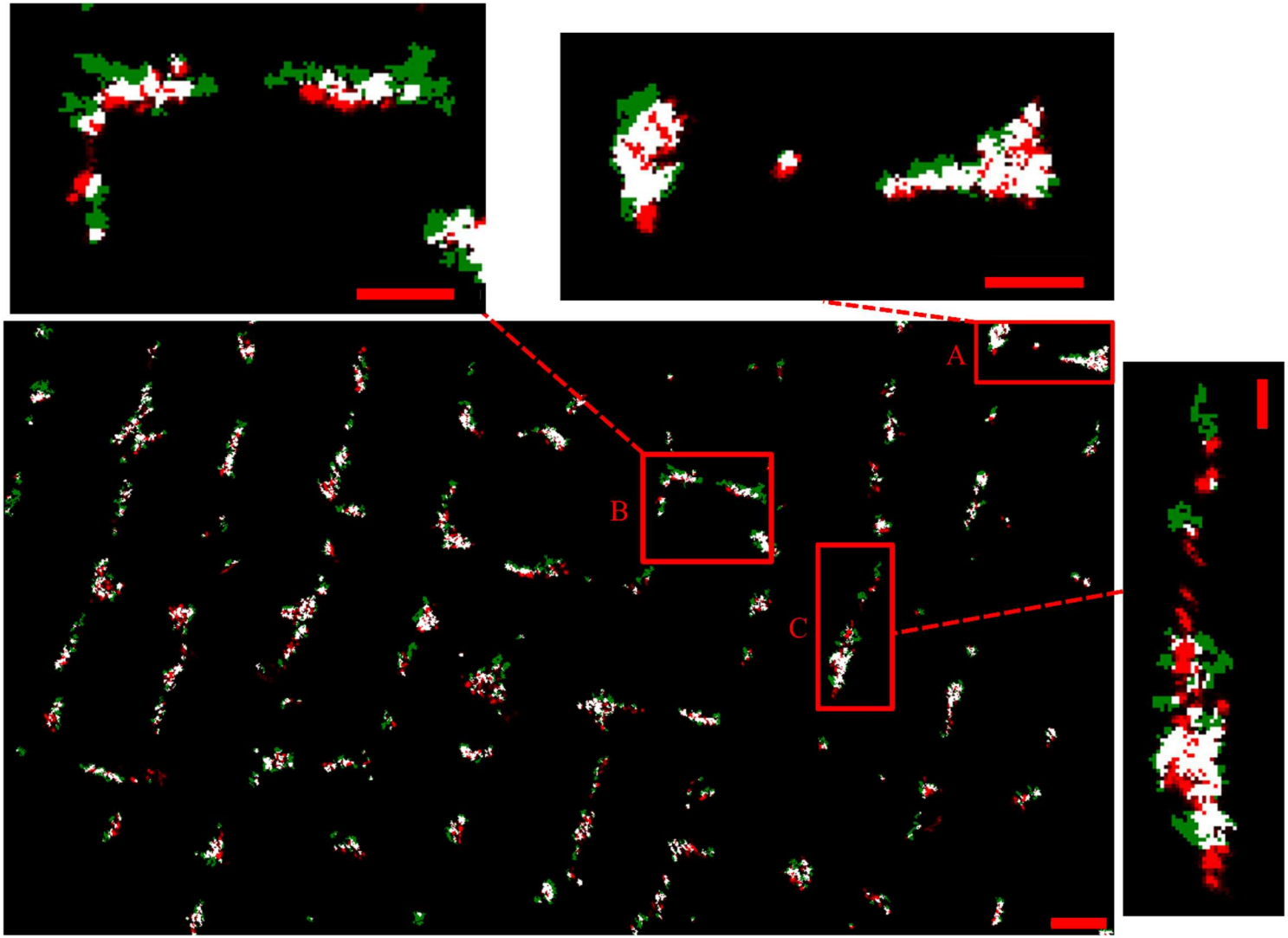

Figure 5.10 - Distributions of RyR2 and Cav1.2 in the interior of a rat ventricular myocyte. RyR2 in green, $Ca_v1.2$ in red and the overlapping voxels in white. Imaging depth: 3 µm. Pixel size 20 nm. Slice: 200 nm thick. Scale bars: 2 µm in the main figure and 500 nm in the insets.

5.4 Conclusion

- We accurately imaged receptors down to a depth of 6 µm below the surface.
- For the first time, using light microscopy, we were able to image individual receptors and confirm Asghari *et al.* (2014) findings that these receptors in a cell at rest were not organized in a checkerboard, but rather, had a variety of cluster arrangements.
- RyR2 had markedly different distributions depending on where it was measured: the surface, just below it (250-500nm) or deep within the cell. This is consistent with previously reported results by Scriven *et al.* [122] that the surface and interior of the myocyte have different molecular architectures. On the surface, the mean edge-to-edge difference was about 175 nm, while just below the surface - a transitional region, there are two types of clusters: circular and longitudinal. The circular clusters are quite isolated, with an edge-to-edge distance of 1.25 µm, while the longitudinal clusters have a mean edge-to-edge nearest neighbour distance (NND) of 374 nm.
- Phosphorylation of the cell seems to increase the size of the tetramer clusters. Network analysis has confirmed this.
- Like RyR2, clusters of $Ca_v1.2$ on the myocyte surface are significantly different from those in the cell's interior. In all locations, $Ca_v1.2$ clusters are significantly smaller than RyR2 clusters. This is consistent with previously reported results by Scriven *et al.* [115].
- If one assumes a 10 nm radius for $Ca_v1.2$, then each cluster could contain as many as 8 channels, probably as a collection of dimers. This estimate ignores the size of the antibodies and the real value is potentially much less.
- We validated two-color mapping by labelling RyR2 with both Cy3B and Alexa 647 and then measuring the overlap between the two images.

- The majority (> 95%) of the RyR2 clusters had some overlap with $Ca_v1.2$, indicating that large extra-dyadic clusters are infrequent.
- The distribution of RyR2 and $Ca_v1.2$ parallel each other and vary greatly between the surface, just below it and deep in the interior. This is consistent with the view that the surface and interior of the myocyte have different molecular architectures.
- Colocalization in the classical sense has little meaning at this high of a resolution, since the degree of overlap varies from 15-85% depending on the cluster examined. In addition, some of the $Ca_v1.2$ is next to, or partly overlapping with the RyR2s at a distance close enough to exert an effect. Similarly, the RyR2 cluster sizes are extremely variable ranging from two to over 200 tetramers. These findings indicate that there is no 'average' or 'typical' couplon.

Chapter 6: Receptor Organization as the Basis for the Priming of Marginal Zone B Cells

6.1 Introduction

The immune system consists of biological structures and processes within an organism that protect against disease. To function properly, an immune system must (1) detect a wide variety of foreign agents (hereafter collectively termed 'pathogens'), and (2) distinguish them from the organism's own healthy tissue. The immune system can be broadly classified into two components: the innate immune system and the adaptive immune system. The innate immune system has various structures, specialized cells, and serum proteins that act as the first line of defense against pathogens. Anatomical and physiological barriers such as lysozyme in tears, the skin, and the cilia in the respiratory system broadly and non-specifically prevent infection [123]. When these barriers are breached by pathogens, innate cells such as dendritic cells, neutrophils, and macrophages are rapidly recruited to sites of infection to provide non-specific cellular responses to eliminate the pathogen. These innate immune cells express pattern recognition receptors (PRRs), which recognize conserved molecular patterns on pathogens called pathogen-associated molecular patterns (PAMPs) [124]. In sharp contrast, the adaptive immune system consists of specialized cells called lymphocytes that produce highly specific responses against a pathogen [125]. In addition, adaptive immunity is characterized by immunological memory, where upon encountering the same pathogen a second time, a rapid and effective response is mounted [125]. While the reaction of the innate immune system is rapid (within minutes), the adaptive immune system is slower and takes ~4-7 days to mount an immune response [123, 124, 126]. In fact, both the innate and the adaptive immune system work together synergistically to maximize protection against pathogenic infections [125].

The adaptive immune responses can be further categorized into two constituents: (1) cell-mediated immunity, mediated by T cells, which combat intracellular pathogens (e.g. viruses) and cancerous cells, and (2) humoral immunity, mediated by macromolecules (as opposed to cells) found in the extracellular fluid [126]. B cells play a central role in humoral immune responses by secreting antibodies against extracellular pathogens and toxins. This is primarily achieved by B cell receptors (BCRs) on the cell surface of B cells, which recognize specific molecular epitopes on pathogens [126].

6.1.1 BCR Complex and BCR Signalling

The BCR is a multi-chain transmembrane receptor located on the surface of all B cells. Every BCR consist of two heavy and two light immunoglobulin (Ig) chains, linked via disulfide bonds. Depending on the amino acid sequence of the heavy chain five BCR isotypes exist, namely IgD, IgM, IgA, IgG, or IgE. The membrane Ig binds to specific molecular pattern on pathogens, called antigens, via the antigen binding site. All BCR isotypes are non-covalently associated with a disulfide-linked heterodimer consisting of the Igα (CD79a) and Igβ (CD79b) polypeptides, to form the 'BCR complex'. The CD79a-CD79b heterodimer functions as the signal transduction moiety of the BCR complex (Figure 6.1).

All mature naïve B cells express two BCR isotopes on their cell surface – IgM and IgD. Though the functional relevance and existence of these two BCR isotypes on the B cell surface is not clear, it is proposed that both isotypes exist in separate and discrete membrane domains [127, 128]. Upon antigen engagement, BCRs initiate a cascade of downstream signaling events, collectively termed 'BCR signaling'. Briefly, the cytoplasmic domains of the CD79a-CD79b chains (the signalling subunit of the BCR complex) are phosphorylated by the Src family kinase, Lyn. This creates binding sites for additional Src family kinases, which then phosphorylate and activate a number of

downstream signaling proteins, leading to the activation of multiple signaling pathways [129-131]. These signaling pathways control the activity of a number of transcription factors, which promote B cell survival, activation, proliferation, and differentiation [130, 132, 133].

The strength of BCR signaling dictates the extent of B cell activation. Based on this, B cells are thought to exist in 3 different states - resting, partially activated or 'primed', and activated. Most B cells exist in the resting state and spontaneous activation (in the absence of antigen) is prevented by various 'safety mechanisms' in the cell. In sharp contrast, an activated B cell differentiates into a plasma cell and secretes their cell surface BCRs as soluble antibodies. These secreted antibodies are very important in mediating a variety of humoral immune responses, as they bind to pathogens and pathogenic components allowing additional immune responses to be induced. Of note, the nature of partially activated B cells is poorly understood.

Importantly, BCR signaling also occurs basally in the absence of any antigen and is referred to as 'tonic signaling'. Although the precise mechanisms that regulate tonic signaling in B cells is largely unknown, tonic signaling is important for B cell selection, survival and maintenance [134]. It is proposed that partially activated B cells have higher tonic signaling and can more rapidly transition into a fully activated state. However, direct evidence for higher tonic signaling in these cells has not been established so far. The magnitude of tonic signaling is also important for normal B cell function and aberrant BCR signaling is implicated in many autoimmune diseases (where immune responses are elicited against self-antigens) and B cell malignancies [135-137].

6.1.2 Models of BCR Organization and Signalling

BCR signaling is tightly coupled to the spatial organization and dynamics of BCRs on the cell surface and various models have been proposed (as reviewed in detail by [138]). The first model is called the 'conformation induced oligomerization model' and it suggests that BCRs exist

primarily as monomers on the cell surface of resting B cells and as large clusters/micro-clusters post-antigen crosslinking [139]. An alternate second model, named the 'dissociation-activation model', proposes that BCRs exist predominantly as tightly packed inactive oligomers in resting B cells and after antigen crosslinking, they dissociate and undergo activation [140, 141] A third and more recent model was developed based on the 'picket-fence model' of the plasma membrane [142]. According to this model ('collision coupling model'), the steady state BCR diffusion on the B cell surface and signaling from the BCR is restricted and tightly regulated by the membrane actin cytoskeleton [143]. This model suggests that BCRs are spatially separated from activating co-receptors or kinases (that act as positive regulators of BCR signaling) by the actin cytoskeleton and activation is associated with changes in the BCR mobility on the cell surface, which allows for the functional interaction of these elements.

More recently, dSTORM analysis showed that BCRs exist as nanoclusters with diameters ranging from 120-160nm on the surface of resting B cells. Upon antigen engagement, these BCRs formed micro-sized clusters, with diameters ranging from 300-400nm [128, 144]. Though all of these models are valid to a certain extent in describing the BCR organization and dynamics in resting and fully activated B cells, the nature of BCR organization in partially activated B cells is largely unknown.

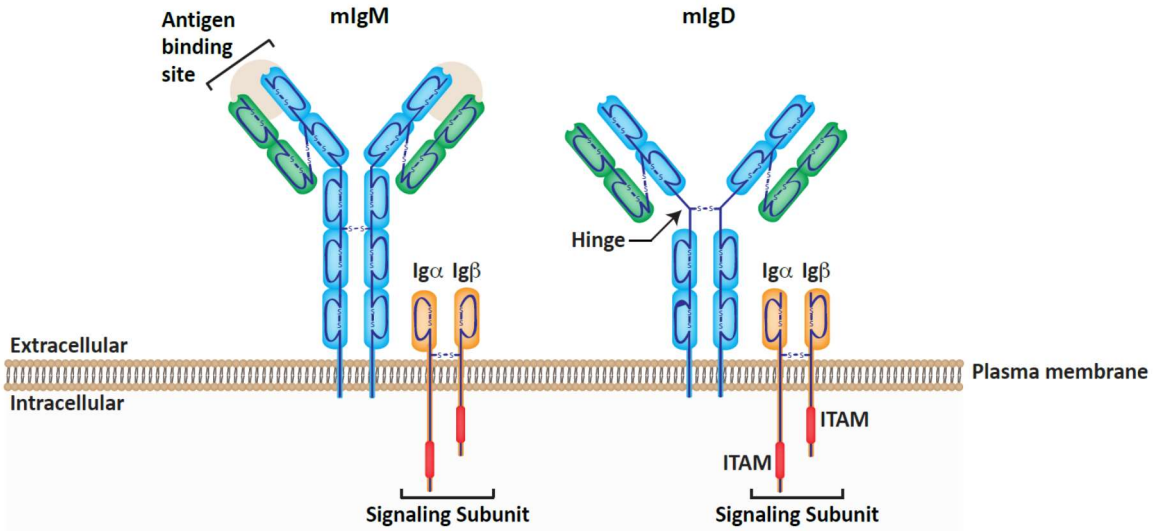

Figure 6.1 - Structure of B cell receptor complex (BCR). The BCR complex consists of an antigen-binding subunit, the membrane immunoglobulin (mIg), and the non-covalently associated Igα/Igβ signaling subunit (indicated in brown). The heavy chain of mIg is displayed in blue, and the light chain is shown in green. Each mIg has two identical antigen-binding sites. mIgM (left) and mIgD (right)-containing BCRs with the identical antigen-binding sites being co-expressed on the surface of mature naïve B cells. Unlike mIgM, mIgD have flexible hinge regions that may enhance their ability to bind pathogens with repeating antigenic patterns. The Igα and Igβ chains both contain binding sites for tyrosine kinases (shown in red) that initiate BCR signaling [145].

6.1.3 Marginal Zone B (MZ) Cells

The spleen is a lymphatic organ and is the body's largest blood filter. It plays a fundamental role in protecting the body from invading pathogens [146]. In the mouse spleen, there are two main populations of B cells: circulating resting follicular (FO) B cells and the spleen resident marginal zone (MZ) B cells [124, 147-149]. FO B cells, which encompass 95% of murine splenic B cells, circulate throughout the body and migrate through the spleen back into circulation [150]. In contrast, MZ B cells are a rare population of spleen resident B cells (comprising 5-8% of total splenic B cells) that are strategically positioned in the marginal sinus of the spleen. The marginal sinus is located at the interface between the blood (which carry pathogens and pathogenic components) and immune cells in the spleen, and hence is similar to a 'filter,' whereby most circulating pathogens are captured [151]. This location allows MZ B cells to act as 'sentinels' or

‘first responders’ where they are able to rapidly detect and aid in the destruction of blood-borne microbial antigens through antibody production.

The swift anti-pathogen responses of MZ B cells are owed primarily to their ‘partially activated’ or ‘primed’ state [147, 151, 152]. Due to the higher basal activation state in these cells (presumably due to constant exposure to circulating pathogens), MZ B cells have lower thresholds for full activation. This allows for the rapid proliferation and differentiation of MZ B cells into antibody-secreting plasma cells in response to even small amounts of antigen [147]. This rapid response by MZ B cells is very important and beneficial to the host because it bridges the temporal gap that is required by FO B cells to produce high affinity antibodies [153]. MZ B cells on the other hand, make low affinity antibodies, which recognize conserved self and microbial molecular structures allowing response to both foreign antigens as well as host antigens, ultimately causing the clearance of microbes and apoptotic or damaged cells [147].

The mechanisms that render partially activated primed state in MZ B cells are not fully understood. It is hypothesized that MZ B cells have higher tonic BCR signaling but this has not been shown experimentally. Even though various models of BCR organization and dynamics have been proposed in resting and antigen-activated B cells (see previous section), the nature of BCR organization in MZ B cells is completely unknown. Based on the conformation induced oligomerization model, it is possible to assume that MZ B cells may have BCRs organized into larger oligomers/nanoclusters compared to resting FO B cells, which results in more tonic BCR signaling (Figure 6.2). Since MZ B cells have higher actin dynamics and BCR diffusion [154]. There could be a second explanation for higher tonic BCR signaling. This would be in accordance with the *collision coupling model*, where BCRs in MZ B cells exhibit more collisions with each other and other co-receptors of BCR signaling and they may exist in overlapping protein domains

of similar sizes (see model in Figure 3). Alternatively, a combination of both models might also be the basis for higher tonic BCR signaling. The overall aim of the study is to gain insights into the molecular basis of the primed state in MZ B cells by assessing the organization of BCR, signalling BCRs, and co-receptors on MZ B cells, when compared to resting FO B cells using dSTORM.

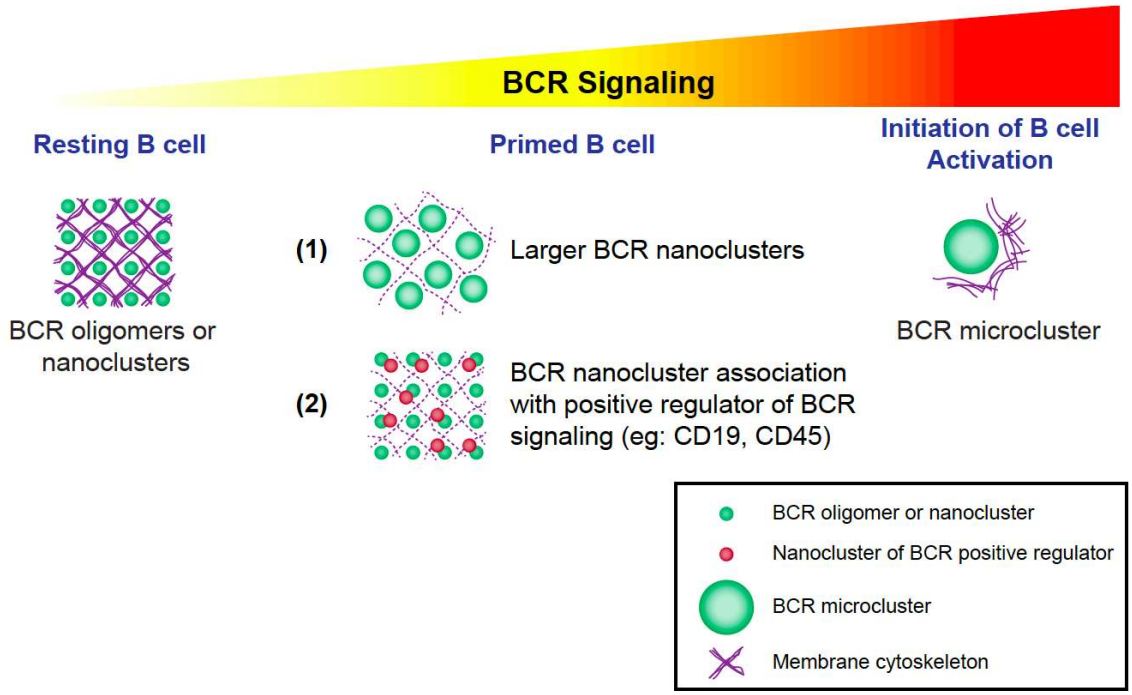

Figure 6.2 - Schematic representation of possible BCR organization in MZ B cell. Depicted is the organization of BCR and membrane actin cytoskeleton in resting B cell (left) and antigen-engaged B cell (right). In resting B cells, BCRs are organized as nanoclusters ((Mattila et al., 2013, Maity et al., 2015) and are spatially separated from each other by actin cytoskeleton that limit their free diffusion (Treanor et al., 2010, Treanor, 2012). In sharp contrast, the antigen-engaged B cells forms large BCR microclusters that can be visualized using diffraction-limited microscope (Fleire et al., 2006, Treanor et al., 2009). The organization of BCRs in primed MZ B cells is not known. Possibility (1) is the existence of BCRs in larger nanoclusters in MZ B cells when compared to FO B cell, formed by the fusion of smaller nanoclusters (middle panel). These larger BCR nanoclusters could contribute for higher tonic BCR signaling. Alternatively, BCRs in MZ B cells could also exist in nanoclusters of similar size (when compared to resting FO B cells), but these BCR nanoclusters in MZ B cells exist overlap with positive regulators of BCR signaling (possibility 2). A third possibility (not shown) could be the co-existence of both the scenarios, described above.

6.2 Material and Methods

6.2.1 B Cell Isolation

All experiments used splenic B cells from 8-week old C57BL/6 mice. Animal handling was done in accordance with the guidelines of the Canadian Council on Animal Care and approved by the animal research committee of the University of British Columbia (UBC). Spleens were harvested from mice of either sex and $CD21^{hi}CD23^{lo}$ MZ B cells were enriched using a MZ B cell enrichment kit (#130-100-366, Miltenyi Biotec).

6.2.2 Coverslip preparation and antibody adsorption.

Glass coverslips (18 mm^2; Marienfeld; #1.5H) were cleaned by sonication using an Ultrasonic Cleaner (VWR; Model 75T) for 30 min in 1M KOH to eliminate dirt particles if any, and then washed several times with double distilled water. Cleaned coverslips were coated with non-stimulatory M5/114 anti-MHCII monoclonal antibody (#12-5321, eBioscience) for 3 hr at 37^0C in an incubator or overnight at 4^0C in a fridge. Coverslips were then washed several times with PBS before use.

6.2.3 Sample preparation for dSTORM

Roughly 100,000 FO or MZ B cells were obtained in a V-bottom Nunc 96-well plate (Thermo Scientific; catalogue #167311) and cell surface BCRs were stained using a rat anti-mouse IgD (clone 11-26c) Alexa Fluor 647 Fab (#19-0069-13, AbLab), a goat anti-mouse IgM Alexa Fluor 647 Fab (#115-167-020, Jackson ImmunoResearch Laboratories), or a combination of both (for two color imaging) for 15 min on ice. Cells were then pelleted and washed thrice with ice cold PBS and plated at 4^0C on prepared coverslips for 15 min. Cells were subsequently fixed with ice cold 4% paraformaldehyde and 0.2% glutaraldehyde (PFA/GA, #15710, Electron Microscopy Sciences) in PBS for 90 min at 4^0C. Coverslips containing the cells were then washed several times

with ice cold PBS. Fluorescent fiducial markers (#F8800, Life Technologies) were incubated with the sample overnight at 4 °C for the purpose of sample stabilization during image acquisition.

For intracellular staining of signaling BCRs, B cells were plated at 4^0C on prepared coverslips for 15 min and fixed with 4% PFA in PBS for 90 min. Coverslips were washed several times with ice cold PBS and permeabilized with 0.1% Triton X-100 in PBS for 5 min. Cells were washed three times with PBS and blocked in 10% Normal Goat Serum (NGS; #005-000-121, Cedarlane Labs) made in PBS for 4 hours. Cells were then labeled with the primary antibody phospho-CD79a (p-CD79a; #5173, Cell Signalling Technologies) in 10% NGS overnight. Coverslips were washed three times with PBS and then stained with the secondary antibody goat anti-rabbit Alexa Fluor 647 (#A11036, Invitrogen) in PBS for 1 hr at room temperature. Cells were then washed three times with PBS and fluorescent fiducial markers were incubated with the sample overnight at 4 °C.

Imaging was performed in a standard GLOX-thiol solution (TN buffer [50 mM Tris, 10 mM NaCl, pH 8.0], 0.5 mg/ml glucose oxidase, 40 μg/ml catalase, 10% (w/v) glucose and 140 mM beta-mercaptoethanol). The coverslip along with the sample were mounted onto depression slides and sealed with a two-component silicone-glue Twinsil (Picodent, Wipperfürth, Germany, #13001000).

6.3 Results

6.3.1 IgM in MZ B Cells Exist as Dense Nanoclusters and Dispersed Oligomers

To visualize the molecular organization of endogenous BCRs on the surface of FO and MZ B cells, we implemented a drift-free direct stochastic optical reconstruction microscopy (dSTORM) system [155]. This method overcomes the resolution limit associated with conventional light microscopy, allowing localization of endogenous receptors to a positional accuracy of 10–30 nm in fixed cells. FO and MZ B cells were labeled with saturating amounts of Fab fragments directed

against the BCR isotype IgM, which were conjugated with the dSTORM-compatible fluorophore Alexa Fluor 647 (AF647), as previously described [144]. These cells were then settled under non-stimulatory conditions onto anti-major histocompatibility complex class II glycoprotein (MHCII) monoclonal antibody-coated coverslips for 15 min, prior to fixation to allow for the adhesion of cells. To selectively visualize BCRs in close proximity to the cell surface, samples were imaged by total internal reflection fluorescence microscopy (TIRFM).

BCRs on the surface of cells are highly dynamic (where nanoclusters are in constant diffusion and exist in an equilibrium, where they constantly fuse and separate from each other; unpublished data from Libin Abraham, Gold lab). dSTORM only offers a detailed overview of these nanoclusters at the time of cell fixation and therefore, molecular organization varies between cells. In addition, there is no prior knowledge about BCR organization in primary murine B cells using alternative high-resolution approaches, such as electron microscopy. The true organization of receptor nanoclusters requires sufficiently large number of localizations for correct image reconstruction. Drift-stabilized dSTORM imaging permits stochastic data acquisition for long periods of time and therefore allows for the accumulation of a sufficient quantity of single molecule localizations, which is very essential for fitting the reconstructions of nanoclusters with high accuracy. We performed 40,000 cycles and had the ability to obtain an average of ~50,000 localizations of IgM in B cells. Cells with localizations of less than 10,000 were removed from analyses to ensure that appropriate reconstructions with high fidelity are achieved.

The expression level of cell surface IgM is higher in MZ B cells when compared to FO B cells (Figure 6.3A; data provided by Libin Abraham, Gold lab). Visual inspection of dSTORM reconstructions readily revealed that IgM was not homogenously distributed in the B cell membrane. Instead, IgM on FO B cells were organized into heterogeneous nanoclusters of various

size, shape and density (Figure 6.3B). Since dSTORM cannot resolve lower molecular organizations of BCRs that exist as monomers, dimers, and small oligomers due to the over-counting of fluorophores [156, 157], we classified the distribution of BCRs into two broad classes: (1) nanoclusters, which comprise multiple localizations within a well-defined nanostructure, and (2) oligomers, which consist of a relatively few scattered localizations, which lack a well-defined nanostructure (as shown in Figure 6.3B). In sharp contrast to FO B cells, BCRs in MZ B cells were found to exist in denser nanoclusters with many dispersed oligomers (Figure 6.3B).

To quantify the extent of receptor clustering in resting B cells as seen by dSTORM, we used Hopkins index to ascertain the extent to which BCR displayed a nonrandom distribution on the B cell surface [158]. In line with our visual inspection of dSTORM reconstructions, IgM BCRs in FO B cells (with a median Hopkins index of 0.733), had a significantly higher Hopkins value than would be expected for a fully random distribution (0.5). This effectively demonstrates that IgM BCRs are not randomly distributed on the B cell surface. However, in MZ B cells, the median Hopkins index was closer to random distribution with a median value of 0.630. The relative diminishing of the Hopkins index values in MZ B cells is primarily attributed to the higher number of dispersed oligomers found in MZ B cells (Figure 6.3C). To quantify nanocluster features in molecular detail, we employed a novel method of nanocluster analysis method known as Voronoï tessellation segmentation [159, 160]. We found that nanoclusters of

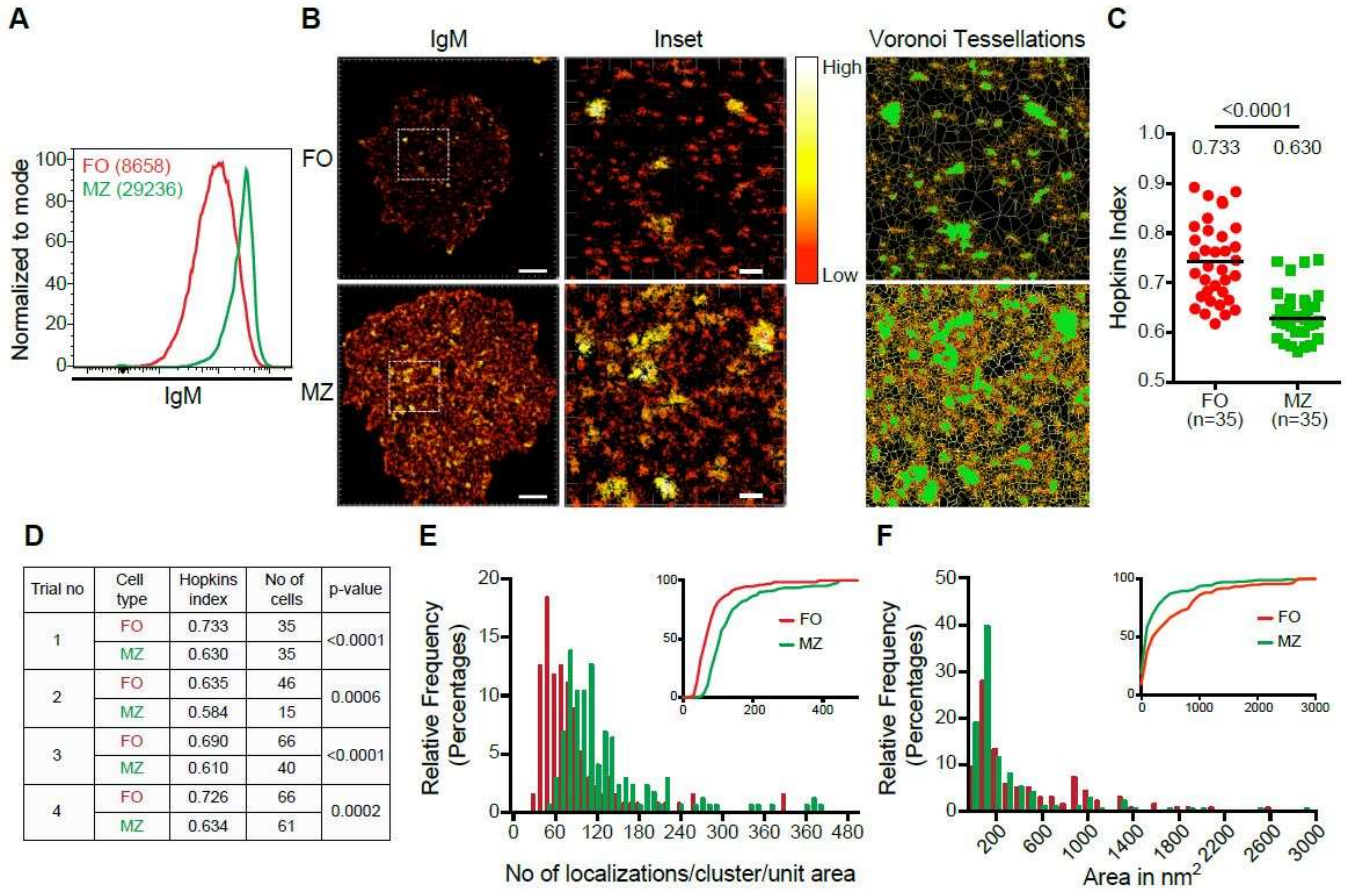

Trial no	Cell type	Hopkins index	No of cells	p-value
1	FO	0.733	35	<0.0001
	MZ	0.630	35	
2	FO	0.635	46	0.0006
	MZ	0.584	15	
3	FO	0.690	66	<0.0001
	MZ	0.610	40	
4	FO	0.726	66	0.0002
	MZ	0.634	61	

Figure 6.3 - IgM nanoclusters are heterogeneously distributed on the surface of B cells. (A) Flow cytometric analysis of cell surface IgM in FO and MZ B cell. **(B)** Representative STORM images reconstructed from single-molecule localizations of IgM in FO (*upper panel*) and MZ B cell (*lower panel*). Depicted is the density plot of localizations. Scale bar = 1µm. The magnified region in dashed white square is shown in the inset (*middle panel*). Scale bar = 200 nm. Cluster analysis based on Voronoi tessellations (*right panel*). Segmentation of the localization data points into clusters was performed using density threshold, which was set to twice the average localization density. **(C-D)** Quantification of the extent of IgM clustering using Hopkins index. Black bars indicate median values. **(E)** Relative frequency distribution of normalized density (number of localizations/cluster/unit area) of IgM nanoclusters in FO and MZ B cells. Cumulative frequency plot of relative frequency is plotted in the inset. **(F)** Relative frequency distribution of area of IgM nanoclusters in FO and MZ B cells. Cumulative frequency distribution plot of relative frequency is plotted in the inset.

IgM were denser in MZ B cells when compared to FO B cells, however the area/size of these nanoclusters were slightly smaller in MZ B cells (Figure 6.3D-E). This suggests that in MZ B cells, IgM BCRs exist in smaller but denser nanoclusters, when compared to FO B cells. Taken together, when compared to FO B cells, we show that there is a higher number of IgM oligomers, and nanoclusters are smaller but denser in MZ B cells.

6.3.2 IgD Nanoclusters are More Clustered in MZ B Cells

IgD is the predominant BCR isotype in mature naïve FO B cells, while IgD levels are low in MZ B cells. To assess the distribution of IgD on the B cell surface, B cells were stained with Fab fragments against IgD that were conjugated with AF647. As expected, the expression level of cell surface IgD is higher in MZ B cells when compared to FO B cells (Figure 6.4A, data provided by Libin Abraham, Gold lab). In STORM, we found that IgD BCRs predominantly existed as nanoclusters and few as oligomers in FO B cells. In addition, they showed a greater degree of clustering than IgM (with a Hopkins index median value of 0.825). In sharp contrast to IgM BCRs, IgD nanoclusters in MZ B cells showed a greater degree of clustering (median Hopkins index of 0.880), and had minimal oligomers, when compared to FO B cell (Figure 6.4B-D). Voronoi analyses revealed that the density of IgD nanoclusters were not changed in MZ B cells, when compared to FO B cells, and the area of nanoclusters were slightly larger in MZ B cells (Figure 6.4E-F). Though IgD exhibited more clustering in MZ B cells, the density and area of nanoclusters were not significantly altered.

6.3.3 MZ B Cells Have Higher Tonic Signaling Than FO B Cells

As described previously, antigen binding to BCR initiates BCR signaling, where the cytoplasmic domains of the CD79a-CD79b chains (the signaling subunit of the BCR complex) are phosphorylated by the Src family kinase, Lyn [129]. Such BCR signaling occurs in the absence of

antigen as well (referred to as tonic BCR signaling) and determines the activation status of a B cell. It is hypothesized that naïve mature FO B cells have low basal tonic BCR signaling, while MZ B cells (being partially activated or primed) have higher levels of tonic BCR signaling. However, this was never established experimentally. Here, for the first time, we investigated tonic BCR signaling in FO and MZ B cells using a phospho-CD79a specific antibody, which binds to all signaling BCRs. Of note, these signaling BCRs could be associated with either a cell surface BCR complex or a membrane proximal intracellular vesicle bearing the BCR complex. Since both BCR isotypes can signal via their CD79a/CD79b subunit, the antibody staining cannot distinguish the BCR isotype involved in BCR signaling.

Unlike IgM or IgD BCRs that exist as heterogeneous oligomers or nanoclusters, signaling BCRs in resting FO B cells were organized predominantly into discrete and well-defined nanoclusters, with minimal fraction in oligomers (Figure 6.5A). This suggests that signaling occurs in well-defined nanocluster 'hotspots or hubs' and the oligomers of BCRs (as seen in IgM or IgD) may not contribute to tonic BCR signaling. However, a large fraction of pCD79a signals in MZ B cells were found to exist as oligomers, suggesting that MZ B cells have more oligomeric forms of signaling BCRs (Figure 6.5B-C). This was quantified using the Hopkins index, where the extent of pCD79a clustering in MZ B cells was found to be significantly lower than FO B cell (Figure 6.5B-C).In addition, the density of the signaling BCRs were lower in MZ B cells, when compared to FO B cells; however the area of these nanoclusters remained unchained (Figure 6.5E-F).On the basis of these data, we report that signaling BCRs exist in well-defined nanoclusters in FO B cells, while they exist predominantly as less denser nanoclusters and dispersed oligomers in MZ B cells.

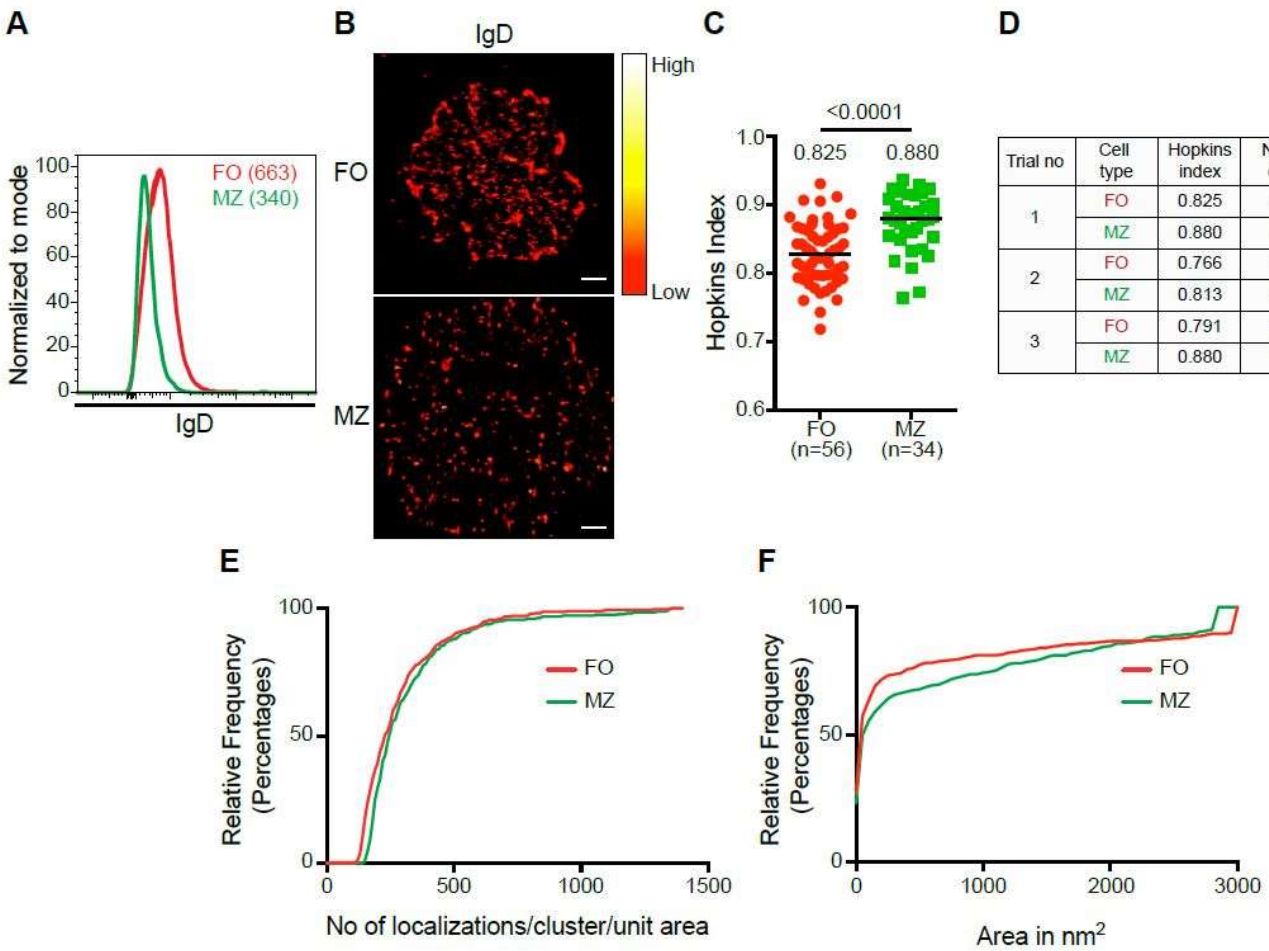

Trial no	Cell type	Hopkins index	No of cells	p-value
1	FO	0.825	56	<0.0001
	MZ	0.880	34	
2	FO	0.766	93	0.0089
	MZ	0.813	23	
3	FO	0.791	30	0.0001
	MZ	0.880	13	

Figure 6.4 - IgD is more clustered in MZ B cells when compared to FO B cells. (A) Flow cytometric analysis of cell surface IgD in FO and MZ B cell. **(B)** Representative STORM images reconstructed from single-molecule localizations of IgD in FO (*upper panel*) and MZ B cell (*lower panel*). Depicted is the density plot of localizations. Scale bar = 1µm. **(C-D)** Quantification of the extent of IgD clustering using Hopkins index. Black bars indicate median values. Cumulative frequency plots indicating relative frequency of normalized density **(E)** and area **(F)** of IgD nanoclusters in FO and MZ B cells.

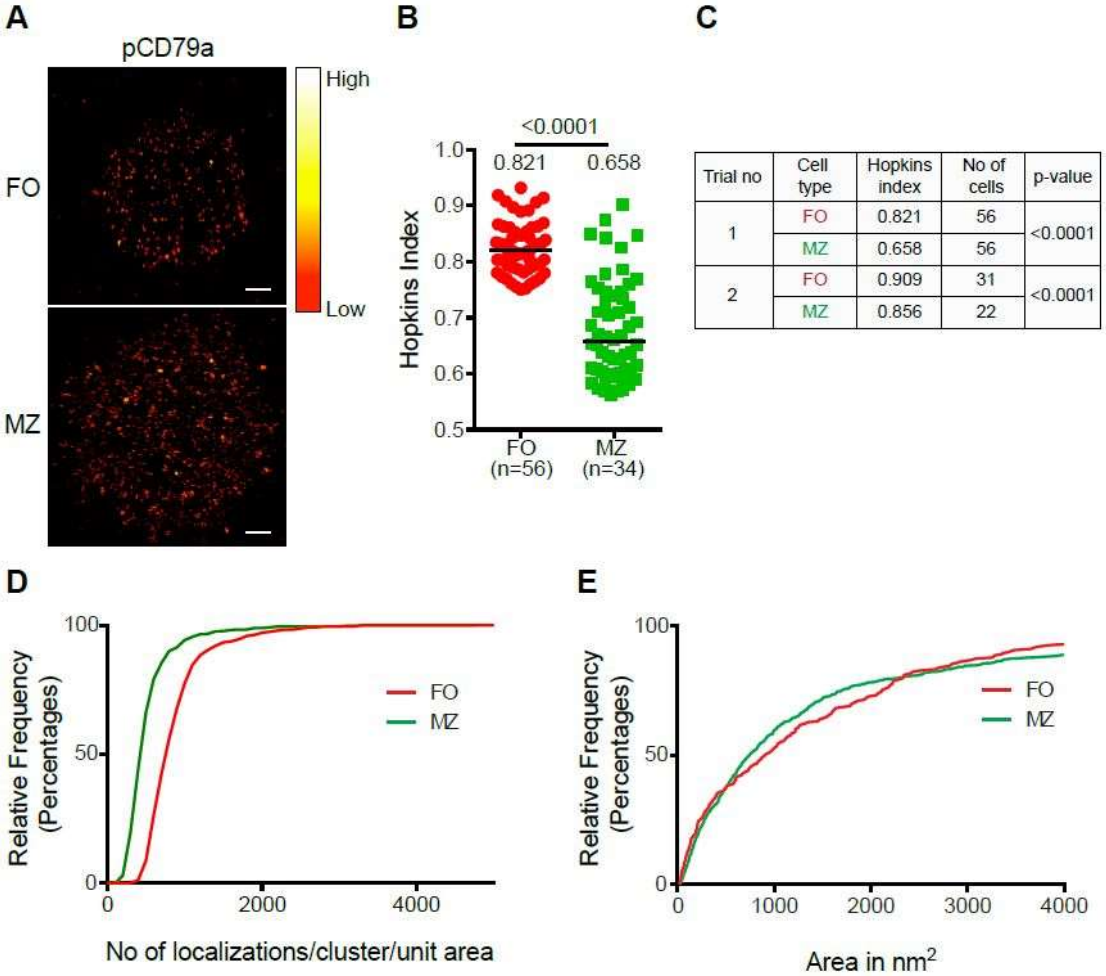

Trial no	Cell type	Hopkins index	No of cells	p-value
1	FO	0.821	56	<0.0001
	MZ	0.658	56	
2	FO	0.909	31	<0.0001
	MZ	0.856	22	

Figure 6.5 - MZ B cells have higher tonic signaling than FO B cells. (A) Representative STORM images reconstructed from single-molecule localizations of pCD79a in FO (*upper panel*) and MZ B cell (*lower panel*). Depicted is the density plot of localizations. Scale bar = 1 µm. **(B-C)** Quantification of the extent of pCD79a clustering using Hopkins index. Black bars indicate median values. Cumulative frequency plots indicating relative frequency of normalized density **(E)** and area **(F)** of pCD79a nanoclusters in FO and MZ B cells.

6.4 Discussion

The primary purpose of this study was to determine the organization of BCR isotypes (IgM and IgD), and signaling BCRs (pCD79a) in FO and MZ B cells using dSTORM. Here, we report that BCR isotypes, IgM and IgD exist in heterogeneous populations in B cell subsets, where both BCR isotypes exist in two major forms: nanoclusters and oligomers. We also visualized for the first time signaling BCRs (pCD79a) in FO and MZ B cells and found that tonic BCR signaling occurs only from well-defined nanoclusters in resting FO B cells. In MZ B cells, we saw an increase in signaling BCR fraction that exist as oligomers, suggesting that oligomers of BCRs also contribute to signaling in these primed B cells. The increase in pCD79a signals in MZ B cells provides the first direct evidence for higher tonic BCR signaling and the subsequent priming seen in MZ B cells.

Spatial organization of BCRs in relation to each other and with positive regulators (e.g. co-receptors such as CD19) and negative regulators (e.g. inhibitory receptors such as CD22) of BCR signaling, play an important role in regulating the thresholds for B cell activation [138, 161, 162]. In resting FO B cells, BCRs exist in nanoclusters and are thought to be associated with negative regulators in order to avoid spontaneous B cell activation. However, upon antigen engagement, receptor crosslinking initiates BCR signaling and subsequently, nanoclusters fuse to form larger microclusters, which can be visualized using a diffraction-limited microscope [163]. Such microclusters formed after antigen-induced BCR crosslinking are spatially segregated in such a way that they exist in close proximity with co-receptors and are excluded from phosphatases (that dephosphorylate signaling BCRs). This acts to enhance the strength of BCR signaling and subsequent B cell activation. However, the organization of BCRs in partially activated/primed B cells is largely unknown. In addition, there is also no evidence pertaining to antigen-independent

tonic BCR signaling in resting and primed B cells. Since MZ B cells are naturally primed (by mechanisms largely unknown), we used this rare population of B cells (compared with resting FO B cells) as a tool to understand this proposed state at a molecular level.

Since the size of BCR nanoclusters are below the diffraction limit of light, we used dSTORM to ascertain the organization of BCRs on the cell surface. Of note, the drift-free long-term imaging system gave us a plethora of advantages over other commercial dSTORM systems (which are prone to sample drift). More specifically, this custom dSTORM system conferred the following benefits: (1) it possesses the unique capability of detecting heterogeneous populations of receptors, ranging from oligomers to dense nanoclusters, (2) with its ability to accumulate a sufficiently large number of single molecule localizations, meaningful and correct image reconstructions with high accuracies can be achieved, and (3) it has the capacity to perform multi-color imaging without compromising on the number of localizations in the weak fluorophore channel (Cy3B or the green channel in our case). Taken together, the super resolution images of BCRs and signaling BCRs we obtained are by far superior to any similar super-resolution studies done on B cells. In addition to a 'cutting-edge' image stabilization system, we used novel clustering methods to quantify the reconstructions of BCRs [159, 160]. We discovered that both IgM and IgD isotypes existed as highly heterogeneous nanoclusters. This is consistent with the observation that most membrane receptors organize predominantly as nanoclusters [164]. Most importantly, the spatial organization of BCR isotypes and signaling BCRs showed striking differences in their organization between FO and MZ B cells.

Though heightened tonic signaling in MZ B cells was demonstrated using flow cytometry (unpublished data from Libin Abraham, Gold lab), spatial information about signaling active BCRs was not available. By using a phospho-CD79a specific antibody, we directly assessed the

organization of signaling active BCRs in these two cell types. Though oligomers of BCRs exist on the resting B cell surface, we found only a negligible fraction of signaling BCRs that existed as oligomers. This suggests that tonic BCR signaling occurs in well-defined nanoclusters, which act as 'signaling hubs' for localized tonic BCR signaling and free oligomers do not contribute to BCR signaling.

From here, the next steps to take would be to examine whether higher tonic BCR signals seen in MZ B cells is mediated by either its association with activatory co-receptors (positive regulators) or exclusion from inhibitory phosphatases (negative regulators), using 2 color STORM. It has been shown that CD19 amplifies BCR signaling after antigen engagement and colocalizes with BCR microclusters [161]. Whether similar mechanisms operate at the nanoscale levels in mediating antigen-independent tonic signaling is yet to be determined. Since we did not find change in BCR nanocluster area (size), we assume that nanocluster concatenation into larger clusters (as illustrated in Figure 6.2) may not be the underlying mechanism of tonic BCR signaling in MZ B cells. Instead, the intermixing of small, but dense BCR nanoclusters with positive regulators of BCR signaling could contribute to enhanced BCR signaling. In addition, recently, CD22 - a key negative regulator of BCR signaling, was shown to exist in dense nanoclusters and transiently interacts with BCRs in resting B cells [162]. In order to address the effect of co-receptors on signaling, the experimental approach would be to perform multi-color super-resolution imaging of BCRs, co-receptors, and signaling BCRs, and to quantify the degree of overlap between these various types of nanoclusters between two B cell types.

In addition, it would be useful to determine the spatial organization of BCR isotypes, co-receptors, and pCD79a nanoclusters, after stimulating B cells with bacterial lipopolysaccharide (LPS) or CpG DNA. These treatments activate B cells and mimic a primed state in a laboratory

setting. Recent studies from the Gold lab [154] have shown that such treatments increase actin remodeling, however the organization of BCRs and other co-receptors is still unknown. Cortical actin plays a central role in altering the mobility of BCRs and co-receptors [143, 144]. This was tested using pharmacological methods that disrupt actin barriers, and resulted in an increase in antigen-independent tonic BCR signaling [139]. Surprisingly, these treatments did not alter the size or density of BCR nanoclusters [144]. They proposed that actin disruption increases tonic BCR signaling by facilitating more receptor-corrector intermixing, instead of altering the nanocluster morphology of BCRs/co-receptors. Physiological actin remodeling in primed cells that acts to increase BCR mobility is different from actin perturbation using pharmacological agents. Hence, it is of particular interest to investigate the organization of different components involved in BCR signaling, in a more biological setting. In short, the study provided a detailed characterization of the molecular organization of BCR isotypes and signaling BCRs in resting FO B cells and primed MZ B cells.

Chapter 7: Conclusion

We presented two optical designs for real-time 3D drift correction of a super-resolution microscope. By extending the depth of field of the objective lens and decoupling the focal planes of the sample and the fiducial markers, it enabled drift-free super-resolution imaging at any depth. The instability of the microscope stage was shown to be reduced to ~1 nm in the lateral direction and ~3 nm in the axial direction. These stabilization systems are simple, inexpensive and compact and can be readily integrated into both commercial and custom-made super-resolution imaging systems. Imaging experiments, which require long-term data acquisition are generally susceptible to setup instability, but this can be greatly ameliorated by the technique presented in this study.

One of the optical designs for 3D super-resolution imaging, which was based on a simple movable lens in the bead-tracking path, was used to image type-2 Ryanodine receptor (RYR2) in the cardiac myocyte at a depth of several microns. This design helped resolve issues associated with deep imaging of thick cells using 3D SMLM. Localization errors due to the refractive index mismatch were removed by empirical measurements, which also provided corrections for the imperfection of the optics. Additionally, we showed that the spatial filter commonly used in reconstructing a super-resolution image may not eliminate artefacts that arise from structures with densely packed fluorophores. A time-domain filter was described that significantly reduced these artefacts.

Another optical design using an ETL in the bead-tracking path, was used to study the organization of transferrin receptors deep within B cells. The impact of stability on super-resolution images was demonstrated by imaging transferrin receptors in B cells at a depth of 8 μm. The drift-free super-resolution image depicts the transferrin receptors as distinct and heterogeneous clusters with a high circularity index and a bimodal size distribution. Additionally,

the average density of fluorophores per unit area in these clusters was two times higher than that in the drifted image.

We have used these super-resolution imaging approaches to examine overlap between the RYR2 and the L-type Calcium channel (Cav1.2) on the cellular surface and within the rat ventricular myocyte. We accurately imaged receptors down to a depth of 6 µm below the surface. For the first time, using light microscopy, we were able to image individual receptors and confirm Asghari *et al.* (2014) findings that these receptors in a cell at rest were not organized in a checkerboard, but rather, had a variety of cluster arrangements. RyR2 had markedly different distributions depending on where it was measured: the surface, just below it (250-500nm) or deep within the cell. This is consistent with previously reported results by Scriven *et al.* [122] that the surface and interior of the myocyte have different molecular architectures.

On the surface, the mean edge-to-edge difference was about 175 nm, while just below the surface - a transitional region, there are two types of clusters: circular and longitudinal. The circular clusters are quite isolated, with an edge-to-edge distance of 1.25 µm, while the longitudinal clusters have a mean edge-to-edge nearest neighbour distance (NND) of 374 nm. Phosphorylation of the cell seems to increase the size of the tetramer clusters. Network analysis has confirmed this. Like RyR2, clusters of $Ca_v1.2$ on the myocyte surface are significantly different from those in the cell's interior. In all locations, $Ca_v1.2$ clusters are significantly smaller than RyR2 clusters. This is consistent with previously reported results by Scriven *et al.* [115]. If one assumes a 10 nm radius for $Ca_v1.2$, then each cluster could contain as many as 8 channels, probably as a collection of dimers. This estimate ignores the size of the antibodies and the real value is potentially much less.

We validated two-color mapping by labelling RyR2 with both Cy3B and Alexa 647 and then measuring the overlap between the two images. The majority (> 95%) of the RyR2 clusters had

some overlap with $Ca_v1.2$, indicating that large extra-dyadic clusters are infrequent. The distribution of RyR2 and $Ca_v1.2$ parallel each other and vary greatly between the surface, just below it and deep in the interior. This is consistent with the view that the surface and interior of the myocyte have different molecular architectures. Colocalization in the classical sense has little meaning at this high of a resolution, since the degree of overlap varies from 15-85% depending on the cluster examined. In addition, some of the $Ca_v1.2$ is next to, or partly overlapping with the RyR2s at a distance close enough to exert an effect. Similarly, the RyR2 cluster sizes are extremely variable ranging from two to over 200 tetramers. These findings indicate that there is no 'average' or 'typical' couplon.

We have also used these super-resolution imaging approaches to examine the organization of BCRs on the cell surface. Of note, the drift-free long-term imaging system gave us a plethora of advantages over other commercial dSTORM systems (which are prone to sample drift). More specifically, this custom dSTORM system conferred the following benefits: (1) it possesses the unique capability of detecting heterogeneous populations of receptors, ranging from oligomers to dense nanoclusters, (2) with its ability to accumulate a sufficiently large number of single molecule localizations, meaningful and correct image reconstructions with high accuracies can be achieved, and (3) it has the capacity to perform multi-color imaging without compromising on the number of localizations in the weak fluorophore channel (Cy3B or the green channel in our case).

Taken together, the super resolution images of BCRs and signaling BCRs we obtained are by far superior to any similar super-resolution studies done on B cells. In addition to a 'cutting-edge' image stabilization system, we used novel clustering methods to quantify the reconstructions of BCRs [159, 160]. We discovered that both IgM and IgD isotypes existed as highly heterogeneous nanoclusters. This is consistent with the observation that most membrane receptors organize

predominantly as nanoclusters [164]. Most importantly, the spatial organization of BCR isotypes and signaling BCRs showed striking differences in their organization between FO and MZ B cells.

Bibliography

1. G. T. Dempsey, J. C. Vaughan, K. H. Chen, M. Bates, and X. Zhuang, "Evaluation of fluorophores for optimal performance in localization-based super-resolution imaging," Nat. Methods **8**, 1027-1036 (2011).
2. H. Volkmann, "Ernst Abbe and His Work," Appl. Opt. **5**, 1720 (1966).
3. L. Rayleigh, "XV. On the theory of optical images, with special reference to the microscope," Philosophical Magazine Series 5 **42**, 167-195 (1896).
4. C. Cremer and B. R. Masters, "Resolution enhancement techniques in microscopy," EPJ H **38**, 281-344 (2013).
5. J. Bechhoefer, "What is superresolution microscopy?," arXiv:1405.1118 [physics] (2014).
6. C. W. McCutchen, "Superresolution in Microscopy and the Abbe Resolution Limit," J. Opt. Soc. Am. **57**, 1190 (1967).
7. A. Yildiz, J. N. Forkey, S. A. McKinney, T. Ha, Y. E. Goldman, and P. R. Selvin, "Myosin V walks hand-over-hand: single fluorophore imaging with 1.5-nm localization," Science (New York, N.Y.) **300**, 2061-2065 (2003).
8. A. Yildiz, M. Tomishige, R. D. Vale, and P. R. Selvin, "Kinesin walks hand-over-hand," Science (New York, N.Y.) **303**, 676-678 (2004).
9. E. Betzig, G. H. Patterson, R. Sougrat, O. W. Lindwasser, S. Olenych, J. S. Bonifacino, M. W. Davidson, J. Lippincott-Schwartz, and H. F. Hess, "Imaging Intracellular Fluorescent Proteins at Nanometer Resolution," Science **313**, 1642-1645 (2006).
10. M. J. Rust, M. Bates, and X. Zhuang, "Sub-diffraction-limit imaging by stochastic optical reconstruction microscopy (STORM)," Nat. Methods **3**, 793-796 (2006).
11. G. Giannone, E. Hosy, F. Levet, A. Constals, K. Schulze, A. I. Sobolevsky, M. P. Rosconi, E. Gouaux, R. Tampé, D. Choquet, and L. Cognet, "Dynamic superresolution imaging of endogenous proteins on living cells at ultra-high density," Biophys. J. **99**, 1303-1310 (2010).
12. S. v. d. Linde, A. Löschberger, T. Klein, M. Heidbreder, S. Wolter, M. Heilemann, and M. Sauer, "Direct stochastic optical reconstruction microscopy with standard fluorescent probes," Nat. Protoc. **6**, 991-1009 (2011).
13. M. Born and E. Wolf, *Principles of Optics: Electromagnetic Theory of Propagation, Interference and Diffraction of Light* (Cambridge University Press, 1997).
14. B. Huang, M. Bates, and X. Zhuang, "Super-Resolution Fluorescence Microscopy," Annu. Rev. Biochem. **78**, 993-1016 (2009).
15. E. Abbe, "Beiträge zur Theorie des Mikroskops und der mikroskopischen Wahrnehmung," Arch. Mikrosk. Anat., 413–487 (1873).
16. P. P. Mondal and A. Diaspro, *Fundamentals of Fluorescence Microscopy* (Springer Netherlands, Dordrecht, 2014).
17. M. Heilemann, S. van de Linde, A. Mukherjee, and M. Sauer, "Super-Resolution Imaging with Small Organic Fluorophores," Angew. Chem. Int. Ed. **48**, 6903-6908 (2009).
18. M. Heilemann, S. van de Linde, M. Schüttpelz, R. Kasper, B. Seefeldt, A. Mukherjee, P. Tinnefeld, and M. Sauer, "Subdiffraction-Resolution Fluorescence Imaging with Conventional Fluorescent Probes," Angew. Chem. Int. Ed. **47**, 6172-6176 (2008).
19. S. W. Hell, "Far-Field Optical Nanoscopy," Science **316**, 1153-1158 (2007).

20. S. W. Hell and J. Wichmann, "Breaking the diffraction resolution limit by stimulated emission: stimulated-emission-depletion fluorescence microscopy," Opt. Lett. **19**, 780-782 (1994).
21. M. Heilemann, "Fluorescence microscopy beyond the diffraction limit," J. Biotechnol. **149**, 243-251 (2010).
22. S. W. Hell, "Microscopy and its focal switch," Nat. Methods **6**, 24-32 (2009).
23. Shannon and CE., "Communication in the presence of noise," Proc. Inst. Radio Eng **37**, 10–21 (1949).
24. H. Shroff, C. G. Galbraith, J. A. Galbraith, and E. Betzig, "Live-cell photoactivated localization microscopy of nanoscale adhesion dynamics," Nat. Methods **5**, 417-423 (2008).
25. T. Cordes, M. Strackharn, S. W. Stahl, W. Summerer, C. Steinhauer, C. Forthmann, E. M. Puchner, J. Vogelsang, H. E. Gaub, and P. Tinnefeld, "Resolving Single-Molecule Assembled Patterns with Superresolution Blink-Microscopy," Nano Lett. **10**, 645-651 (2010).
26. S. van de Linde, S. Wolter, M. Heilemann, and M. Sauer, "The effect of photoswitching kinetics and labeling densities on super-resolution fluorescence imaging," J. Biotechnol. **149**, 260-266 (2010).
27. T. Klein, A. Löschberger, S. Proppert, S. Wolter, S. van de Linde, and M. Sauer, "Live-cell dSTORM with SNAP-tag fusion proteins," Nat. Methods **8**, 7-9 (2011).
28. R. Wombacher, M. Heidbreder, S. van de Linde, M. P. Sheetz, M. Heilemann, V. W. Cornish, and M. Sauer, "Live-cell super-resolution imaging with trimethoprim conjugates," Nat. Methods **7**, 717-719 (2010).
29. S. van de Linde, A. Löschberger, T. Klein, M. Heidbreder, S. Wolter, M. Heilemann, and M. Sauer, "Direct stochastic optical reconstruction microscopy with standard fluorescent probes," Nat. Protoc. **6**, 991-1009 (2011).
30. J. R. Allen, S. T. Ross, and M. W. Davidson, "Single molecule localization microscopy for superresolution," J. Opt. **15**, 094001 (2013).
31. M. H. Horrocks, M. Palayret, D. Klenerman, and S. F. Lee, "The changing point-spread function: single-molecule-based super-resolution imaging," Histochem. Cell Biol. **141**, 577-585 (2014).
32. T. A. Klar and S. W. Hell, "Subdiffraction resolution in far-field fluorescence microscopy," Opt. Lett. **24**(1999).
33. S. W. Hell, M. Dyba, and S. Jakobs, "Concepts for nanoscale resolution in fluorescence microscopy," Curr. Opin. Neurobiol. **14**, 599-609 (2004).
34. J. B. Ding, K. T. Takasaki, and B. L. Sabatini, "Supraresolution Imaging in Brain Slices using Stimulated-Emission Depletion Two-Photon Laser Scanning Microscopy," Neuron **63**, 429-437 (2009).
35. C. Eggeling, C. Ringemann, R. Medda, G. Schwarzmann, K. Sandhoff, S. Polyakova, V. N. Belov, B. Hein, C. von Middendorff, A. Schönle, and S. W. Hell, "Direct observation of the nanoscale dynamics of membrane lipids in a living cell," Nature **457**, 1159-1162 (2009).
36. U. V. Nägerl, K. I. Willig, B. Hein, S. W. Hell, and T. Bonhoeffer, "Live-cell imaging of dendritic spines by STED microscopy," PNAS **105**, 18982-18987 (2008).

37. V. Westphal, S. O. Rizzoli, M. A. Lauterbach, D. Kamin, R. Jahn, and S. W. Hell, "Video-Rate Far-Field Optical Nanoscopy Dissects Synaptic Vesicle Movement," Science **320**, 246-249 (2008).
38. U. Kubitscheck, O. Kückmann, T. Kues, and R. Peters, "Imaging and Tracking of Single GFP Molecules in Solution," Biophys. J. **78**, 2170-2179 (2000).
39. R. E. Thompson, D. R. Larson, and W. W. Webb, "Precise nanometer localization analysis for individual fluorescent probes," Biophys. J. **82**, 2775-2783 (2002).
40. M. K. Cheezum, W. F. Walker, and W. H. Guilford, "Quantitative comparison of algorithms for tracking single fluorescent particles," Biophys. J. **81**, 2378-2388 (2001).
41. R. J. Ober, S. Ram, and E. S. Ward, "Localization Accuracy in Single-Molecule Microscopy," Biophys. J. **86**, 1185-1200 (2004).
42. F. Huang, T. M. P. Hartwich, F. E. Rivera-Molina, Y. Lin, W. C. Duim, J. J. Long, P. D. Uchil, J. R. Myers, M. A. Baird, W. Mothes, M. W. Davidson, D. Toomre, and J. Bewersdorf, "Video-rate nanoscopy using sCMOS camera-specific single-molecule localization algorithms," Nat. Methods **10**, 653-658 (2013).
43. S. Kay, *Fundamentals of Statistical Signal Processing, Volume I: Estimation Theory,* 1 edition ed. (Prentice Hall, Englewood Cliffs, N.J, 1993), p. 625.
44. K. I. Mortensen, L. S. Churchman, J. A. Spudich, and H. Flyvbjerg, "Optimized localization analysis for single-molecule tracking and super-resolution microscopy," Nat. Methods **7**, 377-381 (2010).
45. H. Deschout, F. C. Zanacchi, M. Mlodzianoski, A. Diaspro, J. Bewersdorf, S. T. Hess, and K. Braeckmans, "Precisely and accurately localizing single emitters in fluorescence microscopy," Nat. Methods **11**, 253-266 (2014).
46. A. Small and S. Stahlheber, "Fluorophore localization algorithms for super-resolution microscopy," Nat. Methods **11**, 267-279 (2014).
47. J. Chao, S. Ram, E. S. Ward, and R. J. Ober, "Ultrahigh accuracy imaging modality for super-localization microscopy," Nat. Methods **10**, 335-338 (2013).
48. W. Wang, "Structures and Dynamics in Live Bacteria Revealed by Super-Resolution Fluorescence Microscopy," (2012).
49. R. Hain, C. J. Kähler, and C. Tropea, "Comparison of CCD, CMOS and intensified cameras," Exp. Fluids **42**, 403-411 (2007).
50. M. J. Mlodzianoski, J. M. Schreiner, S. P. Callahan, K. Smolková, A. Dlasková, J. Santorová, P. Ježek, and J. Bewersdorf, "Sample drift correction in 3D fluorescence photoactivation localization microscopy," Opt. Express **19**, 15009-15019 (2011).
51. A. Pertsinidis, Y. Zhang, and S. Chu, "Subnanometre single-molecule localization, registration and distance measurements," Nature **466**, 647-651 (2010).
52. S. H. Lee, M. Baday, M. Tjioe, P. D. Simonson, R. Zhang, E. Cai, and P. R. Selvin, "Using fixed fiduciary markers for stage drift correction," Opt. Express **20**, 12177-12183 (2012).
53. R. McGorty, D. Kamiyama, and B. Huang, "Active microscope stabilization in three dimensions using image correlation," in *Opt. Nanoscopy,* (2013).
54. C. Geisler, T. Hotz, A. Schönle, S. W. Hell, A. Munk, and A. Egner, "Drift estimation for single marker switching based imaging schemes," Opt. Express **20**(2012).
55. K. Weber, P. C. Rathke, and M. Osborn, "Cytoplasmic microtubular images in glutaraldehyde-fixed tissue culture cells by electron microscopy and by immunofluorescence microscopy," Proc. Natl. Acad. Sci. U.S.A. **75**, 1820-1824 (1978).

56. M. Bates, B. Huang, G. T. Dempsey, and X. Zhuang, "Multicolor super-resolution imaging with photo-switchable fluorescent probes," Science (New York, N.Y.) **317**, 1749-1753 (2007).
57. P. N. Hedde, J. Fuchs, F. Oswald, J. Wiedenmann, and G. U. Nienhaus, "Online image analysis software for photoactivation localization microscopy," Nat. Methods **6**, 689-690 (2009).
58. R. Henriques, M. Lelek, E. F. Fornasiero, F. Valtorta, C. Zimmer, and M. M. Mhlanga, "QuickPALM: 3D real-time photoactivation nanoscopy image processing in ImageJ," Nat Meth **7**, 339-340 (2010).
59. U. Köthe, F. Herrmannsdörfer, I. Kats, and F. A. Hamprecht, "SimpleSTORM: a fast, self-calibrating reconstruction algorithm for localization microscopy," Histochem. Cell Biol. **141**, 613-627 (2014).
60. M. Ovesný, P. Křížek, J. Borkovec, Z. Švindrych, and G. M. Hagen, "ThunderSTORM: a comprehensive ImageJ plug-in for PALM and STORM data analysis and super-resolution imaging," Bioinformatics, btu202 (2014).
61. A. V. Abraham, S. Ram, J. Chao, E. S. Ward, and R. J. Ober, "Quantitative study of single molecule location estimation techniques," Opt. Express **17**, 23352 (2009).
62. B. Richards and E. Wolf, "Electromagnetic Diffraction in Optical Systems. II. Structure of the Image Field in an Aplanatic System," Proceedings of the Royal Society of London A: Mathematical, Physical and Engineering Sciences **253**, 358-379 (1959).
63. S. F. Gibson and F. Lanni, "Experimental test of an analytical model of aberration in an oil-immersion objective lens used in three-dimensional light microscopy," Journal of the Optical Society of America A **9**, 154 (1992).
64. F. Aguet, "Super-resolution fluorescence microscopy based on physical models," (2009).
65. A. R. Carter, G. M. King, T. A. Ulrich, W. Halsey, D. Alchenberger, and T. T. Perkins, "Stabilization of an optical microscope to 0.1 nm in three dimensions," Appl. Opt. **46**, 421-427 (2007).
66. V. Mennella, B. Keszthelyi, K. L. McDonald, B. Chhun, F. Kan, G. C. Rogers, B. Huang, and D. A. Agard, "Subdiffraction-resolution fluorescence microscopy reveals a domain of the centrosome critical for pericentriolar material organization," Nat. Cell Biol. **14**, 1159-1168 (2012).
67. R. McGorty, J. Schnitzbauer, W. Zhang, and B. Huang, "Correction of depth-dependent aberrations in 3D single-molecule localization and super-resolution microscopy," Opt. Lett. **39**, 275-278 (2014).
68. B. Huang, S. A. Jones, B. Brandenburg, and X. Zhuang, "Whole-cell 3D STORM reveals interactions between cellular structures with nanometer-scale resolution," Nat. Meth. **5**, 1047-1052 (2008).
69. B. Huang, W. Wang, M. Bates, and X. Zhuang, "Three-Dimensional Super-Resolution Imaging by Stochastic Optical Reconstruction Microscopy," Science **319**, 810-813 (2008).
70. F. Huang, S. L. Schwartz, J. M. Byars, and K. A. Lidke, "Simultaneous multiple-emitter fitting for single molecule super-resolution imaging," Biomed. Opt. Express **2**, 1377-1393 (2011).
71. Y. Chen-Izu, S. L. McCulle, C. W. Ward, C. Soeller, B. M. Allen, C. Rabang, M. B. Cannell, C. W. Balke, and L. T. Izu, "Three-Dimensional Distribution of Ryanodine Receptor Clusters in Cardiac Myocytes," Biophys. J. **91**, 1-13 (2006).

72. S. Hell, G. Reiner, C. Cremer, and E. H. K. Stelzer, "Aberrations in Confocal Fluorescence Microscopy Induced by Mismatches in Refractive-Index," J. Microsc. **169**, 391-405 (1993).
73. M. N. Schulson, D. R. Scriven, P. Fletcher, and E. D. Moore, "Couplons in rat atria form distinct subgroups defined by their molecular partners," J. Cell Sci. **124**, 1167-1174 (2011).
74. B. Rodrigues and D. L. Severson, "Preparation of cardiomyocytes," in *Biochemical Techniques in the Heart* (CRC Press, Boca Raton, FL, USA, 1997), pp. 101–115.
75. R. Henriques, M. Lelek, E. F. Fornasiero, F. Valtorta, C. Zimmer, and M. M. Mhlanga, "QuickPALM: 3D real-time photoactivation nanoscopy image processing in ImageJ," Nat. Meth. **7**, 339-340 (2010).
76. S. Wolter, A. Löschberger, T. Holm, S. Aufmkolk, M.-C. Dabauvalle, S. van de Linde, and M. Sauer, "rapidSTORM: accurate, fast open-source software for localization microscopy," Nat. Meth. **9**, 1040-1041 (2012).
77. S. A. Jones, S.-H. Shim, J. He, and X. Zhuang, "Fast, three-dimensional super-resolution imaging of live cells," Nat. Meth. **8**, 499-505 (2011).
78. H. Babcock, Y. M. Sigal, and X. Zhuang, "A high-density 3D localization algorithm for stochastic optical reconstruction microscopy," in *Opt. Nanoscopy,* (2012).
79. S. Cox, E. Rosten, J. Monypenny, T. Jovanovic-Talisman, D. T. Burnette, J. Lippincott-Schwartz, G. E. Jones, and R. Heintzmann, "Bayesian localization microscopy reveals nanoscale podosome dynamics," Nat. Meth. **9**, 195-200 (2012).
80. S. J. Holden, S. Uphoff, and A. N. Kapanidis, "DAOSTORM: an algorithm for high-density super-resolution microscopy," Nat. Meth. **8**, 279-280 (2011).
81. A. Barsic, G. Grover, and R. Piestun, "Three-dimensional super-resolution and localization of dense clusters of single molecules," Sci. Rep. **4**(2014).
82. L. Zhu, W. Zhang, D. Elnatan, and B. Huang, "Faster STORM using compressed sensing," Nat. Meth. **9**, 721-723 (2012).
83. M. Radermacher, V. Rao, R. Grassucci, J. Frank, A. P. Timerman, S. Fleischer, and T. Wagenknecht, "Cryo-electron microscopy and three-dimensional reconstruction of the calcium release channel/ryanodine receptor from skeletal muscle," J. Cell Biol. **127**, 411-423 (1994).
84. P. Asghari, D. R. L. Scriven, S. Sanatani, S. K. Gandhi, A. I. M. Campbell, and E. D. W. Moore, "Nonuniform and Variable Arrangements of Ryanodine Receptors Within Mammalian Ventricular Couplons," Circ. Res. **115**, 252-262 (2014).
85. R. Tafteh, D. R. L. Scriven, E. D. W. Moore, and K. C. Chou, "Single molecule localization deep within thick cells; a novel super-resolution microscope," J. Biophoton **9**, 155-160 (2016).
86. G. Beadie, M. L. Sandrock, M. J. Wiggins, R. S. Lepkowicz, J. S. Shirk, M. Ponting, Y. Yang, T. Kazmierczak, A. Hiltner, and E. Baer, "Tunable polymer lens," Opt. Express **16**, 11847-11857 (2008).
87. H. Ren, H. Xianyu, S. Xu, and S.-T. Wu, "Adaptive dielectric liquid lens," Opt. Express **16**, 14954 (2008).
88. O. Pishnyak, S. Sato, and O. D. Lavrentovich, "Electrically tunable lens based on a dual-frequency nematic liquid crystal," Appl. Opt. **45**, 4576 (2006).
89. S. Kuiper, B. H. Hendriks, L. J. Huijbregts, A. M. Hirschberg, C. A. Renders, and M. A. van As, "Variable-focus liquid lens for portable applications," in 2004), 100-109.

90. S. A. Freeman, V. Jaumouillé, K. Choi, B. E. Hsu, H. S. Wong, L. Abraham, M. L. Graves, D. Coombs, C. D. Roskelley, R. Das, S. Grinstein, and M. R. Gold, "Toll-like receptor ligands sensitize B-cell receptor signalling by reducing actin-dependent spatial confinement of the receptor," Nat Commun **6**, 6168 (2015).
91. J. Futran, J. D. Kemp, E. H. Field, A. Vora, and R. F. Ashman, "Transferrin receptor synthesis is an early event in B cell activation," Journal of Immunology (Baltimore, Md.: 1950) **143**, 787-792 (1989).
92. L. M. Neckers, G. Yenokida, and S. P. James, "The role of the transferrin receptor in human B lymphocyte activation," Journal of Immunology (Baltimore, Md.: 1950) **133**, 2437-2441 (1984).
93. G. Eberle, V. Chiron, and K. Wegener, "Simulation and Realization of a Focus Shifting Unit using a Tunable Lens for 3D Laser Material Processing," Physics Procedia **41**, 441-447 (2013).
94. I. Izeddin, M. El Beheiry, J. Andilla, D. Ciepielewski, X. Darzacq, and M. Dahan, "PSF shaping using adaptive optics for three-dimensional single-molecule super-resolution imaging and tracking," Opt. Express **20**, 4957 (2012).
95. N. Piro, T. Pengo, N. Olivier, and S. Manley, "Improved 3D Superresolution Localization Microscopy Using Adaptive Optics," arXiv:1401.0879 [physics] (2014).
96. F. O. Fahrbach, F. F. Voigt, B. Schmid, F. Helmchen, and J. Huisken, "Rapid 3D light-sheet microscopy with a tunable lens," Opt. Express **21**, 21010 (2013).
97. I. Moreno, C. Ferreira, and M. M. Sánchez-López, "Ray matrix analysis of anamorphic fractional Fourier systems," J. Opt. A: Pure Appl. Opt. **8**, 427 (2006).
98. T. Szoplik, W. Kosek, and C. Ferreira, "Nonsymmetric Fourier transforming with an anamorphic system," Appl. Opt. **23**, 905 (1984).
99. P. Ponka and C. N. Lok, "The transferrin receptor: role in health and disease," The International Journal of Biochemistry & Cell Biology **31**, 1111-1137 (1999).
100. H. Kobayashi and M. Fukuda, "Arf6, Rab11 and transferrin receptor define distinct populations of recycling endosomes," Commun. Integr. Biol. **6**, e25036 (2013).
101. R. S. Ajioka and J. Kaplan, "Intracellular pools of transferrin receptors result from constitutive internalization of unoccupied receptors," Proc. Natl. Acad. Sci. U.S.A. **83**, 6445-6449 (1986).
102. E. M. v. Dam, T. t. Broeke, K. Jansen, P. Spijkers, and W. Stoorvogel, "Endocytosed Transferrin Receptors Recycle via Distinct Dynamin and Phosphatidylinositol 3-Kinase-dependent Pathways," J. Biol. Chem. **277**, 48876-48883 (2002).
103. F. Levet, E. Hosy, A. Kechkar, C. Butler, A. Beghin, D. Choquet, and J.-B. Sibarita, "SR-Tesseler: a method to segment and quantify localization-based super-resolution microscopy data," Nat. Methods **12**, 1065-1071 (2015).
104. D. Baddeley, "Detecting nano-scale protein clustering," Nat. Methods **12**, 1019-1020 (2015).
105. C. Harding, J. Heuser, and P. Stahl, "Receptor-mediated endocytosis of transferrin and recycling of the transferrin receptor in rat reticulocytes," The Journal of Cell Biology **97**, 329-339 (1983).
106. C. R. Hopkins, "Intracellular routing of transferrin and transferrin receptors in epidermoid carcinoma A431 cells," Cell **35**, 321-330 (1983).

107. B. T. Pan, K. Teng, C. Wu, M. Adam, and R. M. Johnstone, "Electron microscopic evidence for externalization of the transferrin receptor in vesicular form in sheep reticulocytes," The Journal of Cell Biology **101**, 942-948 (1985).
108. L. Sallé and F. Brette, "T-tubules: a key structure of cardiac function and dysfunction," Arch. Mal. Coeur Vaiss. **100**, 225-230 (2007).
109. A. Fabiato, "Calcium-induced release of calcium from the cardiac sarcoplasmic reticulum," The American journal of physiology **245**, C1-14 (1983).
110. D. R. L. Scriven, P. Asghari, and E. D. W. Moore, "Microarchitecture of the dyad," Cardiovasc. Res. **98**, 169-176 (2013).
111. P. Asghari, D. R. L. Scriven, J. Hoskins, N. Fameli, C. v. Breemen, and E. D. W. Moore, "The structure and functioning of the couplon in the mammalian cardiomyocyte," Protoplasma **249**, 31-38 (2011).
112. P. Asghari, D. R. L. Scriven, S. Sanatani, S. K. Gandhi, A. I. M. Campbell, and E. D. W. Moore, "Nonuniform and variable arrangements of ryanodine receptors within mammalian ventricular couplons," Circul. Res. **115**, 252-262 (2014).
113. T. Hayashi, M. E. Martone, Z. Yu, A. Thor, M. Doi, M. J. Holst, M. H. Ellisman, and M. Hoshijima, "Three-dimensional electron microscopy reveals new details of membrane systems for Ca2+ signaling in the heart," J. Cell Sci. **122**, 1005-1013 (2009).
114. D. Baddeley, I. D. Jayasinghe, L. Lam, S. Rossberger, M. B. Cannell, and C. Soeller, "Optical single-channel resolution imaging of the ryanodine receptor distribution in rat cardiac myocytes," PNAS **106**, 22275-22280 (2009).
115. D. R. L. Scriven, P. Asghari, M. N. Schulson, and E. D. W. Moore, "Analysis of Cav1.2 and Ryanodine Receptor Clusters in Rat Ventricular Myocytes," Biophys. J. **99**, 3923-3929 (2010).
116. P. Annibale, M. Scarselli, M. Greco, and A. Radenovic, "Identification of the factors affecting co-localization precision for quantitative multicolor localization microscopy," Optical Nanoscopy **1**, 9 (2012).
117. L. S. Churchman, Z. Okten, R. S. Rock, J. F. Dawson, and J. A. Spudich, "Single molecule high-resolution colocalization of Cy3 and Cy5 attached to macromolecules measures intramolecular distances through time," Proc. Natl. Acad. Sci. U.S.A. **102**, 1419-1423 (2005).
118. A. Goshtasby, "Registration of images with geometric distortions," IEEE Transactions on Geoscience and Remote Sensing **26**, 60-64 (1988).
119. P. R. Selvin and R. Ha, *Single-Molecule Techniques: A Laboratory Manual,* 1 edition ed. (Cold Spring Harbor Lab Press, Cold Spring Harbor, N.Y, 2007), p. 507.
120. D. M. Bers and V. M. Stiffel, "Ratio of ryanodine to dihydropyridine receptors in cardiac and skeletal muscle and implications for E-C coupling," The American Journal of Physiology **264**, C1587-1593 (1993).
121. P. Asghari, "Dynamic distribution of ryanodine receptors in cardiac muscles," (University of British Columbia, 2014).
122. D. R. L. Scriven, A. Klimek, P. Asghari, K. Bellve, and E. D. W. Moore, "Caveolin-3 is adjacent to a group of extradyadic ryanodine receptors," Biophys. J. **89**, 1893-1901 (2005).
123. S. E. Turvey and D. H. Broide, "Innate immunity," J. Allergy Clin. Immunol. **125**, S24-32 (2010).

124. G. Benichou, M. Tonsho, G. Tocco, O. Nadazdin, and J. C. Madsen, "Innate immunity and resistance to tolerogenesis in allotransplantation," Front. Immunol. **3**, 73 (2012).
125. M. G. Netea, J. Quintin, and J. W. van der Meer, "Trained immunity: a memory for innate host defense," Cell host & microbe **9**, 355-361 (2011).
126. C. A. Janeway, Jr. and R. Medzhitov, "Innate immune recognition," Annu. Rev. Immunol. **20**, 197-216 (2002).
127. R. Ubelhart, E. Hug, M. P. Bach, T. Wossning, M. Duhren-von Minden, A. H. C. Horn, D. Tsiantoulas, K. Kometani, T. Kurosaki, C. J. Binder, H. Sticht, L. Nitschke, M. Reth, and H. Jumaa, "Responsiveness of B cells is regulated by the hinge region of IgD," Nat. Immunol. **16**, 534-U257 (2015).
128. P. C. Maity, A. Blount, H. Jumaa, O. Ronneberger, B. F. Lillemeier, and M. Reth, "B cell antigen receptors of the IgM and IgD classes are clustered in different protein islands that are altered during B cell activation," Sci Signal **8**(2015).
129. J. M. Dal Porto, S. B. Gauld, K. T. Merrell, D. Mills, A. E. Pugh-Bernard, and J. Cambier, "B cell antigen receptor signaling 101," Mol. Immunol. **41**, 599-613 (2004).
130. T. Kurosaki, H. Shinohara, and Y. Baba, "B Cell Signaling and Fate Decision," Annual Review of Immunology, Vol 28 **28**, 21-55 (2010).
131. I. Puga, M. Cols, C. M. Barra, B. He, L. Cassis, M. Gentile, L. Comerma, A. Chorny, M. Shan, W. Xu, G. Magri, D. M. Knowles, W. Tam, A. Chiu, J. B. Bussel, S. Serrano, J. A. Lorente, B. Bellosillo, J. Lloreta, N. Juanpere, F. Alameda, T. Baro, C. D. de Heredia, N. Toran, A. Catala, M. Torrebadell, C. Fortuny, V. Cusi, C. Carreras, G. A. Diaz, J. M. Blander, C. M. Farber, G. Silvestri, C. Cunningham-Rundles, M. Calvillo, C. Dufour, L. D. Notarangelo, V. Lougaris, A. Plebani, J. L. Casanova, S. C. Ganal, A. Diefenbach, J. I. Arostegui, M. Juan, J. Yague, N. Mahlaoui, J. Donadieu, K. Chen, and A. Cerutti, "B cell-helper neutrophils stimulate the diversification and production of immunoglobulin in the marginal zone of the spleen," Nat. Immunol. **13**, 170-180 (2012).
132. M. Szydlowski, E. Jablonska, and P. Juszczynski, "FOXO1 transcription factor: a critical effector of the PI3K-AKT axis in B-cell development," Int. Rev. Immunol. **33**, 146-157 (2014).
133. B. Grotsch, S. Brachs, C. Lang, J. Luther, A. Derer, U. Schlotzer-Schrehardt, A. Bozec, S. Fillatreau, I. Berberich, E. Hobeika, M. Reth, E. F. Wagner, G. Schett, D. Mielenz, and J. P. David, "The AP-1 transcription factor Fra1 inhibits follicular B cell differentiation into plasma cells," J. Exp. Med. **211**, 2199-2212 (2014).
134. J. G. Monroe, "ITAM-mediated tonic signalling through pre-BCR and BCR complexes," Nat. Rev. Immunol. **6**, 283-294 (2006).
135. R. E. Davis, V. N. Ngo, G. Lenz, P. Tolar, R. M. Young, P. B. Romesser, H. Kohlhammer, L. Lamy, H. Zhao, Y. Yang, W. Xu, A. L. Shaffer, G. Wright, W. Xiao, J. Powell, J. K. Jiang, C. J. Thomas, A. Rosenwald, G. Ott, H. K. Muller-Hermelink, R. D. Gascoyne, J. M. Connors, N. A. Johnson, L. M. Rimsza, E. Campo, E. S. Jaffe, W. H. Wilson, J. Delabie, E. B. Smeland, R. I. Fisher, R. M. Braziel, R. R. Tubbs, J. R. Cook, D. D. Weisenburger, W. C. Chan, S. K. Pierce, and L. M. Staudt, "Chronic active B-cell-receptor signalling in diffuse large B-cell lymphoma," Nature **463**, 88-92 (2010).
136. R. C. Rickert, "New insights into pre-BCR and BCR signalling with relevance to B cell malignancies," Nat. Rev. Immunol. **13**, 578-591 (2013).
137. A. M. Avalos, F. Meyer-Wentrup, and H. L. Ploegh, "B-cell receptor signaling in lymphoid malignancies and autoimmunity," Adv. Immunol. **123**, 1-49 (2014).

138. B. Treanor, "B-cell receptor: from resting state to activate," Immunology **136**, 21-27 (2012).
139. P. Tolar and S. K. Pierce, "A conformation-induced oligomerization model for B cell receptor microclustering and signaling," Curr. Top. Microbiol. Immunol. **340**, 155-169 (2010).
140. W. W. Schamel and M. Reth, "Monomeric and oligomeric complexes of the B cell antigen receptor," Immunity **13**, 5-14 (2000).
141. J. Yang and M. Reth, "Oligomeric organization of the B-cell antigen receptor on resting cells," Nature **467**, 465-469 (2010).
142. A. Kusumi, C. Nakada, K. Ritchie, K. Murase, K. Suzuki, H. Murakoshi, R. S. Kasai, J. Kondo, and T. Fujiwara, "Paradigm shift of the plasma membrane concept from the two-dimensional continuum fluid to the partitioned fluid: high-speed single-molecule tracking of membrane molecules," Annu. Rev. Biophys. Biomol. Struct. **34**, 351-378 (2005).
143. B. Treanor, D. Depoil, A. Gonzalez-Granja, P. Barral, M. Weber, O. Dushek, A. Bruckbauer, and F. D. Batista, "The membrane skeleton controls diffusion dynamics and signaling through the B cell receptor," Immunity **32**, 187-199 (2010).
144. P. K. Mattila, C. Feest, D. Depoil, B. Treanor, B. Montaner, K. L. Otipoby, R. Carter, L. B. Justement, A. Bruckbauer, and F. D. Batista, "The actin and tetraspanin networks organize receptor nanoclusters to regulate B cell receptor-mediated signaling," Immunity **38**, 461-474 (2013).
145. *Encyclopedia of Immunobiology,* 1 edition ed. (Academic Press, Place of publication not identified, 2016), p. 3126.
146. R. E. Mebius and G. Kraal, "Structure and function of the spleen," Nat. Rev. Immunol. **5**, 606-616 (2005).
147. F. Martin and J. F. Kearney, "Marginal-zone B cells," Nat. Rev. Immunol. **2**, 323-335 (2002).
148. R. Geisberger, M. Lamers, and G. Achatz, "The riddle of the dual expression of IgM and IgD," Immunology **118**, 429-437 (2006).
149. M. Amano, N. Baumgarth, M. D. Dick, L. Brossay, M. Kronenberg, L. A. Herzenberg, and S. Strober, "CD1 expression defines subsets of follicular and marginal zone B cells in the spleen: beta 2-microglobulin-dependent and independent forms," J. Immunol. **161**, 1710-1717 (1998).
150. S. Pillai and A. Cariappa, "The follicular versus marginal zone B lymphocyte cell fate decision," Nat. Rev. Immunol. **9**, 767-777 (2009).
151. S. Pillai, A. Cariappa, and S. T. Moran, "Marginal zone B cells," Annu. Rev. Immunol. **23**, 161-196 (2005).
152. F. Martin and J. F. Kearney, "B-cell subsets and the mature preimmune repertoire. Marginal zone and B1 B cells as part of a "natural immune memory"," Immunol. Rev. **175**, 70-79 (2000).
153. E. J. Pone, J. Zhang, T. Mai, C. A. White, G. Li, J. K. Sakakura, P. J. Patel, A. Al-Qahtani, H. Zan, Z. Xu, and P. Casali, "BCR-signalling synergizes with TLR-signalling for induction of AID and immunoglobulin class-switching through the non-canonical NF-kappaB pathway," Nat Commun **3**, 767 (2012).
154. S. A. Freeman, V. Jaumouille, K. Choi, B. E. Hsu, H. S. Wong, L. Abraham, M. L. Graves, D. Coombs, C. D. Roskelley, R. Das, S. Grinstein, and M. R. Gold, "Toll-like

receptor ligands sensitize B-cell receptor signalling by reducing actin-dependent spatial confinement of the receptor," Nat Commun **6**, 6168 (2015).
155. M. Heilemann, S. van de Linde, M. Schuttpelz, R. Kasper, B. Seefeldt, A. Mukherjee, P. Tinnefeld, and M. Sauer, "Subdiffraction-resolution fluorescence imaging with conventional fluorescent probes," Angew. Chem. Int. Ed. Engl. **47**, 6172-6176 (2008).
156. H. T. Kratochvil, D. G. Ha, and M. T. Zanni, "Counting tagged molecules one by one: Quantitative photoactivation and bleaching of photoactivatable fluorophores," The Journal of Chemical Physics **143**, 104201 (2015).
157. G. C. Rollins, J. Y. Shin, C. Bustamante, and S. Pressé, "Stochastic approach to the molecular counting problem in superresolution microscopy," PNAS **112**, E110-E118 (2015).
158. J. Zhang, K. Leiderman, J. R. Pfeiffer, B. S. Wilson, J. M. Oliver, and S. L. Steinberg, "Characterizing the topography of membrane receptors and signaling molecules from spatial patterns obtained using nanometer-scale electron-dense probes and electron microscopy," Micron **37**, 14-34 (2006).
159. D. Baddeley, "Detecting nano-scale protein clustering," Nat. Methods **12**, 1019-1020 (2015).
160. F. Levet, E. Hosy, A. Kechkar, C. Butler, A. Beghin, D. Choquet, and J. B. Sibarita, "SR-Tesseler: a method to segment and quantify localization-based super-resolution microscopy data," Nat. Methods **12**, 1065-1071 (2015).
161. D. Depoil, S. Fleire, B. L. Treanor, M. Weber, N. E. Harwood, K. L. Marchbank, V. L. Tybulewicz, and F. D. Batista, "CD19 is essential for B cell activation by promoting B cell receptor-antigen microcluster formation in response to membrane-bound ligand," Nat. Immunol. **9**, 63-72 (2008).
162. F. Gasparrini, C. Feest, A. Bruckbauer, P. K. Mattila, J. Muller, L. Nitschke, D. Bray, and F. D. Batista, "Nanoscale organization and dynamics of the siglec CD22 cooperate with the cytoskeleton in restraining BCR signalling," EMBO J. **35**, 258-280 (2016).
163. Y. Xu, L. Xu, M. Zhao, C. Xu, Y. Fan, S. K. Pierce, and W. Liu, "No receptor stands alone: IgG B-cell receptor intrinsic and extrinsic mechanisms contribute to antibody memory," Cell Res. **24**, 651-664 (2014).
164. M. F. Garcia-Parajo, A. Cambi, J. A. Torreno-Pina, N. Thompson, and K. Jacobson, "Nanoclustering as a dominant feature of plasma membrane organization," J. Cell Sci. **127**, 4995-5005 (2014).